ABSTRACT

Title of Dissertation/Thesis:	Architecturally Controlled Bimetallic Nanoparticles for Heterogeneous Catalysis
	Shenghu Zhou, Doctor of Philosophy, 2007
Thesis Directed By:	Professor Bryan W. Eichhorn Department of Chemistry and Biochemistry

This work develops synthetic methods for architecturally controlled AuPt and CuPt bimetallic nanomaterials. The AuPt heteroaggregate, AuPt alloy spherical nanoparticles, and AuPt alloy nanowires were prepared by a sequential or co-reduction method. The unique AuPt heteroaggregate nanostructures, synthesized by the sequential reduction method, contain Au cores with Pt tendrils extending from the Au surfaces. The AuPt alloy nanoparticles or nanowires were prepared by the rapid co-reduction method. This rapid co-reduction method prevents the phase separation and traps the metastable AuPt alloy phase. The AuPt heteroaggregate, alloy spherical nanoparticles, alloy nanowires, and the reported Au@Pt core-shell structures, constitute the rare example of a bimetallic system containing all reported architectures in the literature.

Kinetically stabilized Cu@Pt core-shell nanoparticles were prepared by deposition of Pt onto Cu nanoparticles. The Cu@Pt particles exhibit high stability toward alloying upon annealing. In contrast, the Pt@Cu particles readily transform into alloy structures in the same conditions. This abnormal stability of the Cu@Pt particles is attributed to the Kirkendall mass transport effect, where the inherent diffusion direction from the Pt to Cu

is hindered by a limited population of vacancies in the Cu cores.

These architecturally controlled bimetallic nanomaterials were applied in CO tolerant hydrogen oxidation and de-NO_x reactions with hydrogen. In the $H_2/CO/O_2$ fuel, the AuPt alloy nanoparticles are CO tolerant in hydrogen oxidation, and the AuPt heteroaggregate nanoparticles exhibit enhanced preferential CO oxidation in the presence of Fe promoters. In the NO/H_2 reaction, the Cu@Pt nanoparticles maintain the high activity of pure Pt particles and have a higher selectivity for N_2. Under 4/1 H_2/NO conditions, the selectivity for N_2 over the Cu@Pt catalyst is 45%. In contrast, under the same conditions, the pure Pt catalyst exhibits a selectivity of 22%. The Pt@Pd catalyst enhances activity as well as selectivity due to the near surface alloy effect.

Architecturally Controlled Bimetallic Nanoparticles for Heterogeneous Catalysis

By

Shenghu Zhou

Dissertation submitted to the Faculty of the Graduate School of the

University of Maryland, College Park, in partial fulfillment

of the requirements for the degree of

Doctor of Philosophy

2007

Advisory Committee:
Professor Bryan W. Eichhorn, Chair
Professor Jeffery Davis
Associate Professor Gregory Jackson
Professor Lawrence R. Sita
Associate Professor Robert Walker

Dedication

In memory of my mother, Yumei Huang, for always standing by me. To my loving wife, Qing Zhu, my lovely daughter, Qianqian Zhou, and my father, Linkui Zhou. To my parents in the law, Xiangmin Zhu and Huifen Lv, for taking care of my daughter in my graduate study.

Acknowledgements

First of all, I would like to thank my advisor, Professor Bryan Eichhorn, for these years' guidance and also for educating me how to do research and what the science is. I have learned huge amount of knowledge on materials science form him, which is greatly helpful for my future research career.

I would also like to thank Professor Gregory Jackson for his wonderful discussion in catalysis. I have learned a lot from him about the computer controlled reaction system, without which the fast screening of catalysts would not have been possible. I would also like to thank Dr. Seyed-A. Seyed-Reihani for keeping the Mass Spectrometer running.

I am also grateful to Tim Maugel for his help on TEM, Kevin McIlwrath for images of FE-STEM with EELS and EDS, Bindhu Varughese and Peter Zavalij for their help on X-ray facilities.

To those lab mates I've worked with, Dr. Melanie Moses, Dr. Chad Alan Stoltz, Dr. Emren Nalbant-Esenturk, Oktay Demircan, Selim Alayoglu, Linging Wang, and Anthony Dylla, thanks for their help and good times. I would also like to thank to Anthony Dylla for correcting my thesis.

Thanks to my wife, Qing Zhu, my daughter, Qianqian Zhou, my parents, Yumei Huang and Linkui Zhou, my parents in the law, Xiangmin Zhu and Huifen Lv, for always supporting me.

Table of Contents

Dedication……..……..……ii

Acknowledgements……..……iii

Table of Contents…….……iv

List of Schemes……..……..viii

List of Tables……...…….…ix

List of Figures……..…...……x

List of Abbreviations……..….xx

Chapter 1: Introduction…….....1

1.1. Introduction…… ……...……1

1.2. Theory of Formation of Nanomaterials……..…..2

1.3. Metallic NPs……...……...3

1.4. Syntheses of Nanomaterials by Polyol Method……...…….6

1.5. Shaped-controlled Nanomaterials……...…….……...……..8

1.5.1. Core-shell Structures…….....9

1.5.2. Heterodimers……...…...11

1.5.3. Transformation from Core-shell Structures to Heterodimers……...…….12

1.5.4. Hollow Nanostructures……...……...13

1.5.5. Anisotropic Materials-Nanorods and Nanowires……...18

1.6. Near Surface Alloy Theory for Designs of Heterogeneous Catalysts……...…….21

1.7. Overview of the Thesis……...24

Chapter 2: Syntheses and Characterization of Au-Pt Bimetallic Nanostructures and Their Performance in CO Tolerant Hydrogen Activation…….…..25

2.1. Introduction…….25

2.2. Experiment Section…….31

2.2.1. Materials……...…...31

2.2.2. Syntheses of AuPt Bimetallic Nanostructures…….31

2.2.2.1. Synthesis of AuPt Heteroaggregate Nanostructures…….31

2.2.2.2. Synthesis of AuPt Alloy NPs……....32

2.2.2.3. Synthesis of AuPt Alloy NWs……..33

2.2.3. Preparation of Alumina Supported Catalysts…….……..33

2.2.4. Characterization of Samples……34

2.2.4.1. UV-Visible Absorption Spectroscopy……..34

2.2.4.2. Transmission Electron Microscopy……..34

2.2.4.3. Powder X-ray Diffraction (XRD)…….35

2.2.4.4. X-ray Photoelectron Spectroscopy (XPS)……35

2.2.5. CO Tolerant Performances for Hydrogen Catalytic Oxidation…...……35

2.3. Results…….37

2.3.1. Synthesis and Characterization of AuPt Heteroaggregate Nanostructures…..37

2.3.2. Syntheses and Characterization of AuPt Alloy NPs and NWs……...….45

2.3.3. CO Tolerant Hydrogen Catalytic Activation of Bimetallic AuPt Nanostructures……...….59

2.4. Discussion…….……...…72

2.4.1. Shape Control of AuPt Bimetallic Nanostructures……..……72

2.4.2. The Origin of CO Tolerance……...…….76

Chapter 3: Syntheses of Pt Group Based Nanoparticles and Their Applications in De-NO_x Reactions with hydrogen.....79

3.1. Introduction…….79

3.2. Experimental Section……...……...85

3.2.1. Materials……..……85

3.2.2. Syntheses of Monometallic, Bimetallic NPs, and γ-alumina Supported Catalysts.....86

3.2.2.1. Synthesis of PdCu NPs…….86

3.2.2.2. Synthesis of Pd_xCu_y NPs…….……..86

3.2.2.3. Synthesis of Pd NPs……..87

3.2.2.4. Synthesis of PtCu NPs……..87

3.2.2.5. Synthesis of Pt NPs…….…..87

3.2.2.6. Syntheses of Cu@Pt and Pt@Cu NPs……..88

3.2.2.7. Synthesis of Mixture of Pt and Cu NPs……88

3.2.2.8. Syntheses of Pt NPs Stabilized by Oleylamine and Pt_{40} NPs Stabilized by Dendrimer……..89

3.2.2.9. Syntheses of Pd@Pt and Pt@Pd NPs……...……89

3.2.2.10. Preparation of γ-alumina Supported Catalysts……90

3.2.3. Characterization of Samples……90

3.2.3.1. UV-Visible Absorption Spectroscopy……..90

3.2.3.2. Transmission Electron Microscopy (TEM)……..91

3.2.3.3. Powder X-ray Diffraction (XRD)…….91

3.2.2.4. X-ray Photoelectron Spectroscopy (XPS)……91

3.2.3.5. Infrared Spectroscopy (IR)……...92

3.2.4. Evaluation of Catalysts for NO/H_2 and $NO/H_2/O_2$ Reactions…….92

3.3. Results…….……93

3.3.1. PdCu Alloys…….…93

3.3.2. PtCu Alloys……101

3.3.3. Oleylamine Protected Pt NPs and Dendrimer Protected Pt NPs…….…...105

3.3.4. Cu@Pt and Pt@Cu Core-shell Structures…….106

3.3.5. Pd@Pt and Pt@Pd core-shell NPs…….113

3.3.6. NO Reduction in Lean-burn Conditions with Monometallic Pd and Pt NPs……...……119

3.3.7. NO Reduction with H_2 Using Monometallic NPs…….127

3.3.8. NO Reduction with H_2 Using Bimetallic Core-shell NPs……...……..131

3.3.9. Stability Test of Cu@Pt Catalyst under NO/H_2 Conditions……..136

3.4. Dissicusion……...….140

Chapter 4: Conclusion……..……..142

4.1. Designs of Heterogeneous Catalysts……...…..142

4.2. Synthetic Method Development for Material Synthesis……...……145

4.2.1. Synthetic Methods for Metastable NPs by The Butyllithium Reduction Method…….……..…….....145

4.2.2. Synthetic Method for fully Architecturally Controlled AuPt Bimetallic NPs……...146

4.2.3. Synthetic Method for Kinetically Stabilized Core-shell Structures…...……146

Bibliography……..…….……148

List of Schemes

Scheme 1.1. Synthetic route for the synthesis of Ni@Pd NPs……..……..9

Scheme 1.2. Synthetic route for the synthesis of Pt@Fe_2O_3 NPs…….....10

Scheme 1.3. Synthetic route for the synthesis of heterodimer NPs……..…….....11

Scheme 1.4. Synthetic route for the synthesis of FePt-CdS heterodimer NPs…….….13

Scheme 1.5. Synthetic route for the synthesis of hollow Au NPs……..……...……14

Scheme 1.6. Synthetic route for the synthesis of hollow Pt@CoO NPs…….....15

Scheme 1.7. Synthetic route for the synthesis of hollow Pd NPs…….....…16

Scheme 1.8. Synthetic route for the synthesis of 1D nanostructures……...…….....19

Scheme 1.9. Synthetic route for the synthesis of Cu_2S/Au NWs…….....21

Scheme 2.1. Equations of catalytic and electrochemical H_2/CO/O_2 reactions……..…61

Scheme 2.2. Proposed catalytic mechanisms for H_2/CO/O_2 over the AuPt heteroaggregate and alloy catalysts……...78

List of Tables

Table 1.1. Representations of magic number clusters.....…..4

Table 1.2. Representative synthesis of Au NPs by solution-based methods…….....5

Table 1.3. Recent results of nanoparticle synthesis by the polyol method…….7

Table 2.1. Binding energies and atomic concentrations of Au and Pt in AuPt heteroaggregate NPs by XPS…….43

Table 2.2. XPS binding energies and atomic concentrations of Au and Pt in AuPt alloy NPs…….49

Table 2.3. Single particle composition analysis of 13 particles selected in figure 3.12...52

Table 2.4. The CO conversions of the pure Pt, alloy and heteroaggregate catalysts at an H_2O yield of 15%.....64

Table 3.1. The indexed β-ordered CuPd XRD data of the sample (with a reaction time of 2 hours in glycol) annealed at 300^{o}C for 2 hours……...98

Table 3.2. Comparisons of nominal compositions and compositions by Vegard's Law through XRD patterns of different PdCu alloys……..101

Table 3.3. Compositions of Pt@Cu and Cu@Pt by XPS before etching……....112

Table 3.4. Compositions of Pd@Pt and Pt@Pd NPs by EDS in HRTEM……..…119

List of Figures

Figure 1.1. The near surface alloys…….……..22

Figure 1.2. H binding energies of selected NSA examples……..……23

Figure 2.1. Catalytic reactor for hydrogen oxidation……36

Figure 2.2. Low magnification TEM images of a) individual Au NPs, b) individual Pt NPs, c) AuPt heteroaggregare NPs (inset: enlargement of one particle)……...38

Figure 2.3. Histograms showing particle distributions of a) Au, b) Pt, c) tendrils of AuPt heteroaggregates, and d) cores of AuPt heteroaggregates…….39

Figure 2.4. XRD patterns of AuPt heteroaggregate NPs showing a) as prepared sample, and b) sample annealed at 400^{o}C for 3 hours. The vertical green lines indicate the Au diffractions (JCPDS 01-1172), and the blue lines indicate the Pt diffraction peak positions (JCPDS 01-1311)……...40

Figure 2.5. Time resolved TEM images showing particles of a) 0 minutes, b) 66 minutes, c) 132 minutes, and d) 1226 minutes…….41

Figure 2.6. Time resolved UV-Visible spectra showing SPR absorption of individual Au, AuPt-0 minutes, AuPt-66 minutes, AuPt-132 minutes, and AuPt-1226 minutes. The spectrum of individual Pt NPs is included for comparison……42

Figure 2.7. Images of FE-STEM with EDS showing a) AuPt heteroaggregate NPs, b) Pt map of AuPt heteroaggregate NPs, and c) Au map of AuPt heteroaggregate NPs……...44

Figure 2.8. Atomic densities across one heteroaggregate nanoparticle by EELS showing a) linescan across one heteroaggregate nanoparticle, b) atomic densities of Au and Pt across the particle……...45

Figure 2.9. Low magnification TEM images showing a) AuPt alloy NPs, b) individual Au NPs, and c) individual Pt NPs……46

Figure 2.10. Histogram showing particle size distribution of alloy NPs…….47

Figure 2.11. XRD patterns of AuPt systems. The red pattern-AuPt alloy NPs; the black pattern-AuPt NPs from control experiment (without butyllithium, other conditions is same as those of alloy NPs); the blue pattern-alloy NPs after annealing at 700^{o}C in vacuum for 24 hours. The vertical red lines indicate the diffraction from Au (JCPDS 01-1172), and the black lines indicate the diffraction from Pt (JCPDS 01-1311). The inset is the enlargement of XRD patterns……..47

Figure 2.12. Dark field images of two regions in sample grid. 13 particles were randomly selected for EDS analysis……...51

Figure 2.13. Representative EDS spectrum of one particle……..51

Figure 2.14. Time resolved UV-Visible study of colloids at different reaction stages. Sampling at different temperatures for different reaction times during temperature increasing process, other reaction conditions are same as the typical synthesis of alloy NPs…….53

Figure 2.15. HRTEM image showing lattices of AuPt alloy NPs. The reddish arrows indicate the <111> direction, and the green arrows indicate the <100> direction…….54

Figure 2.16. XRD pattern of AuPt NWs. The vertical green lines indicate the diffraction of Au (JCPDS 04-0784), and the red lines indicate the diffraction of Pt (JCPDS 04-0802)……..55

Figure 2.17. Low magnification TEM images showing a) NWs synthesizeded at 190^{o}C for 2 hours, and b) NWs synthesized at 210^{o}C for 7 hours……57

Figure 2.18. Low magnification TEM image of NWs synthesized by less amount of butyllithium……58

Figure 2.19. HRTEM image showing d-spacing of {200} surfaces of two NWs. The arrows indicate <100> direction……58

Figure 2.20. Comparison of temperature programmable reactions of Pt, alloy and AuPt heteroaggregate catalysts for H_2 oxidation in $H_2/CO/O_2/Ar$ fuel streams (50:0.2:0.5:49.3) and fixed flow rate (0.2085m/s) in reactor. CO is normalized to inlet composition. H_2O composition is normalized with respect to H_2O generated if the limiting reactant O_2 were completely converted to H_2O…….63

Figure 2.21. Comparison of three runs of temperature programmable reactions of AuPt alloy catalyst for hydrogen oxidation in $H_2/CO/O_2/Ar$ fuel streams (50:0.2:0.5:49.3) and fixed flow rate (0.2085m/s) in reactor. CO is normalized to inlet composition. H_2O composition is normalized with respect to H_2O generated if the limiting reactant O_2 were completely converted to H_2O…….65

Figure 2.22. Comparison of temperature programmable reactions of AuPt heteroaggregate catalyst for H_2 oxidation in $H_2/CO/O_2/Ar$ fuel streams (50:0.2:0.5:49.3) with steel or aluminum-CO cylinders and fixed flow rate (0.2085m/s) in reactor. CO is normalized to inlet composition. H_2O composition is normalized with respect to H_2O generated if the limiting reactant O_2 were completely converted to H_2O……..66

Figure 2.23. Comparison of temperature programmable reactions of AuPt alloy catalyst for H_2 oxidation in $H_2/CO/O_2/Ar$ fuel streams (50:0.2:0.5:49.3) with steel or aluminum-CO cylinders and fixed flow rate (0.2085m/s) in reactor. CO is normalized to inlet

composition. H_2O composition is normalized with respect to H_2O generated if the limiting reactant O_2 were completely converted to H_2O……...67

Figure 2.24. Comparison of temperature programmable reactions of AuPt heteroaggregate catalysts with or without Fe promoter for hydrogen oxidation in $H_2/CO/O_2/Ar$ fuel streams (50:0.2:0.5:49.3) and fixed flow rate (0.2085m/s) in reactor. CO is normalized to inlet composition. H_2O composition is normalized with respect to H_2O generated if the limiting reactant O_2 were completely converted to H_2O…….68

Figure 2.25. Temperature programmable reaction using the steel-CO cylinder with O_2 deficient condition showing AuPt heteroaggregate catalyst for H_2 oxidation in $H_2/CO/O_2/Ar$ fuel streams (50:0.45:0.2:49.35) and fixed flow rate (0.2085m/s) in reactor. Yields of CO_2 and H_2O are based on O_2-the limiting reagent. The selectivity for CO_2 is calculated by dividing the yield of CO_2 by the conversion of O_2……..70

Figure 2.26. Temperature programmable reaction using the steel-CO cylinder showing the AuPt heteroaggregate catalysts for H_2 oxidation in $H_2/CO/O_2/Ar$ fuel streams (50:0.1:0.5:49.4) and fixed flow rate (0.2085m/s) in reactor. CO and O_2 are normalized to inlet composition. H_2O composition is normalized with respect to H_2O generated if the limiting reactant O_2 is completely converted to H_2O…….71

Figure 2.27. Comparison of temperature programmable oxidation reactions of the AuPt alloy nanoparticle catalysts using the steel-CO cylinder for hydrogen oxidation with different CO concentrations in $H_2/CO/O_2/Ar$ fuel streams (50:0.1-0.2:0.5:49.4-49.3) and fixed flow rate (0.2085m/s) in reactor. CO and O_2 are normalized to inlet composition. H_2O composition is normalized with respect to H_2O generated if the limiting reactant O_2 were completely converted to H_2O……72

Figure 3.1. XRD patterns of PdCu NPs showing a) as prepared PdCu particles, b) PdCu particles annealed at 550^{o}C for 2 hours. The vertical lines show the peak positions of Pd (black, JCPDS 01-1310), PdCu alloy (red, JCPDS 48-1551), and Cu (green, JCPDS 04-0836)……..95

Figure 3.2. XRD patterns of PdCu particles prepared by glycol with different reaction time showing a) 2 hour, b) 3 hours. The vertical lines show the peak positions of PdCu alloy (JCPDS 48-1551), and stars indicate three new peaks…….96

Figure 3.3. XRD patterns of the annealed PdCu particles synthesized in glycol with a reaction time of 2 hours showing a) as-prepared sample with a reaction time of 3 hours, b) the sample annealed at 300^{o}C for 2 hours (nearly pure β-ordered phase), c) the sample annealed at 480^{o}C for 2 hours (the mixture of α and β phases), and d) the sample annealed at 550^{o}C for 2 hours (pure α phase). The vertical green lines show the peak positions of α alloy of PdCu (JCPDS 48-1551), and the vertical black lines indicate the peaks position of β alloy of PdCu……..97

Figure 3.4. Low magnification TEM images showing a) PdCu alloy NPs prepared by 2-ethoxyethanol, and b) pure Pd NPs……99

Figure 3.5. Histograms of particle distributions of PdCu and Pd NPs showing a) PdCu alloy NPs, and b) Pd NPs…….100

Figure 3.6. XRD patterns of Cu-Pd alloys with different compositions showing a) $PdCu_2$, b) PdCu, and c) Pd_3Cu. The vertical lines show the peak positions of Pd (red, JCPDS 01-1310), PdCu alloy (blue, JCPDS 48-1551), and Cu (green, JCPDS 04-0836)……101

Figure 3.7. XRD patterns of PtCu alloy NPs showing a) as prepared PtCu NPs, and b) the samples annealed at 300^{o}C for 2 hours. Vertical lines indicate the peak positions of Pt

(black, JCPDS 04-0802), PtCu alloy (red, JCPDS 48-1549), and Cu (blue, JCPDS 04-0836)……103

Figure 3.8. XRD patterns of samples prepared by using different Cu precursors showing a) sample with $CuSO_4.5H_2O$, b) sample with $Cu(acac)_2$, and c) sample with $Cu(OAc)_2$. Vertical lines indicate the peak positions of Pt (black, JCPDS 04-0802), PtCu alloy (red, JCPDS 48-1549), and Cu (blue, JCPDS 04-0836)……..104

Figure 3.9. TEM images of Pt-Cu alloy and Pt NPs showing a) PtCu alloy NPs, and b) Pt NPs……...……105

Figure 3.10. Histograms of particle distributions of PtCu and Pt NPs showing a) PtCu alloy NPs, and b) Pt NPs……..105

Figure 3.11. Low magnification TEM image of 4.5 nm Pt and its particle size distribution……...106

Figure 3.12. Low magnification TEM images showing a) Cu@Pt, and b) Pt@Cu core-shell particles……...107

Figure 3.13. Histograms of particle distributions showing a) Cu@Pt, and b) Pt@Cu...108

Figure 3.14. Images of FE-STEM with EDS showing a) the FE-STEM image of Cu@Pt, b) the FE-STEM image of Pt@Cu, c) the Cu phase map of Cu@Pt, d) the Cu phase map of Pt@Cu, e) the Pt phase map of Cu@Pt, and e) the Pt phase map of Pt@Cu.....109

Figure 3.15. XRD patterns of CuPt showing a) the physical mixture of Cu and Pt NPs annealed at 370^{o}C for 5 hours, b) Cu@Pt annealed at 370^{o}C for 5 hours, c) Pt@Cu annealed at 370^{o}C for 5 hours, d) as-prepared Pt@Cu, and e) as-prepared Cu@Pt. Vertical lines indicate the peak positions of Pt (blue, JCPDS 04-0802), PtCu alloy (red, JCPDS 29-0547, another alloy phase of PtCu), and Cu (green, JCPDS 04-0836)……..110

Figure 3.16. HRTEM images of annealed Cu@Pt and Pt@Cu NPs showing a) Cu@Pt annealed at 370^{o}C for 5 hours, and b) Pt@Cu annealed at 370^{o}C for 5 hours……111

Figure 3.17. The compositions of Pt and Cu in Cu@Pt and Pt@Cu by XPS with sequential etching showing a) Cu@Pt, and b) Pt@Cu.....112

Figure 3.18. Low magnification TEM images of a) Pd and b) Pd@Pt NPs……...114

Figure 3.19. Histograms of Pd and Pd@Pt NPs showing particle distributions of a) Pd NPs, and b)Pd@Pt NPs……115

Figure 3.20. Low magnification TEM images showing a) Pt NPs, and Pt@Pd NPs….115

Figure 3.21. Histograms of Pt and Pt@Pd showing particle distributions of a) Pt, and b) Pt@Pd.....116

Figure 3.22. The spectra of EDS in HRTEM showing a) Pd@Pt, b) Pt@Pd.....118

Figure 3.23. FTIR spectra of CO adsorbed on metal NPs showing a) the physical mixture of Pd and Pt colloid, b) Pt colloid, c) Pd@Pt colloid, d) Pd colloid, and e) Pt@Pd colloid……..119

Figure 3.24. Temperature programmable reaction with $NO/H_2/O_2$ showing the catalytic performance of Pd/γ-alumina catalyst (11.5 nm Pd). The y-axis represents the conversion of NO (C-NO), selectivity of N_2 (S-N_2), yields of N_2 (Y-N_2), yield of NO_2 (Y-NO_2) and yield of N_2O (Y-N_2O). The selectivity of N_2 is calculated by dividing Y-N_2 by C-NO. The reactant mixture contains 0.75% NO, 3% H_2, 5% O_2 and Ar balance…….……121

Figure 3.25. Temperature programmable reaction with $NO/H_2/O_2$ showing the catalytic performance of the Pt/γ-alumina catalyst (15.3 nm Pt). The reactant mixture contains 0.75% NO, 3% H_2, 5% O_2 and Ar balance……..……122

Figure 3.26. Temperature programmable reaction with $NO/H_2/O_2$ showing the catalytic performance of the Pt/γ-alumina catalyst (4.5 nm Pt). The reactant mixture contains 0.75% NO, 3% H_2, 5% O_2 and Ar balance……..123

Figure 3.27. Temperature programmable reaction with $NO/H_2/O_2$ showing the catalytic performance of the Pt/γ-alumina catalyst (1.3 nm Pt). The reactant mixture contains 0.75% NO, 3% H_2, 5% O_2 and Ar balance……..……124

Figure 3.28. Comparison of the catalytic performances of the Pt catalysts with different particle size. The reactant mixture contains 0.75% NO, 3% H_2, 5% O_2 and Ar balance……..125

Figure 3.29. TPR of the 15.3 nm Pt/alumina catalyst with a Pt loading of 0.1%. The reactant mixture contains 0.75% NO, 3% H_2, 5% O_2 and Ar balance…….……126

Figure 3.30. TPR of the Pt/LCM catalyst with a Pt loading of 0.1%. The reactant mixture contains 0.75% NO, 3% H_2, 5% O_2 and Ar balance……...…….126

Figure 3.31. TPR of the Pd/γ-alumina with a Pd loading of 1% (11.5 nm). The reactant mixture contains 0.75% NO, 3% H_2 and Ar balance……..…….128

Figure 3.32. TPR of the Pd/γ-alumina with a Pd loading of 1% (11.5 nm). The reactant mixture contains 0.75% NO, 0.75% H_2 and Ar balance…….…….128

Figure 3.33. TPR of the Pt/γ-alumina with a Pt loading of 1% (15.3 nm). The reactant mixture contains 0.75% NO, 3% H_2 and Ar balance……...129

Figure 3.34. TPR of the Pt/γ-alumina with a Pt loading of 1% (15.3 nm). The reactant mixture contains 0.75% NO, 0.75% H_2 and Ar balance……..…130

Figure 3.35. TPR of the Pt/γ-alumina with a Pt loading of 1% (4.5 nm). The reactant mixture contains 0.75% NO, 3% H_2 and Ar balance……...131

Figure 3.36. TPR of the Pt/γ-alumina with a Pt loading of 1% (4.5 nm). The reactant mixture contains 0.75% NO, 0.75% H_2 and Ar balance……..……131

Figure 3.37. TPR of the CuPt/γ-alumina with a Pt loading of 1% (Cu/Pt 1/1). The reactant mixture contains 0.75% NO, 3% H_2 and Ar balanc……...132

Figure 3.38. TPR of the Cu@Pt/γ-alumina with a Pt loading of 1% (Cu/Pt 1/1). The reactant mixture contains 0.75% NO, 3% H_2 and Ar balance……...……..133

Figure 3.39. TPR of the Cu@Pt/γ-alumina with a Pt loading of 1% (Cu/Pt 1/1). The reactant mixture contains 0.75% NO, 0.75% H_2 and Ar balance……134

Figure 3.40. TPR of the Pd@Pt/γ-alumina with a Pt loading of 1% (Pd/Pt 1/1). The reactant mixture contains 0.75% NO, 3% H_2 and Ar balance…….135

Figure 3.41. TPR of the Pt@Pd/γ-aluminaad with a Pt lo ing of 1% (Pd/Pt 1/1). The reactant mixture contains 0.75% NO, 3% H_2 and Ar balance…….136

Figure 3.42. Stability tests for PtCu, Pt@Cu, and Cu@Pt nanocatalysts in the reduction of NO with H_2. The profiles for a 4:1 H_2/NO mixture (reaction time up to 5.8 h) are shown on the left. The subsequent reaction profiles for a 1:1 H_2/NO mixture are shown on the right…….……..138

Figure 3.43. XRD patterns of Cu@Pt, Pt@Cu and CuPt catalyst after stability test. a) Gamma-alumina, b) Pt@Cu/gamma-alumina, star indicates the $Cu_{0.8}Pt_{0.2}$ shell, c) Pt@Cu/gamma-alumina after reaction, hexagon indicate PtCu alloy (JCPDS 29-0547), d) PtCu/gamma-alumina, square indicates as prepared PtCu (JCPDS 42-1326), e) PtCu/gamma-alumina after reaction, triangle indicates PtCu alloy(JCPDS 48-1549), f) Cu@Pt/gamma-alumina, circle indicates Cu (JCPDS 04-0836), g) Cu@Pt/gamma-

alumina after reaction, circle indicates Cu (JCPDS 04-0836). NOTE: Pt peaks are obscured by Gamma-alumina……..……139

List of Abbreviations

acac	acetylacetonate
nm	nanometer
mmol	millimole
^{o}C	degree Celsius
eV	electron volt
XRD	X-ray powder diffraction
EDS	energy dispersive X-ray spectroscopy
TEM	transmission electron microscopy
HRTEM	high resolution transmission electron microscopy
FT-IR	fourier transform infrared
JC-PDS	powder diffraction file
EELS	electron energy loss spectroscopy
TPR	temperature programmable reaction
NSAs	near surface alloys
NPs	nanoparticles
NWs	nanowires
PVP	poly(vinylpyrrolidone)
µl	microliter

Chapter 1

Introduction

1.1. Introduction

Nanomaterials have received significant attention in the last several decades due to potential applications in photonics, catalysis and electronics.[1-3] Nanomaterials are often defined as having dimensions less than 100 nanometers and have the properties fundamentally different from their bulk counterparts. The evolution from vacuum tubes to diodes and transistors, and miniature chips resulted in smaller and smaller devices with more powerful computing ability. Now these electric circuits are approaching nanodimensions, and when this realm is entered, nanocomputers only visible through microscope will appear.[1] Among the current research, application of nanomaterials in catalysis has attracted a lot of attention. Chemists believe that nanomaterials have the potential to be more active and selective than the current technology due to the high percentage of surface atoms and quantum size effects related with small size.[4, 5]

Developing heterogeneous catalysts is often referred to as an art, due to the difficulty in understanding catalytic mechanisms. A major obstacle in developing new heterogeneous catalysts is lack of adequate preparation methods. A typical current procedure involves impregnation of precursor solutions with supports, calcination and reduction at elevated temperatures. Although this method can provide high percentage of surface atoms and is convenient for the large scale manufacturing of catalysts, it is difficult to obtain information about phases and morphologies of catalytic components, especially in multiple component systems. In addition, metal-support interactions caused by high temperature calcination and reduction processes make heterogeneous catalysts

even more difficult to understand.[6-10] Due to the development of new synthetic methods for nanomaterials, there are now many demonstrations of well-characterized, shape-controlled and pre-reduced nanoparticles (NPs).[11-14] Applications of these types of NPs in heterogeneous catalysis may provide a route to understanding catalytic mechanisms.

In this thesis, architecturally controlled bimetallic NPs were synthesized and applied in CO tolerant hydrogen oxidation and de-NO_x reactions. The results of this thesis provide important principles for designs of heterogeneous catalysts and build a bridge to connect the nanomaterials and heterogeneous catalysts. To clearly demonstrate the link between heterogeneous catalysts and nanomaterials, a brief background on metallic NPs is given in the following sections. The sections are organized as follows: a brief overview of the synthesis of nanomaterials and metallic NPs, a review of shape-controlled nanomaterials and a near surface alloy theory for designing heterogeneous catalysts.

1.2. Theory of Formation of Nanomaterials

A common method of nanomaterial synthesis is the precipitation of insoluble products from solution. This process involves nucleation, growth, coarsening and termination.[1] Although these phenomena have been studied for more than a half century, they were not thoroughly understood due to the difficulty in separating these processes. To demonstrate these processes, the formation of Pt NPs is given as an example.[15] A soluble oxidized Pt precursor, such as $H_2PtCl_6.H_2O$, is dissolved in solvent, and then a reducing agent, such as sodium borohydride, is added dropwise. This fast reduction reaction resulted in a zero-valent Pt super-saturated solution. Due to low solubility of Pt(0) in the solution, nanoscale Pt seeds nucleate to form a colloidal suspension. The number of seeds produced in the nucleation process will dictate the final particle size. Fewer seeds will

result in larger particles whereas large numbers of seeds will form smaller particles. In the following growth process, the Pt precursor was continuously reduced and deposited onto the seeds in a diffusion-limited process. In the next coarsening process, small Pt particles are digested by larger Pt particles. This process is also referred to as Ostwald ripening. The driving force for the coarsening process is the higher surface tension of small particles. To avoid continuous growth caused by the coarsening process, ligands are used to terminate the particle growth and stabilize the NPs.[1] Maximizing the interaction between ligands and surface atoms are favorable due to the energy release from coordination. In general, strong ligands favor small particles, and weak ligands produce large particles.[16]

1.3. Metallic NPs

Metallic NPs are a common class of nanomaterials. Well-ordered, highly monodispersed small NPs are often referred to as "nanoclusters".[5, 17] Table 1.1 lists some representations of full-shell "magic number" clusters. They have a hexagonal close-packed structure (hcp) and each atom has the maximum number of nearest neighbors. Ligand stabilized $Au_{55}(PPh_3)_{12}Cl_6$ has been prepared and shown to contain a 1.4 nm core.[5] By enveloping the surface with PPh_3 and Cl^{-1} ligands, the size is enlarged to 2.2-2.3 nm. This material is a single electron transistor, even at room temperature. Usually "magic number" clusters are expected to be less catalytically active due to the additional stability of these systems. In heterogeneous catalysis, only surface atoms are exposed to reactants. At a constant metal loading, a higher percentage of surface atoms usually means a higher catalytic activity. Small particles have high percentage of surface atoms. This is clearly seen in Table 1.1.

Table 1.1. Representations of magic number clusters.[5]

Number of shells	1	2	3	4	5
Numbers of atoms in cluster	M_{13}	M_{55}	M_{147}	M_{309}	M_{561}
Percentage of surface atoms	92%	76%	63%	52%	45%

Metallic NPs can be made by physical or chemical methods.[18] Vapor-phase synthesis is the most commonly used physical method to form nanomaterials and is particularly useful for 1D nanostructures.[3] However, the solution-based chemical methods are more suitable for the synthesis of small and uniform NPs than the former. This brief review primarily focuses on solution-based chemical methods. A detailed review about physical methods for NP synthesis can be found elsewhere.[3]

A common solution-based method to form metallic NPs is through chemical reduction of metal salts. The key factor for successful reduction is to match the reduction potentials of reducing agents with those of the metal precursors. Regularly used reducing agents include H_2, polyol (for example glycol is an commonly used polyol), sodium borohydride ($NaBH_4$), and hydrazine hydrate ($N_2H_4.H_2O$). Sodium borohydride is frequently used in aqueous solution or two-phase reactions.[1] It is strong enough to reduce most of the noble metals such as Au,[19] Pt[15] and Co.[20] However, in some cases it forms metal borides.[21 20]

The formation of Au NPs is the most intensely investigated system and has been known since 1857.[22] A common Au precursor is $AuCl_4^-$ because this ion is a strong oxidizing agent and can be reduced by weak reducing agents, such as carboxylates or alcohols.[23] Widely used stabilizers for Au NPs are thiols, which bind tightly to Au and form small particles. Other protecting agents, such as dendrimers, cyclodextrins,

tetraoctylammonium bromide, and amines, are also exploited in the syntheses of Au particles. Table 1.2 lists some recent results of Au NP synthesis.

Table 1.2. Representative syntheses of Au NPs by solution-based methods.

Starting materials	reductant[a]	stabilizer[b]	avg diam (nm)[c]	solvent	ref
$HAuCl_4$	SN	none	1.9 to 5.2 (A)	diglyme	24
$HAuCl_4$	$NaBH_4$	modified PMA	1 to 4 (A)	H_2O	19
$HAuCl_4$	$NaBH_4$	G6-OH	1.4 (A)	H_2O	25
$HAuCl_4$	Sodium citrate	cyclodextrin	2.5 to 6.6	H_2O	26
$HAuCl_4$	$NaBH_4$	TOAB	4	H_2O/toluene	27
$AuCl_3$	TBAB	ammonium hydroxide	1.5 to 7 (A)	toluene	28
$HAuCl_4$	$NaBH_4$	thiolates	1.4 to 4.7	H_2O/CH_3OH	29
$HAuCl_4$	oleylamine	oleylamine	6 to 21	toluene	30

[a] SN=sodium naphthalenide; TBAB=tetrabutylammonium borohydride.

[b] modified PMA=alkyl thioether end-functionalized poly(methacrylic acid); G6-OH=sixth generation hydroxyl-terminated PAMAM dendrimers; TOAB=tetraoctylammonium bromide. [c] A=monidispersed.

Crooks and co-workers synthesized monodispersed monometallic and bimetallic NPs by dendrimer templates.[25, 31, 32] The particle size is precisely tuned by varying the ratio of precursors to dendrimers. The main disadvantages of this synthetic method are that dendrimers are expensive and removing dendrimers for further applications requires high temperatures under oxidizing environments, which may cause phase transformations of bimetallic NPs.

Other metallic NPs such as Co,[33] Ni,[34] Cu,[31, 35] Ag,[23, 25] Pt,[15] and Fe[36, 37] are all successfully synthesized by solution-based methods. For metals with lower reduction potential such as Fe, more powerful reducing agents are required.

1.4. Syntheses of Nanomaterials by Polyol Method

Among solution-based chemical methods, the polyol method is the most widely applied for the syntheses of nanomaterials. Polyols refer to chemical compounds containing multiple hydroxyl groups, such as sugar alcohols, polymers or monomers with hydroxyl functional groups for organic reactions. Ethylene glycol and 1,2-hexadecanediol are intensely used in the nanoparticle synthesis. Ethylene glycol can reduce most noble metal ions to form metallic NPs, such as Au,[38, 39] Pt,[40] Pd,[41, 42] Ru,[43] Co,[44] Ni[45] and Ag.[39, 46] Unlike sodium borohydride, a room temperature reducing agent, the reduction reactions with ethylene glycol are usually carried out at the reflux temperature to fully reduce the metal salts to metallic state. Another regularly used polyol is 1,2-hexadecanediol, which is soluble in nonpolar organic solvents. Here, Table 1.3 lists some recent results of nanoparticle synthesis by the polyol method.

Table 1.3. Recent results of nanoparticle synthesis by the polyol method.

Compd	Starting materials	reductant	stabilizer	morphology	ref
Pt	H_2PtCl_6	EG[a]	PVP[b]	shape-controlled[c]	40
PtBi	H_2PtCl_6+$Bi(NO_3)_3$	EG	none	spherical	47
Pd	Na_2PdCl_4	EG	PVP	shape-controlled[d]	41
Pd	Na_2PdCl_4	EG	PVP	cubooctahedral[e]	42
FePd	$Pd(acac)_2$+$Fe(CO)_5$[f]	1,2-HD[g]	ACA,TBP[h]	spherical	48
Au	$HAuCl_4$	EG	PVP	shape-controlled[i]	38
Ru	$RuCl_3$	1,2-PD[k]	none	spherical	43

[a] EG=ethylene glycol; [b] PVP=poly(vinylpyrrolidone); [c] multipods and nanowires are generated by varying experimental conditions; [d] triangular and hexagonal NPs by kinetically controlled synthesis; [e] cubooctahedral NPs by oxidative etching; [f] $Pd(acac)_2$=$Pd(CH_3COCHCOCH_3)_2$; [g] 1,2-HD=1,2-hexadecanediol; [h] ACA=adamantanecarboxylic acid, TBP=tributylphosphone; [i] truncated tetrahedral, icosahedral nanocrystals, and nanocubes are generated by varying experimental conditions. [k] 1,2-PD=1,2-propane diol.

The essence of the polyol method is the redox reaction between metal salts and polyols. In the redox process, the metal ions are reduced to the metallic state and nucleate to form NPs. At the same time the polyols are oxidized to organic compounds containing carbonyl groups. Although the polyol method has been widely applied to synthesize various metallic NPs, the reaction mechanism has been studied little.[45, 49] The possible redox reactions are given as follows:[45]

$$M^{n+} + ne \rightarrow M \quad (1)$$

$$2HOCH_2CH_2OH \rightarrow CH_3CO\text{-}OCCH_3 + 2H^+ + 2H_2O + 2e \quad (2)$$

The presence of carbonyl compound such as diacetyl ($CH_3CO\text{-}OCCH_3$) has been detected by FT-IR. In some cases, the polyol can be fully oxidized to CO_3^{2-}.[45] The degree of glycol oxidation is mainly influenced by pH value of the reaction solutions. Water and O_2 also play an important role in the redox reactions as well.[40-42] Water can come from the redox reaction, a trace impurity in glycol or direct addition. O_2 usually comes from the environment. These issues, plus counter-anions such as Cl^-, can influence the kinetics of the redox reaction, and further influence the size, morphology and crystallinity of resulting NPs.[42, 50] A detailed example about the influence of H_2O, O_2, and the counter-anion on the formation of hollow Pd nanostructure[50] is given in Section 1.5.4.

1.5. Shape-controlled Nanomaterials

In the last decade, shape-controlled nanomaterials have been intensely studied due to potential applications in photonics and electronics. For example CdSe@CdS (core@shell) has an enhanced quantum yield and a lower oxidation rate compared to CdSe nanocrystals, and is more suitable for use as light emitting devices.[51] Currently, there are many reports of shape-controlled nanomaterials and their applications in catalysis, magnetic materials and optical devices.[11, 18, 52] Here only core-shell NPs, heterodimers, hollow nanostructures and nanowires are briefly reviewed. A more detailed review of this field can be found in the literatures.[2, 53]

1.5.1. Core-shell Structures

Core-shell structures are typically prepared by sequential deposition methods. [54] These structures can be obtained by a one-pot synthesis or by adding shell precursors after formation of core NPs. Son and coworkers exploited the former approach to synthesize Ni@Pd core-shell structures.[11] The synthetic route is demonstrated in Scheme 1.1.

Scheme 1.1. Synthetic route for the synthesis of Ni@Pd NPs.

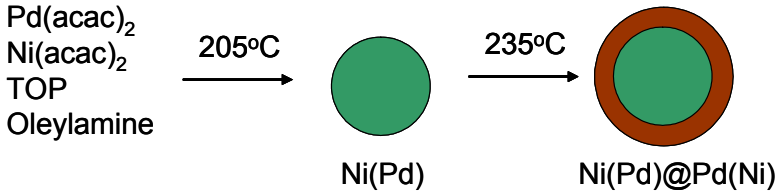

The Ni precursor and Pd precursor were added to the reaction flask at the same time. The core-shell particles were prepared by gradually increasing the reaction temperatures. Due to thermo-decomposition of Ni-trioctylphosphine (Ni-TOP) at relative low temperatures, the Ni core particles were formed first followed by decomposition of Pd precursor at higher temperatures. Due to partial decomposition of the Pd complex at low temperatures, these particles are not phase pure core-shell structures. They consist of Pd rich shells and Ni rich cores. The authors compared the core-shell materials for various Sonogashira coupling reactions with Pd particles having the same amount of palladium. The results showed the core-shell structures have better catalytic activity and are atom–economically applied for Sonogashira coupling reactions.

As mentioned above, a one-pot synthesis may not always produce phase pure core-shell structures. Most core-shell materials are produced by the sequential deposition method, i.e, adding shell precursors after formation of core particles. Pt@Fe_2O_3 are

synthesized by this method.[55] Scheme 1.2 shows the synthetic route for $Pt@Fe_2O_3$ prepared by Teng and co-workers.[55]

Scheme 1.2. Synthetic route for the synthesis of $Pt@Fe_2O_3$ NPs.

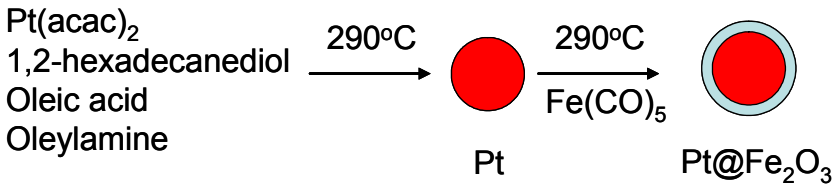

First Pt particles were synthesized by reduction of $Pt(acac)_2$ with 1,2-hexadecanediol in octyl ether with oleylamine and oleic acid as stabilizing agents. Injection of iron pentacarbonyl and raising reaction temperature results in the formation of $Pt@Fe_2O_3$ core-shell structures. The contrast between cores and shells in TEM images is clear. The TEM image shows the less dense Fe_2O_3 shell due to it being a light metal in contrast to the dark dense Pt core. Powder XRD shows strong Pt diffraction and no diffraction from Fe_2O_3 due to the "heavy atom effect" or amorphous properties of Fe_2O_3. The Fe_2O_3 shell was confirmed by the binding energy of Fe in XPS studies.

Reducing these $Pt@Fe_2O_3$ core-shell particles with 5% H_2 at 450°C in Ar produced FePt alloy NPs. TEM studies clearly show that the contrast between Pt and iron oxide disappears after reduction. Powder XRD shows the formation of FePt alloy after reduction and the "as made" alloy has a face-centered tetragonal (fct) structure that is desirable for application in magnetic nanodevices. In most wet chemical syntheses, face-centered cubic (fcc) structures are usually favored and only by annealing these materials at high temperatures will they be converted to thermodynamically favored fct structures.[52]

1.5.2. Heterodimers

Heterodimers are structures with two particles having different compositions that are connected together. These kinds of nanomaterials may have applications in biology, optical devices and heterogeneous catalysis. Gu and co-workers have synthesized Fe_3O_4-Ag, FePt-Ag, and Au-Ag heterodimers by a biphasic method.[13] Scheme 1.3 shows the synthetic route for the biphasic synthesis of heterodimers.

Scheme 1.3. Synthetic route for the synthesis of heterodimer NPs.

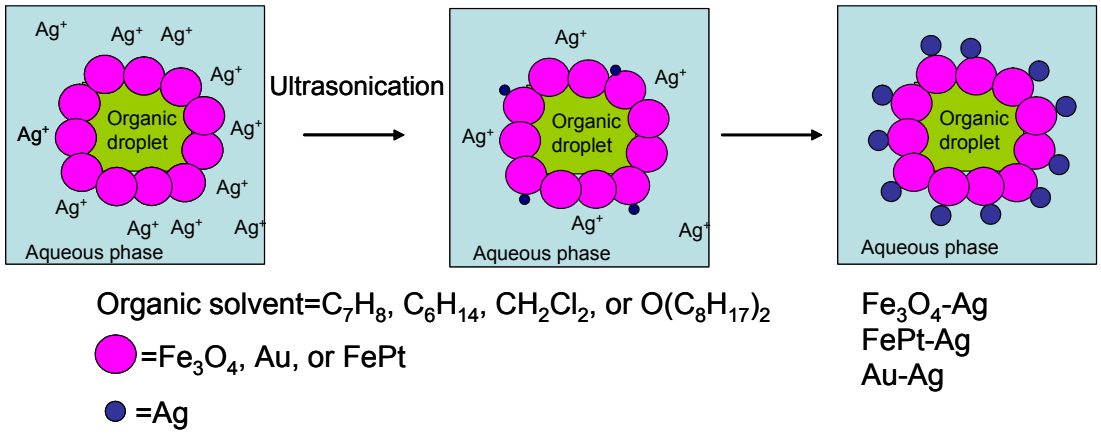

The pre-synthesized Fe_3O_4, FePt or Au particles are dissolved in organic solvents and mixed with an aqueous solution of silver nitrate. After ultrasonification, the heterodimers are formed and can be separated into the organic phase. The authors suggest that the formation of heterodimers occurs at the liquid-liquid interface. Reduction of Ag^+ was catalyzed by the Fe_3O_4 and nucleated on the Fe_3O_4 particles.

The authors did not mention how the reduction of Ag^+ occurred, although it may be caused by ultrasonification.[1] The substantial difference in the surface chemistry of these two particles as heterodimers is suitable for binding different ligands to different parts of dimer, which was proven by fluorescent spectroscopy.

An easier synthetic method for Fe_3O_4-Ag heterodimers was developed by Zhang and co-workers.[56] They exploited a sequential deposition method to make dimers. The pre-synthesized Fe_3O_4 NPs were dissolved with $Ag(CH_3COO)$ and oleylamine in toluene. The resulting solution was heated to 80^oC for 8 hours to give heterodimers. This synthetic method did not use a bi-phasic method and the mechanism is quite straightforward. In this system, oleylamine was used as reducing agent as well as stabilizing agent. The size of these heterodimers can be tuned by varying the experimental conditions.

1.5.3. Transformation from Core-shell Structures to Heterodimers

The above two sections demonstrate preparations of core-shell structures and heterodimers. However, wet chemical methods sometimes produce kinetically stable materials.[57] Annealing at high temperatures will transform these materials into their thermodynamically stable structures. For example, the face-centered tetragonal (fct) FePt alloy forms after reduction of Pt@Fe_2O_3 with 5% H_2 in Ar at 450^oC instead of the expected Pt@Fe particles.[12] According to the Pt-Fe phase diagram,[58] at 450^oC FePt alloy is more thermodynamically stable than Pt@Fe core-shell structures, which is well consistent with the transformation of Pt@Fe_2O_3 to FePt alloy instead of Pt@Fe core-shell structure. Gu and co-workers give a well defined example of transformation of NPs from core-shell structures to heterodimers due to lattice mismatch between the cores and shells.[13]

The synthetic route is illustrated in Scheme 1.4. Magnetic FePt alloy NPs were synthesized by co-deposition of $Fe(CO)_5$ and $Pt(acac)_2$ by 1,2-hexadecanediol in octyl ether with oleylamine and oleic acid stabilizing agents. The resulting FePt particles were then coated with sulfur at 100^oC by addition of a suitable amount of sulfur in solution.

They were then transformed into FePt@CdS core-shell structures by addition of TOPO, 1,2-hexadecanediol, and $Cd(acac)_2$ at 100°C. Raising the temperature of the resulting FePt@CdS colloid to 280°C gave a well-defined FePt-CdS heterodimer structure.

Scheme 1.4. Synthetic route for the synthesis of FePt-CdS heterodimer NPs.

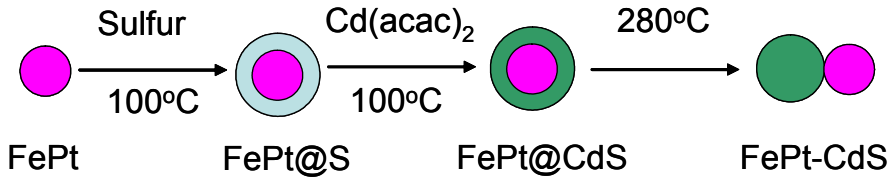

The authors suggested the key factor of transformations is the lattice mismatch between FePt and CdS. The most exciting aspect of this structure is that it contains magnetic FePt particles and semiconductor particles (quantum dots) and may find special applications in biology. Their test of magnetic and florescent properties show that the magnetic properties of FePt and florescent properties of CdSe remain as the individual particles.

1.5.4. Hollow Nanostructures

Hollow nanostructures are currently under intense studies due to applications in catalysis, drug delivery and optics devices.[14] Compared to their solid counterparts, hollow structures can conserve metal.[2] At a constant weight of the materials, the hollow structures have a high percentage of surface atoms. This aspect is especially important in the application of noble metals in catalysis. Another attractive property of hollow nanoparticles is that they have tunable surface plasmon resonance (SPR) bands. For example, the SPR band of gold nanoshells can be tuned from 600 to 1200 nm by changing the diameter and thickness of shells. In contrast, solid gold NPs have a SPR

band centered at 520nm with a maximum of 50 nm variation.[2] The common method for preparing hollow structures is by template methods.[2] The desired metals are deposited onto the templates such as existing Ag nanomaterials, and then the templates are removed by etching or calcination.[2] Au, Pt and Pd hollow structures have been synthesized by Ag templates.[2] Due to many well-defined, shape-controlled Ag NPs, it is possible to prepare hollow structures with similar morphologies. Xia and co-workers have synthesized different types of hollow gold materials including nanorings, nanoshells and nonoboxes by Ag templates.[2] The key reaction using Ag templates to form hollow structures is a galvanic replacement reaction between Ag and the desired metal ions. Any M^{n+} with a higher reduction potential than Ag^{+} can be reduced by Ag template and result in hollow structures. Scheme 1.5 shows the synthetic route of hollow Au nanostructure formation through the use of a Ag template.[59]

Scheme 1.5. Synthetic route for the synthesis of hollow Au NPs.

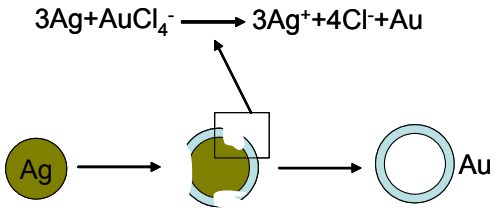

Recently Yin and co-workers exploited the Kirkendall effect to synthesize hollow nanostructures without the use of templates.[14] The Kirkendall effect was discovered in solid-state chemistry a half century ago. When a diffusion couple has a significant difference in their diffusion efficiencies, porosity will form at elevated temperatures. The mass will transport from metals with high diffusion efficiencies to metals with low diffusion efficiencies. The net mass transport will be balanced by vacancy transport in the

opposite direction, resulting in porosity in materials with higher diffusion efficiencies. The Kirkendall effect is usually undesirable in bulk materials due to the formation of porous materials. However, if applied properly, the Kirkendall effect can produce useful materials such as shape memory alloys.[60] It is expected that the driving force for formation of porosity is greater in nanomaterials due to their high surface area to volume ratio. Yin successfully used this concept to synthesize hollow CoO and Co_xS_y structures.[14] The Co NPs were synthesized by thermo-decomposition of $Co_2(CO)_8$ with a stabilizing agent at elevated temperatures. Injection of elemental sulfur or passing O_2 gas through the Co colloid resulted in hollow nanostructures. Time-resolved TEM images clearly demonstrate the evolution of hollow materials. The reaction between cobalt and sulfur is fast, and is complete within a few seconds. The outward flow of cobalt through the cobalt sulfide shell was balanced by the inward flow of vacancies, and resulted in a single hole in the center of the NPs.

HRTEM studies confirm that the hollow CoO structures are not single crystals and show characteristics of multicrystalline materials. The boundaries between crystalline domains may allow small molecules to penetrate into the holes. These types of hollow structures can act as nanoreactors. To demonstrate this idea, the authors have synthesized Pt@CoO yolk-type hollow structures and applied these structures in the hydrogenation of ethylene.[14] Scheme 1.6 shows the synthetic route for Pt@CoO yolk structures.

Scheme 1.6. Synthetic route for the synthesis of hollow Pt@CoO NPs.

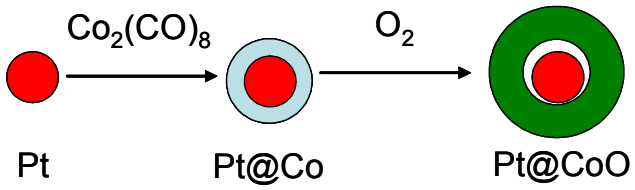

The Pt NPs were synthesized by the polyol method and were then coated with Co by thermo-decomposition of $Co_2(CO)_8$. The resulting Pt@Co core-shell structures were then reacted under O_2 flow to give yolk like Pt@CoO hollow structures. The porosity can be clearly seen by high resolution transmission electron microscope (HRTEM). This hollow yolk Pt@CoO structure showed comparable turnover frequency to pure platinum catalyst when tested for hydrogenation of ethylene at -46 ^oC. At low temperatures Co is inactive, and all the activity comes from the Pt yolks.

Xiong and co-workers recently found that corrosive pitting is helpful to synthesize hollow Pd nanostructures without the use of templates.[50] The corrosive process is usually undesirable. However in the synthesis of hollow Pd nanostructures it provides an elegant method to remove interior material of nanocubes, and results in nanoboxes, nanocages and nanorings at different stage of reaction process. The synthetic route was shown in Scheme 1.7.

Scheme 1.7. Synthetic route for the synthesis of hollow Pd NPs.

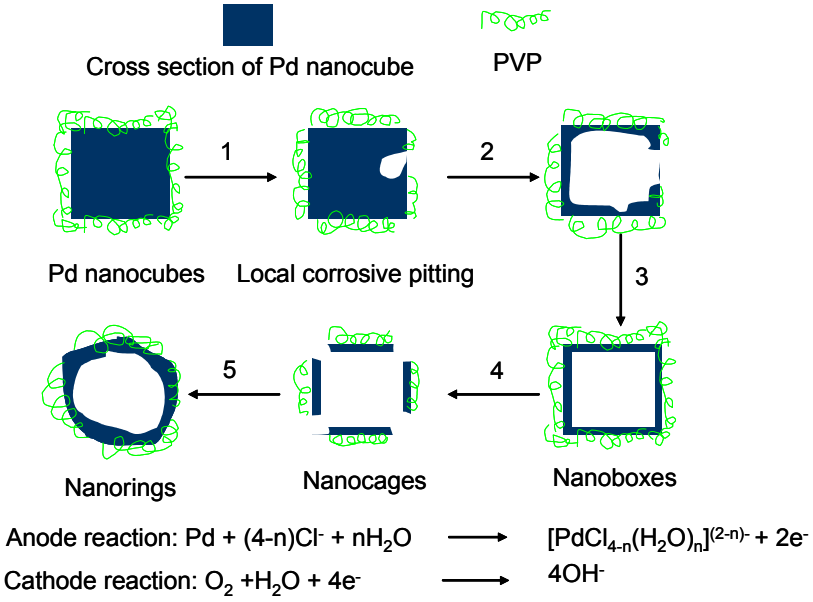

The Pd nanocubes have a diameter of 48 nm, and were synthesized by a polyol method. The common polyol method for Pd synthesis usually forms Pd NPs less than 10 nm. These small particles do not show SPR band in visible region. The authors exploited a mixture of water and minimal ethylene glycol as solvent, Na_2PdCl_4 as the starting material and a high concentration of polyvinylpyrrolidone (PVP) as the stabilizing agent to synthesize large hollow Pd nanostructures. All the above conditions are key factors. The role of water is to decrease the number of seeds in the nucleation process, resulting in a large Pd nanocube with a diameter of 48 nm. Water can also assist in the corrosive pitting of Pd with Cl^- and O_2 from environment. This can be clearly shown in the anode and cathode reactions in scheme 1.7. The concentration of PVP also plays an important role in the system. A high concentration of PVP is needed to prevent corrosive pitting from occurring at all the nanocube surfaces. Finally minimal glycol was used to adjust the relative rate of reduction and corrosive processes. Indeed, before t=20h the reduction process is predominant, and 48nm nanocubes are formed. At t=20h, the corrosive pitting surpasses the reduction process, and holes begin to appear. As the reaction proceeds the empty volume increases with continuous removal of interior Pd by corrosive pitting. The authors monitored the process by measuring the change in concentration of Pd^{2+} ions using Uv-visible spectroscopy. The concentration of Pd^{2+} ions was found to continuously increase during step 2 in scheme 1.6. At a certain point, the concentration of Pd^{2+} ions is high enough, and Pd^{2+} is reduced again by glycol to form enclosed hollow nanoboxes. These hollow Pd structures have a tunable SPR band in visible region, which is fundamentally different than the small Pd particles.

1.5.5. Anisotropic Materials-Nanorods and Nanowires

Nanorods and nanowires are usually refered to as one-dimensional (1D) nanostructures. They are expected to have applications in mesoscopic physics and in the fabrication of nanoscale devices.[3] The essence of 1D nanostructure formation is anisotropic growth, which can be obtained by various chemical and physical methods. Scheme 1.8 illustrates four commonly used strategies for anisotropic growth.[3] 1) Exploit intrinsically anisotropic crystallographic structure to obtain 1D nanostructures. The most famous example is $(SN)_x$, an inorganic polymer. Uniform nanowires of $(SN)_x$ can be easily obtained from vapor phase deposition, and some of the wires will form bundles.[61, 62] Other 1D nanostructures obtained by intrinsically anisotropic structure growth include molybdenum chalcogenides,[63] selenium,[64] tellurium,[65] and Se/Te alloys.[66] 2) Exploit various templates with 1D structures to generate nanowires. This method is intensely used in syntheses of carbon nanotubes. Common templates include step edges on solid substrates,[67] channels in porous materials,[68] self-assembled molecular structures such as micelles and reverse micelles,[69] and existing nanostructures such as carbon nanotubes.[70] 1D structures obtained by physical templates require the removal of templates by calcination or etching. 3) Use capping agents to selectively bind to some facets to favor formation of 1D structures.[46] 4) Self-assembly of NPs into nanowires.[71]

It is worth noting that the creation of a perfect anisotropic nanostructure requires a reversible process between atoms on solid surface and monomers in a fluid phase such as solution, the gas phase or a melt. It allows the atoms to detach from the surface and deposit into the correct positions to obtain uniform, well-controlled 1D nanostructures. Alivisatos and co-workers demonstrated the formation of CdSe nanorods by using high

concentrations of monomers, which provides the driving force for surface reconstruction.[72] The presence of high concentrations of monomers is frequently applied to explain growth of anisotropic materials. In the introduction of chapter 3, a brief introduction of the CdSe system will be presented. This section will primarily focus on the synthetic method using templates.

Scheme 1.8. Synthetic route for the synthesis of 1D nanostructures.

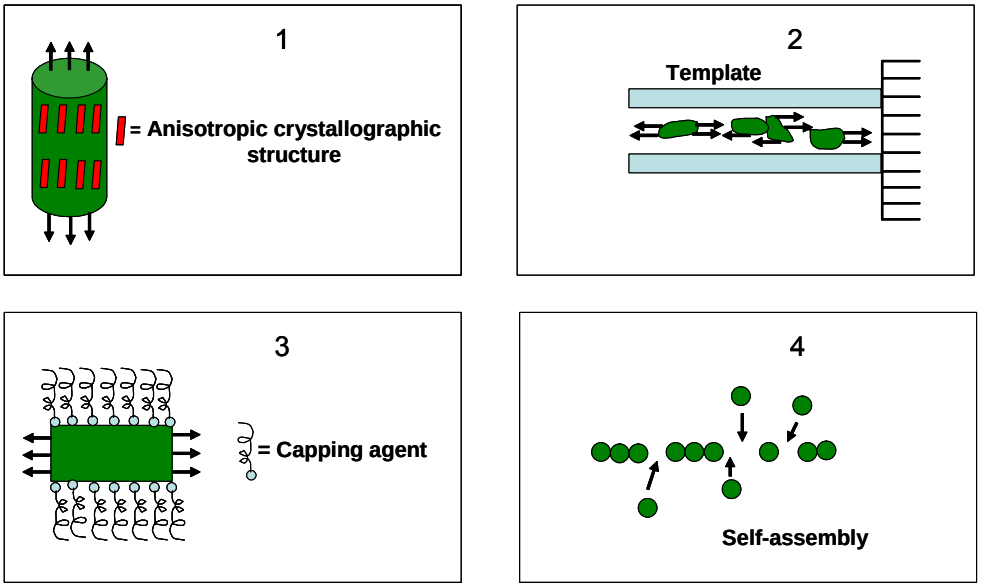

Using nanowires as templates to make new nanowires of different composition is especially useful for nanostructures that may be difficult to synthesize directly. GaP,[73] and MgB_2[74] have been synthesized using carbon nanotube or boron nanowire templates. If the appropriate reagents and reaction conditions are used, the morphology of original 1D nanostructure can be retained in the final product. Wen and Yang exploited Cu_2S nanowires on Cu substrate as templates to prepare Cu_2S/Au core-shell nanowires.[75] Au nanotubes will result after removing the Cu_2S template by etching. The synthetic route is shown in Scheme 1.9.

The pre-synthesized Cu_2S nanowires on Cu substrate were immersed into a $HAuCl_4$ solution. As the reaction proceeds, the color of the solution becomes lighter and finally disappears. The Au^{3+} ion has a high reduction potential and can oxidize the Cu substrate. Because Cu_2S nanowires are good electric conductors, Au^{3+} ions can be reduced at the surfaces of Cu_2S nanowires. After the Cu_2S nanowires were coated by Au shell, the Au shell itself can serve as electric conductor for continuous reactions. The thickness of the Au shell can be adjusted by reaction time and the concentration of Au precursor. After removal of Cu_2S nanowires by acidic solution etching, Au nanotubes are formed.

The existing nanowires can also be sacrificed by appropriate reactants to directly form nanotubes. Ag nanowires are a good template for this purpose due to their low reduction potentials. They can be oxidized by most noble metal ions. Xia and co-workers have synthesized Au, Pd, and Pt nanotubes by using Ag nanowire templates.[2] The redox reactions are believed to first occur at the facets with high surface energies, then to facets with low surface energies, and finally result in seamless nanotubes. If the reaction was continued at an elevated temperature, a highly crystalline structure will form due to coarsening process.

Scheme 1.9. Synthetic route for the synthesis of Cu_2S/Au NWs.

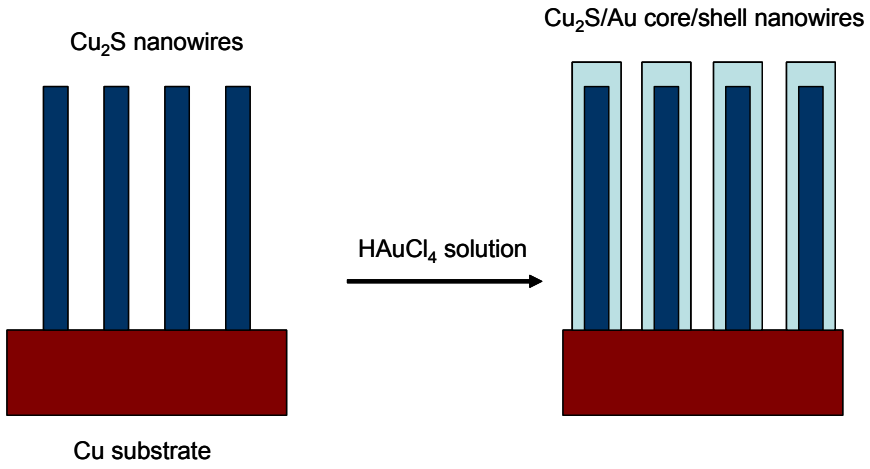

$AuCl_4^- + 3e^- = Au + 4Cl^-$ $E^0 = 1.002V$
$Cu^{2+} + 2e^- = Cu$ $E^0 = 0.3419v$ occuring at Cu substrate
Overall reaction:
$3Cu + HAuCl_4 = 3CuCl_2 + 2Au + 2HCl$

1.6. Near Surface Alloy Theory for Designs of Heterogeneous Catalysts

Heterogeneous catalysis is often referred to as an art due to difficulty in predicting properties. With the development of theoretic calculation and well-controlled nanostructures, design of heterogeneous catalysts becomes possible. However it is still limited to simple systems such as hydrogen activation on idealized catalysts.[76, 77] There is a huge gap between prediction and performance in real industrial catalysts, which sometimes contains more than 10 components.

In chapter 3 bimetallic core-shell NPs are designed for de-NOx reactions. Their unusual catalytic behaviors are attributed to near surface alloy (NSA) effects. The ideal NSAs are those materials with one monolayer of solute on or near the host surface, including overlayers and subsurface alloys. Figure 1.1 illustrates these two types of NSAs. In Figure 1.1, the pairs of solute and host are denoted as solute/host pairs, and * represents the overlayers.[77]

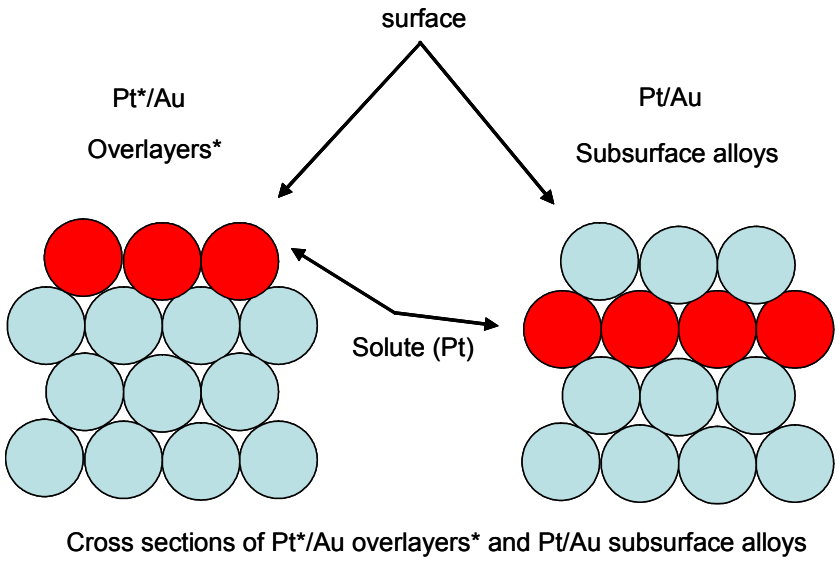

Figure 1.1. The near surface alloys.

Recently, near surface alloys (NSA) have demonstrated their remarkable properties in a limited numbers of cases.[78, 79] Mavrikakis and co-workers exploited theoretical calculations to predict the properties of NSAs for hydrogen activation, and attributed the remarkable properties of NSAs to unique absorption and dissociation of adsorbates on NSAs.[76, 77]

The stability of NSAs in hydrogen is determined by the difference between the segregation energies and binding energies of solute/host pairs. For example, Au*/Pt, an overlayer structure with one monomer of Au on Pt surface, is not stable in hydrogen. Hydrogen will attract Pt atoms to surface due to high binding energy between H and Pt. In other words, the reverse structure Pt*/Au is stable, and hydrogen absorption provides an additional stabilizing effect to maintain this structure. Calculations suggest that some NSAs have decreased H binding energy compared to pure surface metals, which further suggests the surface H is more active due to less binding energy. Figure 1.2 shows some representative data of H binding energy on NSAs from Mavrikakis and workers.[77]

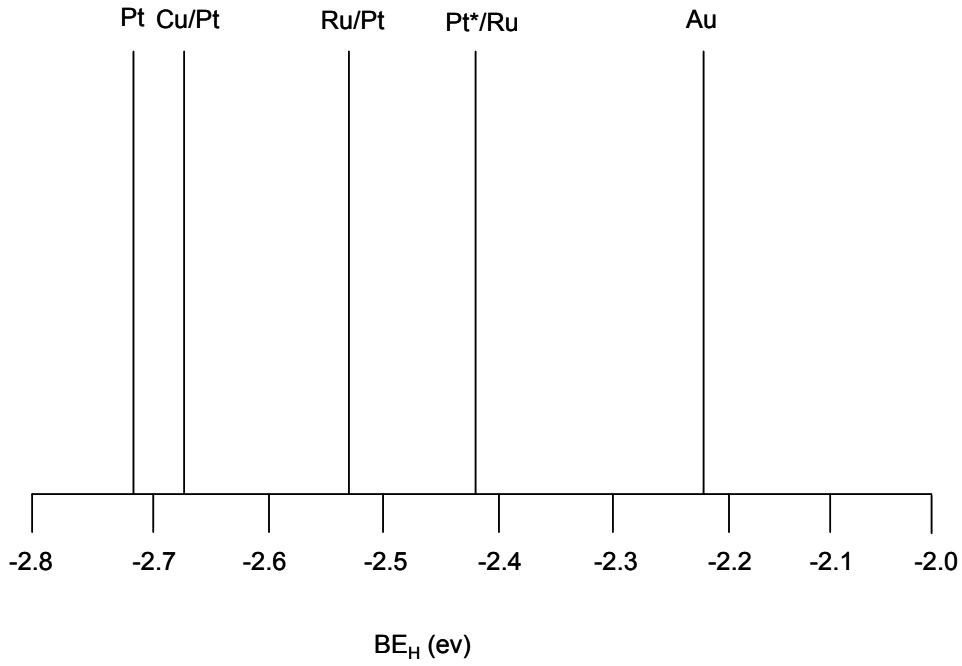

Figure 1.2. H binding energies of selected NSA examples.

Usually weaker H binding means a higher energy barrier of H_2 dissociation, which will give overall lower hydrogen activation. However, for NSAs this assumption is not true. NSAs can facilitate H_2 dissociation by lowering the transition-state energy of dissociation process. The combination of weaker H binding and lower dissociation barrier results in an overall enhancement of hydrogen activation. For example, in Scheme 1.10 the Cu/Pt, Ru/Pt and Pt*/Ru have less negative binding energy compared to pure Pt metal. The H species on the above NSAs are more active than those on pure Pt metal. This phenomenon may explain the remarkable properties of NSAs already reported in the literature.[78, 79] The highly active hydrogen species on NSAs have another advantage for reactions at low temperatures. At such low temperatures, unwanted side reactions may not occur due to high activation barriers, resulting in enhanced selectivity as well as enhanced activity. Although NSAs in Mavrikakis' theory are bulk materials, *i.e.* a surface

monolayer on substrate single crystals or slubs, core-shell NPs may exhibit the same effects due to structure similarity.

1.7. Overview of the Thesis

In the following chapters of this thesis, the syntheses and characterization of new nanomaterials are presented. Their applications in de-NO_x reactions and hydrogen/CO activation are also discussed.

Chapter 2 presents syntheses and characterization of AuPt nanomaterials including a unique Au-Pt heteroaggregate nanostructure, the first fully characterized AuPt alloy NPs and nanowires. Chapter 2 also discusses the applications of heteroaggregate and alloy NPs in CO tolerant hydrogen activation. Chapter 3 presents syntheses and characterization of Pt group based monometallic and bimetallic NPs, including Cu@Pt, Pd@Pt, and Pt@Pd core-shell structures. The syntheses of other monometallic Pd, Pt, bimetallic PdCu and PtCu NPs are also presented. Their applications in de-NO_x reactions by hydrogen with or without oxygen are discussed. Chapter 4 presents the conclusion of this thesis.

Chapter 2

Syntheses and Characterization of Au-Pt Bimetallic Nanostructures and Their Performance in CO Tolerant Hydrogen Activation

2.1. Introduction

Bimetallic catalysts find wide applications in heterogeneous transformation such as CO and NO elimination by PdCu catalysts.[80] A good example is from preparation of vinyl acetate by reaction between ethylene and acetic acid in the presence of oxygen. Individual Au catalysts have no activity, however incorporating Pd into Au gives a much higher activity, which is not seen in any Au or Pd monometallic systems.[81] While some bimetallic catalysts are more efficient than monometallic catalysts, the lack of knowledge regarding structures makes understanding reaction mechanisms difficult especially in multi-component systems.

To fully understand the catalytic reaction mechanisms, a detailed study of composition, phase behavior, geometry and stabilities of catalytic components is essential. To this end, NPs as active components on supports play an important role. There are many demonstrated cases of precise size and shape controls for nanomaterials.[15, 57, 72, 82] Nanorods,[57, 83] nanowires (NWs),[46] dendritic structures,[84] core-shell structures,[11, 55] and heterodimer[13, 85] NPs were produced by exploiting a mixture of stabilizing agents or sequential deposition methods. These systems can be used for catalysis, and effects of particle size and shape can be clearly assigned due to well-characterized structures. Among these systems, bimetallic nanostructures have received significant attention in

recent years due to their novel optical, catalytic, electrical, and magnetic properties.[12, 18, 52]

AuPt bimetallic catalysts have been intensely studied due to their special catalytic performance. An AuPt alloy electrode has been shown to be the most active for the oxidation of various organic compounds in basic solutions.[86] Due to their potential applications, AuPt bimetallic nanostructures have been investigated by several research groups. Lang and coworkers have synthesized dendrimer stabilized AuPt NPs.[87] In this method, Cu NPs were first prepared as sacrificed reductants of Au and Pt ions to form bimetallic materials. According to the reduction potentials, Au precursors usually are much easier to be reduced than Pt precursors. Co-reduction of Au and Pt precursors by common reducing agents, such as polyol or borohydride, will give an Au@Pt core-shell like structure containing an Au rich core/Pt rich shell, or monometallic mixtures. Wu and co-workers have synthesized Au@Pt core-shell NPs in water-in-oil microemulsions.[88] Hydrazinium hydroxide was used as a reducing agent to reduce $HAuCl_4$ hydrate and H_2PtCl_6 hydrate. The color of the reaction solution instantly changed from yellow to red after adding hydrazinium hydroxide to the precursor solution, indicating a Au-core/Pt-shell structure. Au@Pt core-shell structures were also prepared by a seeded growth method. Mandal and co-workers have synthesized Au@Pt by a Keggin ion-mediated synthesis.[89] In this method, Keggin ions (phosphotungstate anions) were used as UV-switchable reducing agents, where phase pure Au core/Pt shell structures resulted from sequential reductions of metal precursors. The same strategy was exploited by Cao and co-workers.[90] Core-Shell structures were obtained by reduction of $PtCl_6^{2-}$ ions in the presence of Au NPs.

Au and Pt are immiscible in a wide range of temperatures and compositions.[91] Bulk studies of alloy formation show that a $Au_{50}Pt_{50}$ alloy does not exist under 1100^{o}C.[91] Theoretical simulations by Mariscal and co-workers also suggested that Pt and Au would like to form a core-shell or a core-shell like structure other than an alloy structure.[92] The terminology of alloy sometimes is not used correctly. Some literature has referred bimetallic NPs as alloy NPs without knowledge of the real structures. According to the definition of the alloy, those atom randomly distributed systems or ordered systems can be referred to as alloys, and core-shell or other phase separated systems are not included. For consistence, the strict definition of alloy is adopted. Because of limited characterization techniques for small AuPt NPs, the literature usually refers them to as AuPt bimetallic NPs. There are several examples showing evidence of alloy formation. Möller and co-worker have synthesized the AuPt alloy for electrochemical studies by a heat treatment in an arc-furnace and subsequent quenching.[86] This solid state method for alloy formation is quite straightforward according to the phase diagram. Njoki and co-workers also exploited a similar method, where AuPt bimetallic NPs were first prepared by a co-reduction of $AuCl_4^-$ and $PtCl_4^-$ with sodium acrylate and H_2. After dispersion of NPs on carbon black support followed by calcinations at 300^{o}C in O_2 and reductions at 400^{o}C in H_2, AuPt alloy formation on support can be seen clearly by XRD.[93] Damle and co-workers have synthesized AuPt alloy NPs by sequential reductions of $AuCl_4^-$ and $PtCl_6^{2-}$ on fatty amine films followed by low temperature annealing at 150^{o}C.[94] The alloy formation was proven by XRD. However, the material shows a sharp XRD pattern, and high 2Θ diffractions are not observed. Furthermore particle size was calculated from

XRD pattern without any TEM images. To our knowledge, no fully-characterized solution-based AuPt alloy nanoparticle synthetic method has been reported.

Controlling the shape and size of nanomaterials remains a challenge in material science. Because of shape and size dependent electronic, optical and catalytic performance, much work has been focused on designing different morphologies. Size control is strongly mediated by surfactants. Stoeva and co-workers found that morphologies and sizes of gold NPs can be reversibly transformed by changing the surfactant. Large polyhedral Au NPs prepared by a reduction of $AuCl_3$ with sodium borohydride in the presence of didodecyldimethylammonium bromide (DDAB) can be transformed into small and spherical NPs by refluxing with alkanethiols (RSH).[16] After precipitation and re-dispersion in toluene with DDAB, these spherical NPs will revert back to large polyhedral NPs. The study by Peng and co-workers shows that size distributions in CdSe are different at different stages of the reaction process.[82] During the growth process, small particles grow faster than larger particles, thus the resulting particle distribution is narrow. In contrast, during the coarsening process small particles will be digested by bigger particles to give a broad distribution. At equilibrium, the spherical shape is the most stable due to the lowest surface free energy. Other NPs having anisotropic shapes usually were prepared by using some method of kinetic control. Peng and co-workers controlled the shape of CdSe nanocrystals by exploiting a mixture of trioctyl phosphine oxide (TOPO) and hexyl-phosphonic acid (HPA) as stabilizing agent. Low concentrations of HPA generate monodisperse spherical NPs, while high concentrations of HPA produce nanorods.[72]The same strategy was employed by Puntes and co-workers to control sizes and shapes of Co nanocrystals using a mixture of TOPO

and oleic acid.[57] It is generally believed that the surfactants were used to control the relative growth rate of different facets. Without TOPO or oleic acid, a broad size distribution and multi-shape nanocrystals were generated. At a constant concentration of oleic acid, the nanorod length varies linearly with respect to the concentration of TOPO.

Side reactions usually are undesirable. However, side reactions can provide an efficient method for shape control if applied properly. The following ZnO system is an example. Chen and co-workers have synthesized ZnO nanocrytstals by zinc stearate with alcohol at an elevated temperature.[95] The resulting nanopyramids were transformed into nanodots in a few minutes by adding stearic acid into the reaction system, and are turned back into nanopyramids due to consumption of stearic acid by the formation of ester with alcohol. More complicated dendritic nanostructures were also found in a manganese oxide system.[84] Dendritic and spherical manganese oxide molecular sieves were synthesized under mild hydrothermal conditions by Yuan and co-workers, and were transformed into dandelion-like microspheres at an elevated temperature.

Among these anisotropic materials, nanowires have received significant attention because of a possible quantum confinement effect.[3] Liang and coworkers exploited Co NPs as templates to make AuPt hollow NWs.[96] Due to strong dipole-dipole interactions, ferromagnetic Co NPs self-assemble into a 1-D structure and are consumed by redox reactions between templates and desired metal precursors to form AuPt hollow NWs. A mixture of surfactants was also used to control the anisotropic growth in the formation of NWs. Yu and co-workers exploited a mixture of oleylamine and a long-chain carboxylic acid to prepare samaria NWs with a single unit cell thickness.[97] Different shapes and sizes of samaria nanostructures can be generated by varying experimental conditions such

as types of stabilizing agents and concentrations of precursors. Recently Sun and Xia have successfully synthesized silver NWs without exotic seeds.[46] The key factor is to control the injection rate of precursor solution. The Ag NPs formed at the initial stage can serve as the seeds for the growth of NWs. Sun and Xia found that the number of repeating unit of PVP and the ratio of PVP to Ag play an important role on morphologies and dimensions. The authors believe that PVP possibly selectively binds to certain surfaces and favors 1-dimentional growth.

In this chapter, we demonstrate syntheses and characterization of novel AuPt heteroaggregate nanostructures, spherical AuPt alloy NPs, and NWs. The AuPt heteroaggregate nanostructures were synthesized by a seeded growth method. This unique nanostructure presumably results from the thermodynamic immiscibility of Au and Pt, and is fundamentally different from individual Au, Pt, mixtures, alloys or core-shell structures. AuPt alloy NPs were prepared by a co-reduction of $HAuCl_4$ and H_2PtCl_6 with butyllithium. This rapid reduction method kinetically traps the metastable AuPt phase. Varying experimental conditions generates AuPt NWs. To test the potentials of these AuPt nanomatericles as a CO tolerant electrode, AuPt heteroaggregate and alloy NPs were evaluated for hydrogen activation with CO contaminated H_2 fuels. The results show that heteroaggregates need reducible oxides for hydrogen activation under CO. In contrast alloy particles show enhanced CO tolerance for hydrogen oxidation without reducible oxides. These studies provide important information about architectural control of nanomaterials and design of CO tolerant anode electro-catalyst for low temperature fuel cells.

2.2. Experimental Section

2.2.1. Materials

Hydrogen tetrachloroaurate(III) hydrate($HAuCl_4.xH_2O$, 99.999%), chloroplatic acid hydrate($H_2PtCl_6.xH_2O$, ≥99.9%), platinum(II) acetylacetonate($Pt(acac)_2$, 97%), oleylamine($C_{18}H_{37}N$, tech., 70%), butyllithium(C_4H_9Li, 2.0M solution in cyclohexane), octyl ether($C_{16}H_{34}O$, 99%) and decahydronaphthalene($C_{10}H_{18}$, anhydrous, 99+%, mixture of *cis* and *trans*) were purchased from Aldrich. Gamma-alumina(S. A. 80-120 m^2/g, 3 micron APS powder) was purchased from Alfa Aesar. All the chemicals were used without any further purification. H_2, Ar, and O_2 cylinders with ultra high purity, CO steel and aluminum cylinders with 99.5% purity were purchased from Airgas, and used without further purification.

2.2.2. Synthesis of AuPt Bimetallic Nanostructure

All the following syntheses of nanomaterials were carried out under N_2 if not mentioned.

2.2.2.1. Synthesis of AuPt Heteroaggregate Structures

0.157mmol $HAuCl_4.xH_2O$ was dissolved in 26.4ml decahydronaphthalene with 4.4ml oleylamine. The solution was stirred and kept at 110^oC for 12hr. The resulting purple colloid was cooled to room temperature and charged with 0.157 mmol $Pt(acac)_2$. The reaction was then slowly heated to dissolve the precursors and then refluxed for 2 hours. The dark colloid was cooled to room temperature, diluted with ethanol, and centrifuged to deposit the NPs. The top clear solution was decanted, and the power in the bottom of centrifuge tubes was redispersed in toluene with a suitable amount of oleylamine if

needed. A part of the toluene colloid was stored in capped vials for preparation of TEM samples and UV-visible measurement. The left colloid was further washed by the above procedure at least four times. The resultant black powdery product was dried in oven at 60^{o}C for 2 hours, and stored in capped vials for powder X-ray diffraction and X-ray photoelectron spectroscopy measurement.

Monometallic Au and Pt NPs were synthesized by the same procedure. 0.157mmol $HAuCl_4.xH_2O$ was dissolved in 26.4ml decahydronaphthalene with 4.4ml oleylamine. The solution was stirred at 110^{o}C for 12hr to give a purple colloid. For the synthesis of Pt NPs, 0.157mmol $Pt(acac)_2$ was dissolved in 26.4ml decahydronaphthalene with 4.4ml oleylamine. The solution was stirred and refluxed for 2hr to give a dark brown colloid. Post-processing procedures are the same as those of hetroaggragates described above.

2.2.2.2. Synthesis of AuPt Alloy NPs

0.179mmol $HAuCl_4.xH_2O$ and 0.179mmol $H_2PtCl_6.xH_2O$ were co-dissolved in 15ml octyl ether with 1.050ml oleylamine at 78^{o}C. The solution was then manually injected, via a syringe, into a 78^{o}C butyllithium solution containing 30ml octyl ether and 1.3ml 2.0M butyllithium cyclohexane solution. A dark brown colloid was formed in several seconds after the solution of Au and Pt precursor was injected. The resulting dark brown colloid was stirred for 30 minutes at 78^{o}C. It was then heated to 230^{o}C for 2 hours. This dark brown colloid was then cooled to room temperature, and diluted by ethanol followed by centrifuging to deposit NPs. The black powder product was re-dispersed in toluene with suitable amount of oleic acid and oleylamine if needed. The colloid was then washed with water by centrifugation. The top organic layer was collected, diluted with ethanol, and centrifuged to deposit NPs. The resulting powder was redispersed in toluene

with a suitable amount of oleylamine and oleic acid if needed. A part of the colloid was stored in capped vials for Uv-visible measurement and preparation of TEM grids. The left colloid was further washed by the above procedure at least four times. The resultant black powdery product was dried in oven at 60^{o}C for 2 hours, and stored in capped vials for powder X-ray diffraction and X-ray photoelectron spectroscopy measurement.

Individual Au and Pt NPs were synthesized by the same method except without the addition of the second metal precursor and half amount of oleylamine and butyllithium. For synthesis of Pt NPs, after stirring at 78^{o}C for 30 minutes, the reaction mixture was heated to 180^{o}C for 2 hours. Post-processing procedures were the same as above.

2.2.2.3. Synthesis of AuPt Alloy NWs

The procures for the synthesis of AuPt alloy NWs is the same as those of AuPt NPs except only 1.1 ml of 2.0M butyllithium cyclohexane solution is used and the reaction is done at 190^{o}C. The degree of branches in NWs increases with decreasing amounts of butyllithium. Post-processing procedures are the same as those of alloy NPs.

2.2.3. Preparation of Alumina Supported Catalysts

Supported catalysts were prepared by impregnating a required amount AuPt bimetallic colloid with a required amount of gamma-alumina followed by removing solvent at approxiately 70^{o}C in vacuum. The powder was further washed with acetone and ethanol. The Pt loading of all the catalysts is 1% (wt %), and the molar ratio of Au to Pt is 1 to 1.

Preparation of the heteroaggregate catalyst with Fe promoter is similar. The required amount of $Fe(NO_3)_3.9H_2O$ was dissolved in a suitable amount of water. The pre-synthesized 1% (wt %) AuPt heteroaggregate catalyst was immersed into the stirring

$Fe(NO_3)_3$ aqueous solution. The solid catalyst powders were obtained by removing the solvent under vacuum. Before activity measurements, the catalyst was reduced by 10% of H_2 in Ar at 200^oC for 3 hours.

2.2.4. Characterization of Samples

2.2.4.1. UV-Visible Absorption Spectroscopy

For UV-Visible absorption spectroscopy, Au, Pt, and AuPt bimetallic toluene colloids were first diluted in toluene, and then measured against a toluene background on a HP 8452A diode array spectrometer with a deuterium lamp having a resolution of 2 nm. The concentrations of nanoparticle colloids were adjusted to have a comparable maximum absorption.

2.2.4.2. Transmission Electron Microscopy

All low magnification images were taken using Zeiss EM 10CA transmission electron microscope with an accelerating voltage of 80 kV. 4 μl of diluted AuPt nanomaterial colloids were deposited onto CFC-300Cu grids (purchased form Electron Microscopy Sciences), and were then dried by evaporation in air. FE-STEM AuPt heteroaggregate nanostructure images were taken by Kevin McIlwrath at Hitachi High Technologies America on HD-2300 200 kV dedicated FE-STEM with an EELS attachment and EDX detector with high sensitivity. HRTEM images of AuPt alloy nanomaterials were taken on JEOL 2100F 400 kV FE-TEM. The single particle analyses (EDS) of AuPt alloy NPs were investigated on the JEOL JEM-2010F Field Emission Transmission Electron Microscope operating at 200 kV. The analysis was carried out in Scanning Transmission mode (STEM) using a nominal 1 nm FWHM probe with a 70 μm condenser aperture

used to reduce uncollimated radiation. In this mode, there is approximately 0.5 nA of beam current hitting the specimen. Thermo Noran Vista analysis software was used with a 40 mm^2 X-ray detector.

2.2.4.3. Powder X-ray Diffraction (XRD)

Powder XRD was operated on Bruker C2 Discover X-ray Powder Diffractometer with a Hi-Star area dedector and CuK_α radiation. Analyses of XRD patterns were performed using the JADE® software package with the JC-PDF database and auto indexing. Diffraction patterns were measured in the 2Θ range from 5 to 90°. XRD samples were prepared by pressuring powder onto a glass plate. Prior to the measurement, the samples were thoroughly washed by ethanol to remove excess organic chemicals.

2.2.4.4. X-ray Photoelectron Spectroscopy (XPS)

XPS measurements were conducted on a Kratos Axis 165 spectrometer by Dr. Bindhu Varughese using Mg K_α radiation in a vacuum of 4×10^{-10} Torr. The hybrid mode was applied for measurements of 10 scans with a step size of 0.1 eV and a sweep time of 60s. The spectra were recorded in the FAT analyzer mode with a pass energy of 80 eV. The data processing was performed using graphical analysis software. The spectra were fit with 60% Gaussian/ 40% Lorentzian peaks after linear background subtraction. The minimum number of peaks were used to deconvolute the spectral envelops.

2.2.5. CO Tolerant Performances for Hydrogen Catalytic Oxidation.

Catalytic hydrogen oxidation activity with CO contaminated H_2 fuel was measured by placing the supported catalyst in a packed bed arrangement in a 6.4 mm inner diameter (ID) quartz tube centered in a vertical programmable tube furnace. The catalyst charge

was 5.5mm in height. The packed bed consisted of 105mg of catalyst (including support, the Pt loading is 1.0%) intermixed with 135 mg of 1-μm quartz particles to provide adequate flow through the bed. The bed was held in place by quartz wool above and beneath, which assisted in preheating the gases to the prescribed furnace temperature. The reactor is shown in Figure 2.1. Computer-controlled electronic mass-flow controllers were used to vary flow rates and to fix reactor residence times and the reactant gas velocity (0.2085 ± 0.0104 m/s). The reactant mixture contained 50% H_2, 0 - 0.45% CO, 0.2 - 0.5% O2, with an Ar balance. Product gases were sampled at the outlet of the catalytic reactor, and measured continuously with a carefully calibrated mass spectrometer (VG Prima δB). Product compositions were determined from the calibrated sensitivities and ion-cracking patterns for the analyzed gases. The catalytic data were obtained after stabilized performance was achieved for all the catalysts.

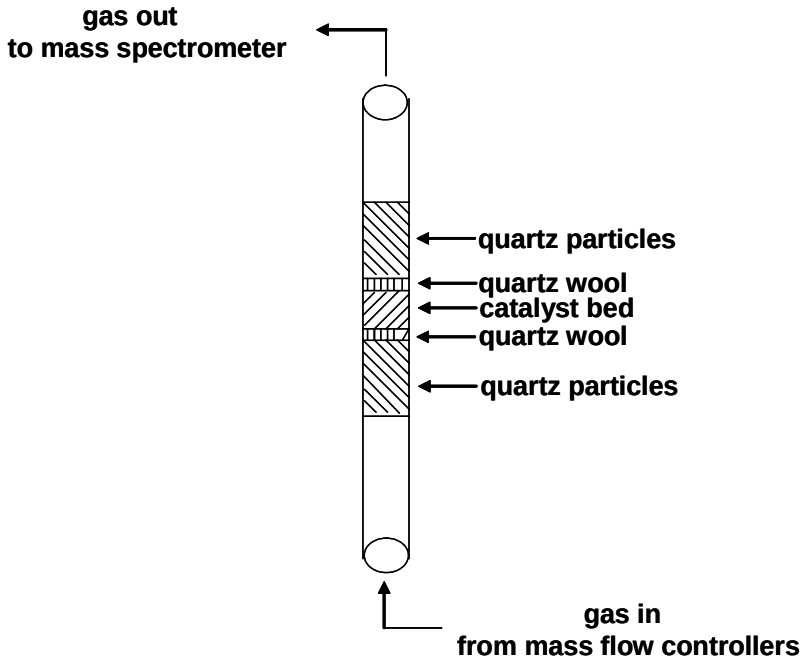

Figure 2.1. Catalytic reactor for hydrogen oxidation.

2.3. Results

2.3.1. Synthesis and Characterization of AuPt Heteroaggregate Nanostructures

Monometallic Pt and Au NPs were prepared by employing minor modifications of published procedures.[30] Due to the higher temperature needed for reduction of $Pt(acac)_2$ by oleylamine, decahydronaphthalene (boiling point, 189^{o}C) was used as a solvent instead of toluene. In this method, oleylamine works as a reducing agent as well as a stabilizing agent. The AuPt heteroaggregate particles were prepared using a modified standard procedure for a sequential core-shell particle growth.[98] After washing and re-dispersing in toluene, the Au colloid shows a purple color, and the Pt colloid has a black color, while the AuPt colloid has a black color with a light red background.

Low magnification TEM images (Figure 2.2) and particle distributions (Figure 2.3) show that monometallic Au NPs have a diameter of 10.9 ± 2.2 nm with a spherical shape and Pt NPs have a 4.7 ± 1.1 nm diameter with branched shapes (the mean particle size and standard deviation of size distribution were obtained by measuring approximate 50 nanoparticles). Unexpectedly, AuPt structures have a heteroaggreagate structure with 11.2 ± 2.5 nm core and 7.5 ± 1.9 nm tendrils extending from the surfaces of cores (Figure 2.2). Particle size analysis shows that the average particle size of the cores of the heteroaggregate NPs is very close to that of the individual Au NPs. Furthermore, the shapes of the tendrils of heteroaggregate NPs are similar to those of Pt NPs. These observations with the sequential reduction method suggest that the heteroaggregate NPs consist of Au cores and Pt tendrils.

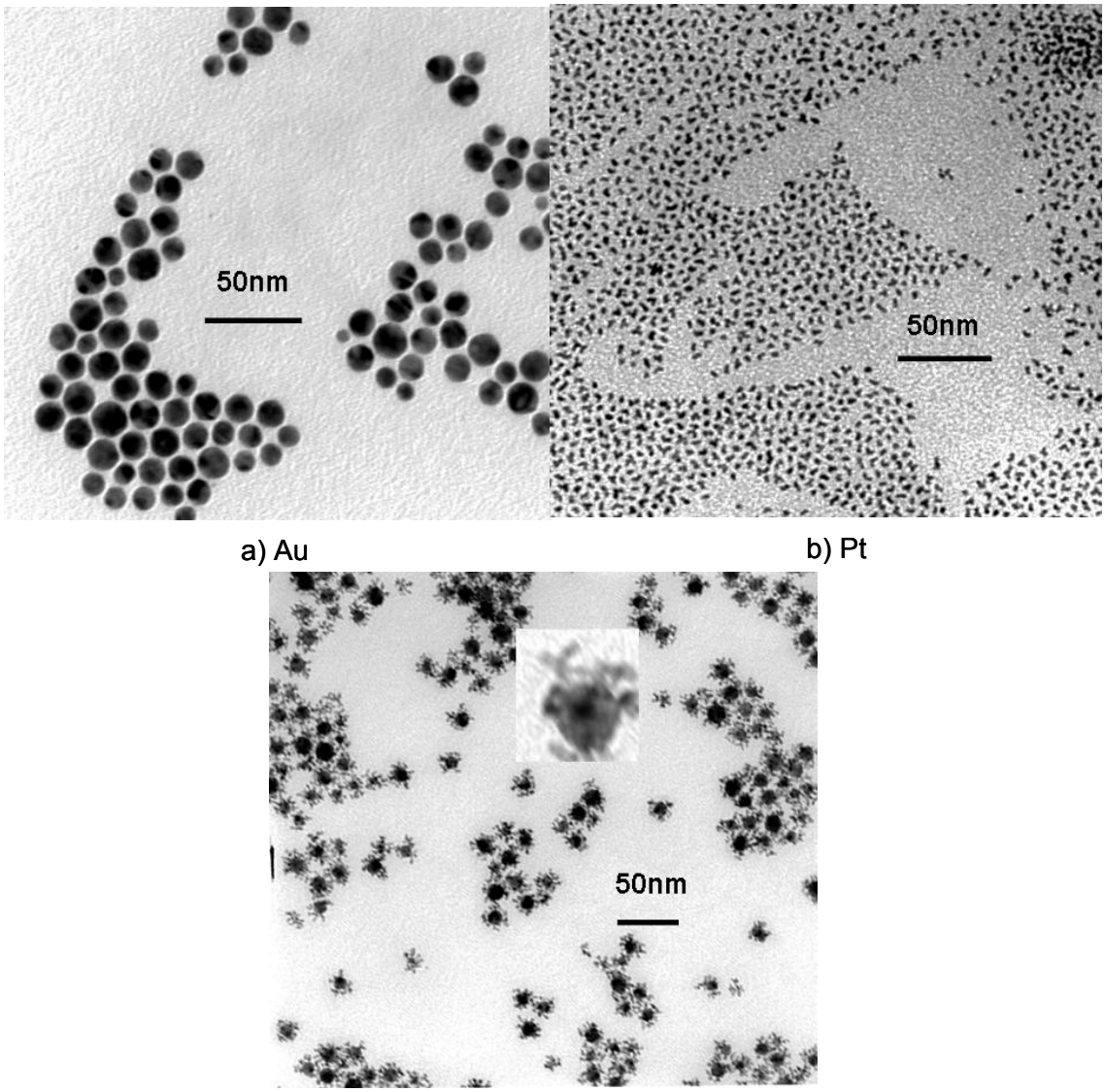

Figure 2.2. Low magnification TEM images of a) individual Au NPs, b) individual Pt NPs, c) AuPt heteroaggregare NPs (inset: enlargement of one particle).

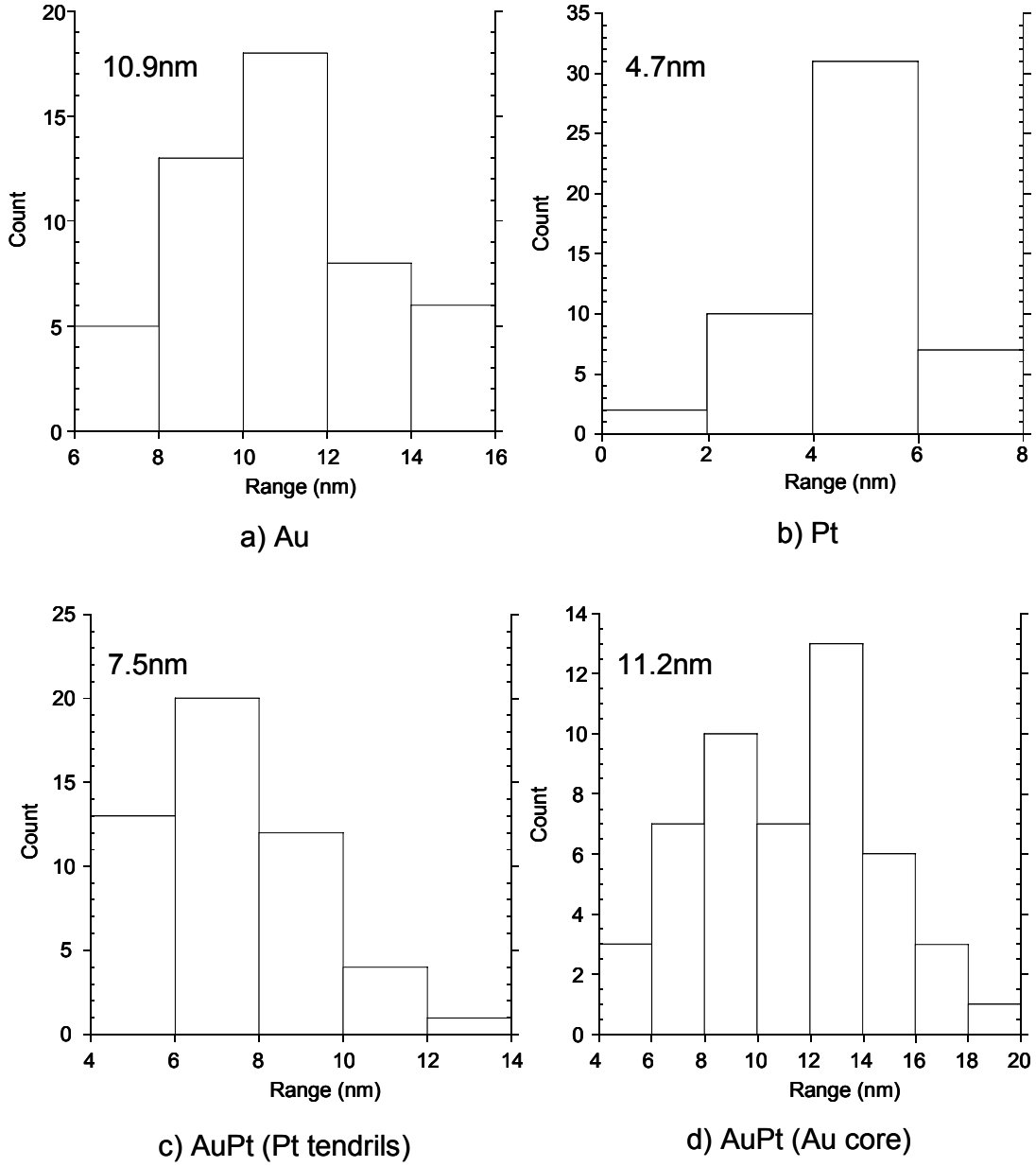

Figure 2.3. Histograms showing particle distributions of a) Au, b) Pt, c) tendrils of AuPt heteroaggregates, and d) cores of AuPt heteroaggregates.

XRD patterns (Figure 2.4) show that AuPt dentritic structures consist of a phase pure Au and a Pt shoulder. Annealing this sample in vacuum at 400^{o}C for 3 hours to crystallize the components gives a well-defined Pt and Au diffraction. This is consistent with the bulk phase diagram of the AuPt system.[91] Below 1100^{o}C, 1/1 Au and Pt are

immisicible such that phase separated nanostructures are thermodynamically favored. Alloy formation by kinetic control will be addressed in the following sections.

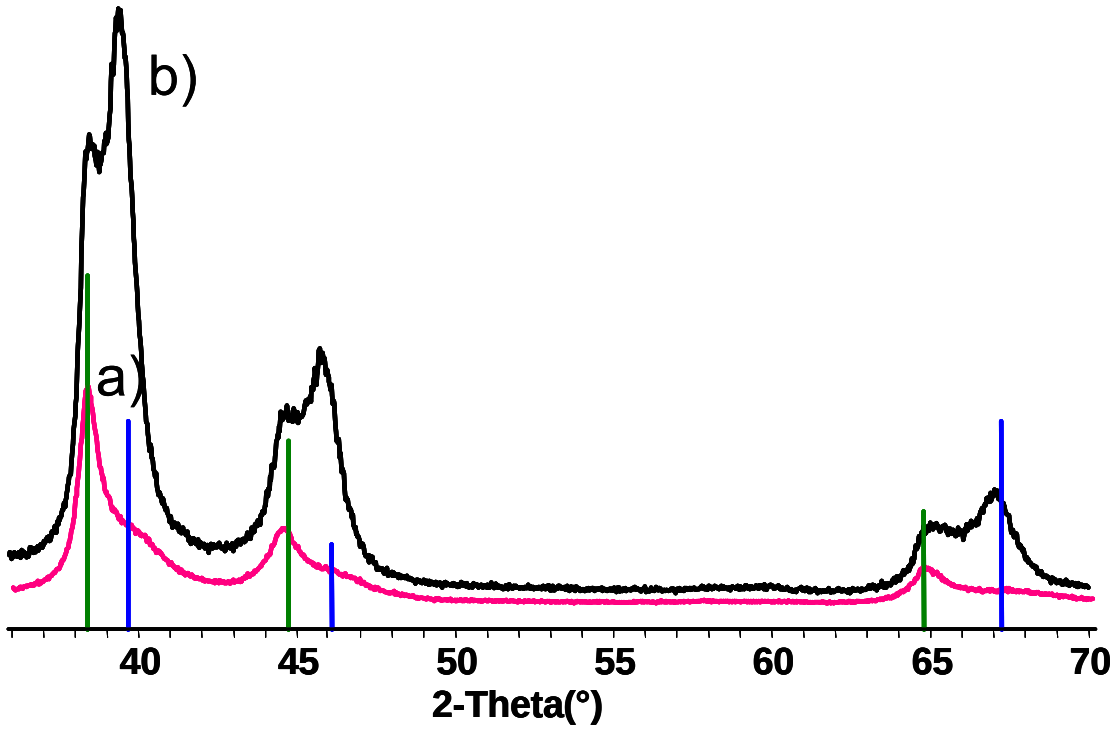

Figure 2.4. XRD patterns of AuPt heteroaggregate NPs showing a) as prepared sample, and b) sample annealed at 400°C for 3 hours. The vertical green lines indicate the Au diffractions (JCPDS 01-1172), and the blue lines indicate the Pt diffraction peak positions (JCPDS 01-1311).

In order to watch the gradual growth of tendrils, the reduction of $Pt(acac)_2$ was carried out at 155°C to elongate the reduction process. Figure 2.5 clearly shows the tendrils growing gradually from the Au NPs. The same trend was found in UV-Visible studies of the colloid at different stages. Figure 2.6 shows that the SPR absorption intensity near 520 nm gradually deceases with more tendrils decorating the cores. In contrast, pure Pt NPs do not show any SPR absorption near 520 nm.

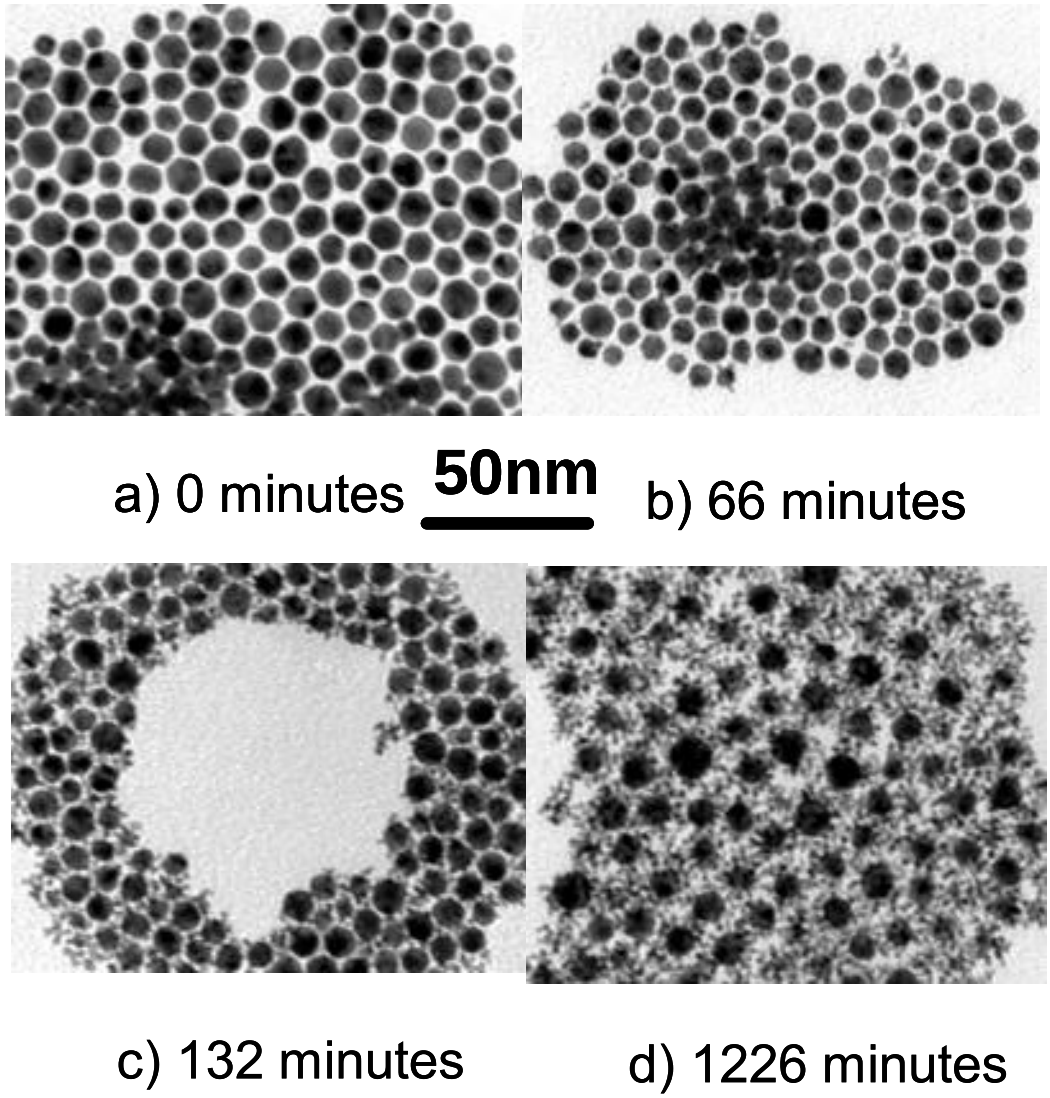

Figure 2.5. Time resolved TEM images showing particles of a) 0 minutes, b) 66 minutes, c) 132 minutes, and d) 1226 minutes.

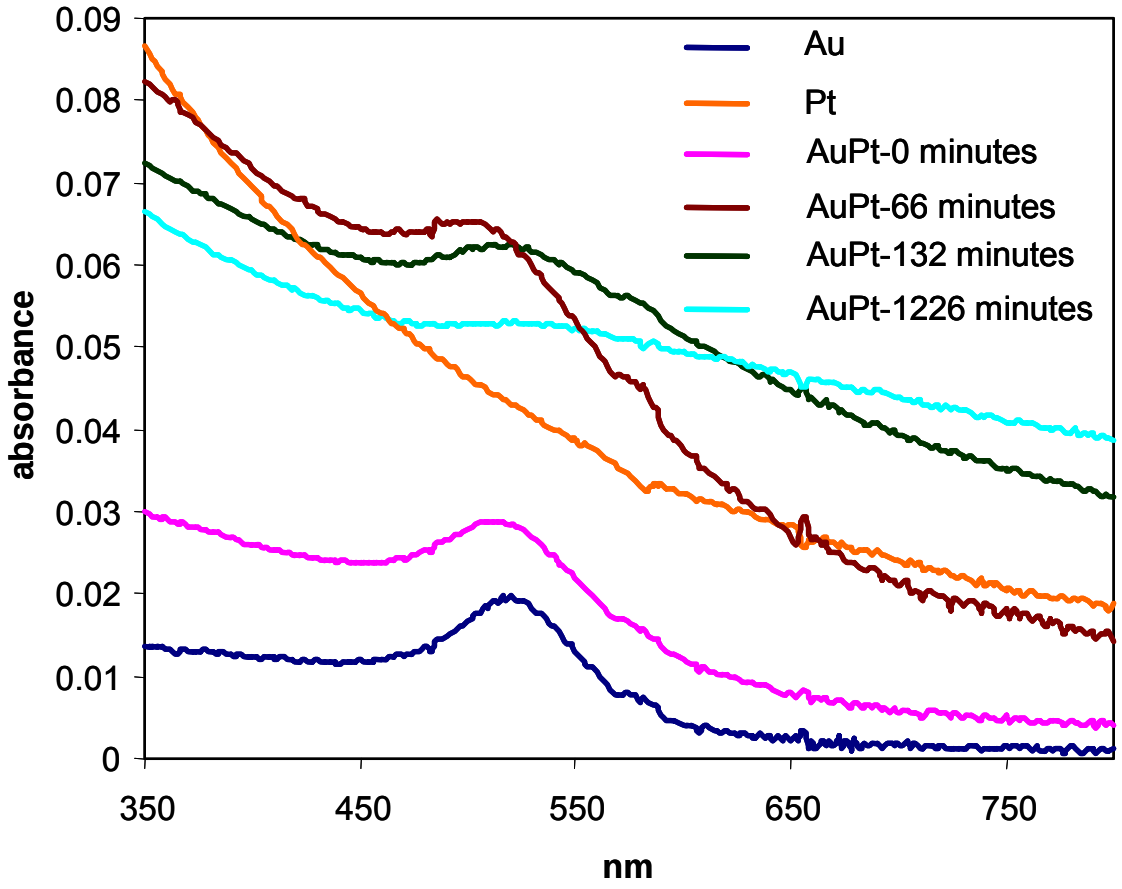

Figure 2.6. Time resolved UV-Visible spectra showing SPR absorption of individual Au, AuPt-0 minutes, AuPt-66 minutes, AuPt-132 minutes, and AuPt-1226 minutes. The spectrum of individual Pt NPs is included for comparison.

Table 2.1 shows the binding energies and atomic concentrations of Au and Pt in heteroaggregares by XPS studies. The Au 4f 7/2 binding energy is 84.130 eV (14.78% of the total atomic concentration), and is consistent with the metallic Au (NIST database). While Pt has two 4f 7/2 binding energies, one with 71.372 eV (82% of the total Pt) indicates the metallic Pt, and another with 72.626 eV (18% of the total Pt) belongs to the partially oxidized Pt component. Most metals (not including very inert Au) have surface oxides if not handled in air-free conditions. It is reasonable for Pt to have two components because the sample was thoroughly washed in the air with acetone and

ethanol to remove the stabilizing agent. It is well known that XPS is a surface technology. Although the penetration depth varies from samples to samples, usually the depth is no more than 10 nm. For large nanoparticles, the composition information by XPS reflects the composition of the material surface.[99] In this study, the average particle size of heteroaggregates is 26.2 nm. Therefore, the ratio of Pt to Au (85.21 to 14.78) indicates the Pt is concentrated at the tendrils. The sequential reduction method, TEM studies, UV-Visible studies, XPS studies, and XRD patterns strongly suggest the AuPt heteroaggregare nanostructures have phase pure Au cores and phase pure Pt tendrils.

Table 2.1. Binding energies and atomic concentrations of Au and Pt in AuPt heteroaggregate NPs by XPS.

Peak	binding energy (eV)	atomic concentration (%)
Pt 4f a 7/2	71.372	34.96
Pt 4f a 5/2	74.670	34.84
Pt 4f b 7/2	72.626	7.42
Pt 4f b 5/2	76.407	7.99
Au 4f 7/2	84.130	8.27
Au 4f 5/2	87.806	6.51

To further prove the phase pure structures, FE-STEM with EDX and EELS attachments were exploited to investigate elemental distribution information. Figure 2.7 shows the phase maps of AuPt heteroaggregate structures. The map of Pt component is spatially more diffuse than that of Au. This observation is consistent with the Pt tendrils extending from the Au cores, but the overlap in the X-ray lines complicates the

interpretation. Definitive evidence of the phase pure structure comes from the EELS measurements of a single particle with line scans across the particle (Figures 2.8). The atomic density of Au is concentrated on the core, and reaches the maximum at the particle center, while the Pt atomic density is concentrated at the periphery of the particle and has several maximums surrounding that of Au.

These quantitative data together with TEM, XRD, and UV-Visible and XPS studies clearly give an unequivocal picture of a pure Au core with pure Pt tendrils attached to the Au particle surfaces.

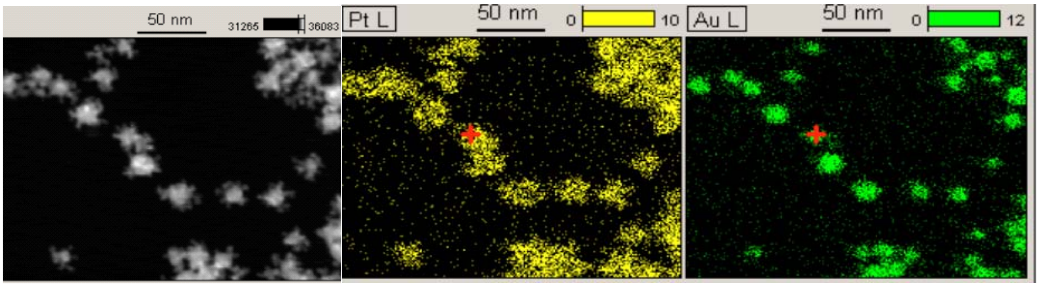

Figure 2.7. Images of FE-STEM with EDS showing a) AuPt heteroaggregate NPs, b) Pt map of AuPt heteroaggregate NPs, and c) Au map of AuPt heteroaggregate NPs.

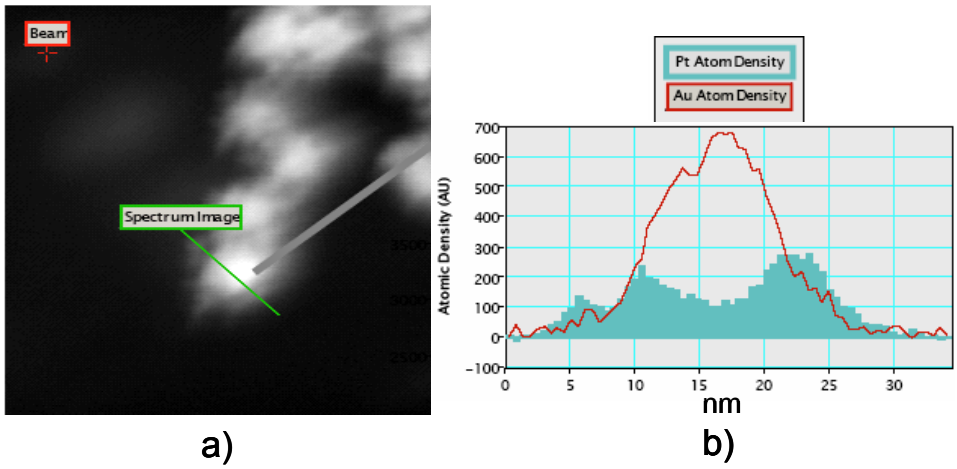

Figure 2.8. Atomic densities across one heteroaggregate nanoparticle by EELS showing a) linescan across one heteroaggregate nanoparticle, b) atomic densities of Au and Pt across the particle.

2.3.2. Syntheses and Characterization of AuPt Alloy NPs and NWs

AuPt alloy NPs were synthesized by a butyllithium reduction method. Butyllithium is often used as a strong base or nucleophile in organic syntheses, and rarely used as a reducing agent in nanoparticle syntheses.[100, 101] Chang and co-workers have synthesized TiC, ZrC, HfC, V_4C_3, NbC, and TaC NPs by a butyllithium reduction method.[101] In their method, $TiCl_4$, $ZrCl_4$, $HfCl_4$, VCl_3, $NbCl_5$, or $TaCl_5$ was reduced by butyllithium to generate colloid precursor followed by deposition of colloid and annealing at 600-1000^{o}C to produce metal carbide NPs. Due to high temperature annealing, the NPs aggregate and can not be re-dispersed in solvent.

Here, the same strategy was applied but annealing was accomplished in the solution instead of the solid state to synthesize metastable, dispersible AuPt alloy NPs. Reactions were carried out in octyl ether solvent with oleylamine as the stabilizing agent. First the precursors of Au and Pt were co-reduced by butyllithium at 78^{o}C to generate the colloid. The resulting dark brown colloid was further heated to 190-240^{o}C to form crystalline

AuPt alloy NPs. Figure 2.9a shows the low magnification TEM image of AuPt NPs. These particles show a narrow distribution with an average particle size of 2.5 nm (Figure 2.10). XRD measurement of the AuPt NPs exhibits a clear, well-defined XRD pattern (Figure 2.11, red pattern). The diffraction peaks of AuPt NPs are just between those of Au and Pt. According to Vegard's law, the XRD pattern is consistent with the pattern of an atom randomly distributed AuPt alloy system. Annealing these NPs at 700^{o}C in vacuum for 24 hours shows formation of Au-rich AuPt alloy phase and basically pure Pt phase (figure 2.11, blue pattern). This result is consistent with the phase diagram, and confirms the AuPt alloy is a metastable phase.

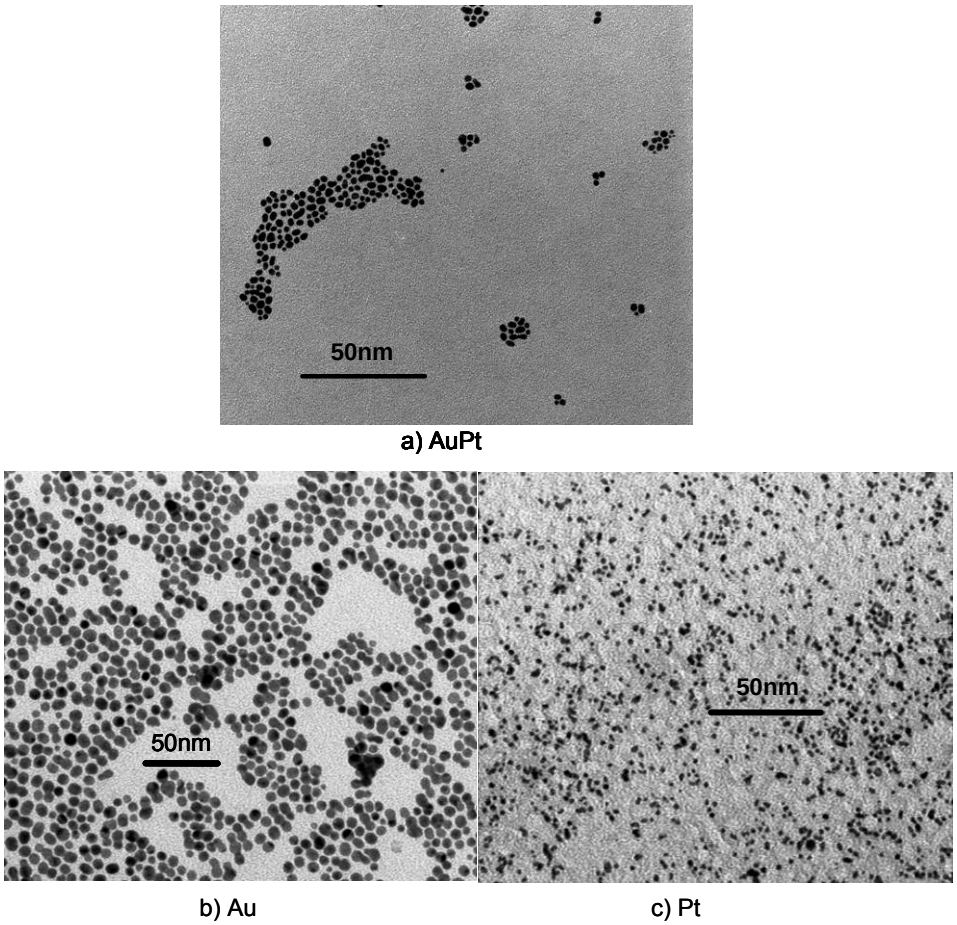

Figure 2.9. Low magnification TEM images showing a) AuPt alloy NPs, b) individual Au NPs, and c) individual Pt NPs.

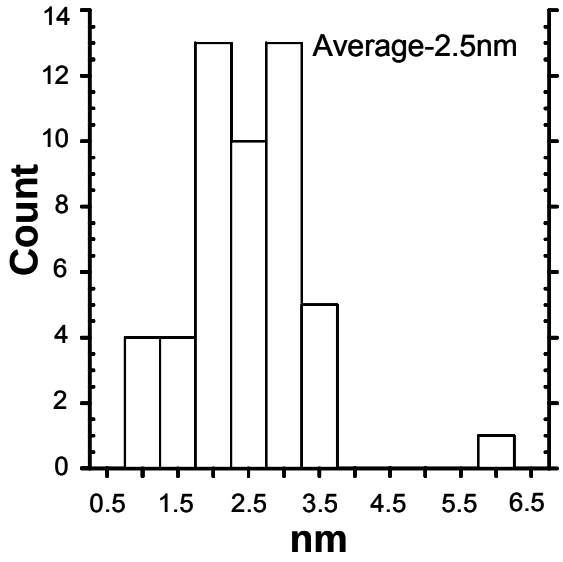

Figure 2.10. Histogram showing particle size distribution of alloy NPs.

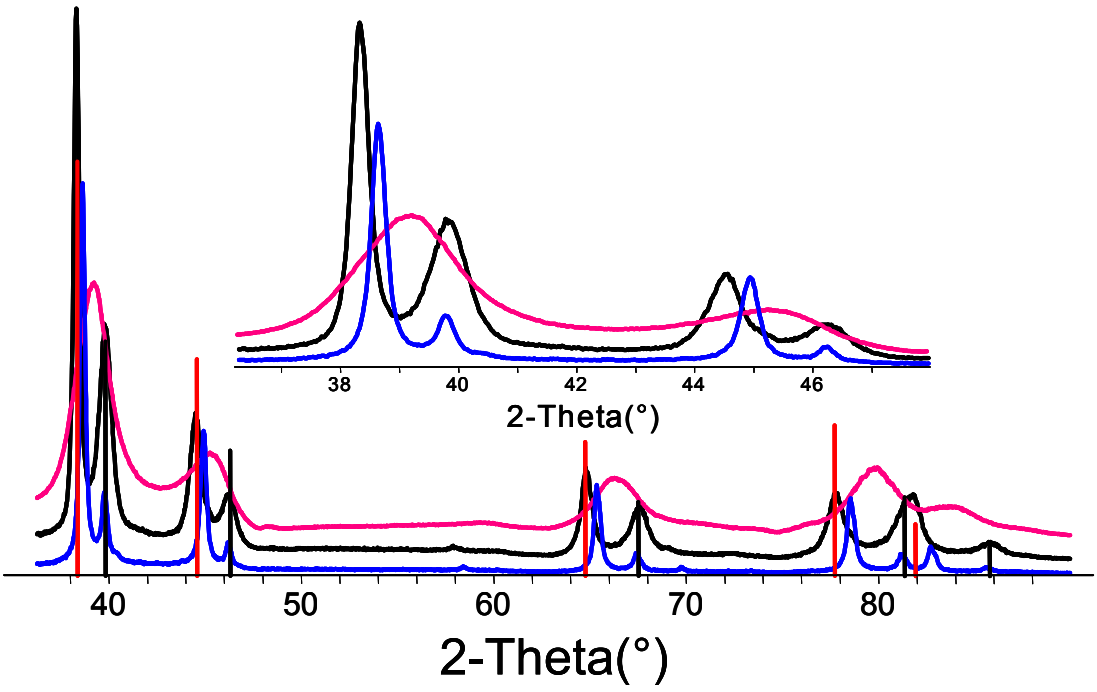

Figure 2.11. XRD patterns of AuPt systems. The red pattern-AuPt alloy NPs; the black pattern-AuPt NPs from control experiment (without butyllithium, other conditions is same as those of alloy NPs); the blue pattern-alloy NPs after annealing at 700^{o}C in vacuum for 24 hours. The vertical red lines indicate the diffraction from Au (JCPDS 01-1172), and the black lines indicate the diffraction from Pt (JCPDS 01-1311). The inset is the enlargement of XRD patterns.

Monometallic Au and Pt NPs can be synthesized by the same method. Figure 2.9b shows the TEM image of Au NPs. These NPs are spherical with an average particle size of 7.4 nm. Figure 2.9c shows the TEM image of Pt NPs. This butyllithium reduction method generated extremely small Pt NPs with an average particle size of 1.5 nm. The interesting phenomenon about the Pt nanoparticle synthesis is that a yellow solution was formed instead of a colloid after injection of Pt precursor solution to the butyllithium solution at 78^{o}C. The formation of yellow solution may suggest that a zero-valent compound was produced. After aging at 180^{o}C for 2 hours, a dark colloid was produced. In contrast, a reddish colloid, the sign of Au nanoparticle formation, was formed after the injection of Au precursor solution at 78^{o}C. For the synthesis of AuPt alloy NPs, a dark brown colloid was generated simultaneously after the injection of Au and Pt precursor solution to the reaction system, suggesting the formation of AuPt bimetallic colloid.

To prove that a rapid reduction is required for the formation of AuPt alloy NPs, control experiments without butyllithium were carried out. As stated above, the oleylamine acts as the reducing agent and also as the stabilizing agent. As the temperature was increased, the appearance of reddish colloid followed by the appearance of dark colloid suggests sequential reductions of Au and Pt precursors, and formation of phase separated structures. XRD pattern of resulting NPs (figure 2.11-black pattern) is consistent with the phase separated structures.

Data from XPS studies of AuPt alloy particles are shown in table 2.2. The overall ratio of Au to Pt is 53.9 to 46.1, which is close to the composition of the starting materials. The data show that alloy particles have two Pt components, which were already shown in heteroaggregate NPs. However, alloy particles contain two Au components, which is in

contrast to heteroaggregate NPs. One component with 84.148 eV (4f 7/2) is consistent with metallic Au, and another with 85.830 eV is consistent with oxidized Au (probably Au^{+}, 12.2% of total Au). It is well known that Au is very inert, and individual Au NPs usually do not contain surface oxide even handled in air conditions. The presence of oxidized Au component in AuPt alloy NPs suggests that the interaction between Au and Pt changes the electronic property of Au component, and make Au component of alloy NPs easier to be oxidized compared to individual Au NPs.

Table 2.2. XPS binding energies and atomic concentrations of Au and Pt in AuPt alloy. NPs

Peak	binding energy (eV)	atomic concentration (%)
Pt 4f a 7/2	71.273	18.92
Pt 4f a 5/2	74.538	19.33
Pt 4f b 7/2	72.501	8.65
Pt 4f b 5/2	75.945	6.98
Au 4f a 7/2	84.148	23.70
Au 4f a 5/2	87.820	16.74
Au 4f b 7/2	85.830	2.96
Au 4f b 5/2	88.616	2.74

To further probe the bimetallic structure, single particle analysis of the AuPt alloy NPs was carried out by TEM with EDS. Figure 2.12 shows dark field images of two regions selected for composition analysis by EDS. 13 particles were randomly selected, and EDS investigation shows all particles contain Au and Pt components (figure 2.12, figure 2.13,

and table 2.3). The compositions of some of these particles show large deviation from 1/1 ratio, which may be caused by relative low sensitivity of EDS for small particles. Furthermore, from statistic view, for overall 1/1 AuPt alloy NPs the percentage of particles showing small deviations should be higher than that of particles showing large deviations. The composition distribution of these 13 NPs is consistent with the statistic model. The average composition for these 13 NPs is 47.1% of Pt and 52.9% of Au. Again, this is close to the composition of the starting materials. Analysis of these particles by EDS indicates that these particles are bimetallic AuPt particles.

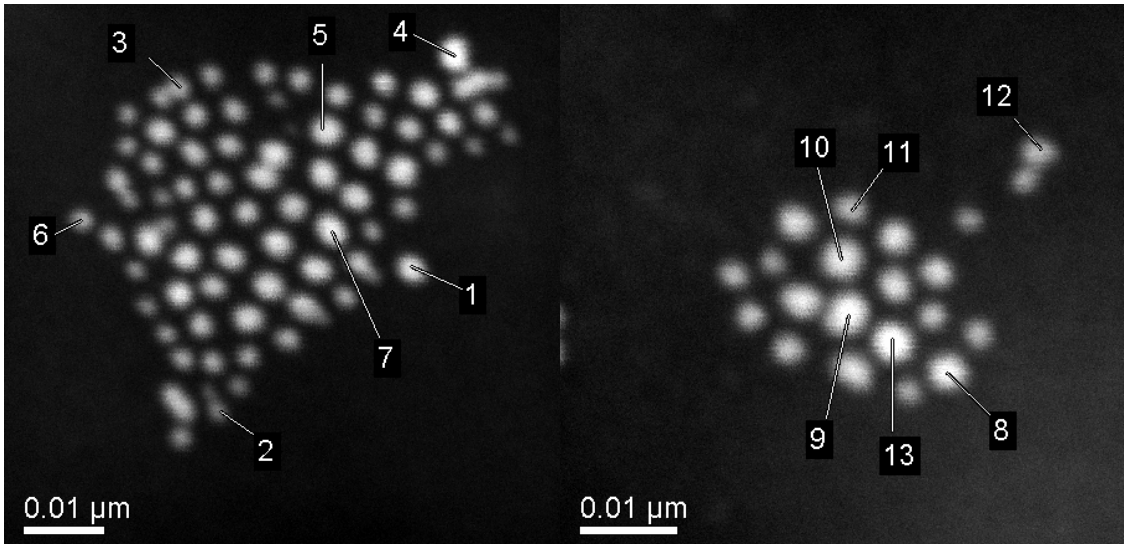

Figure 2.12. Dark field images of two regions in sample grid. 13 particles were randomly selected for EDS analysis.

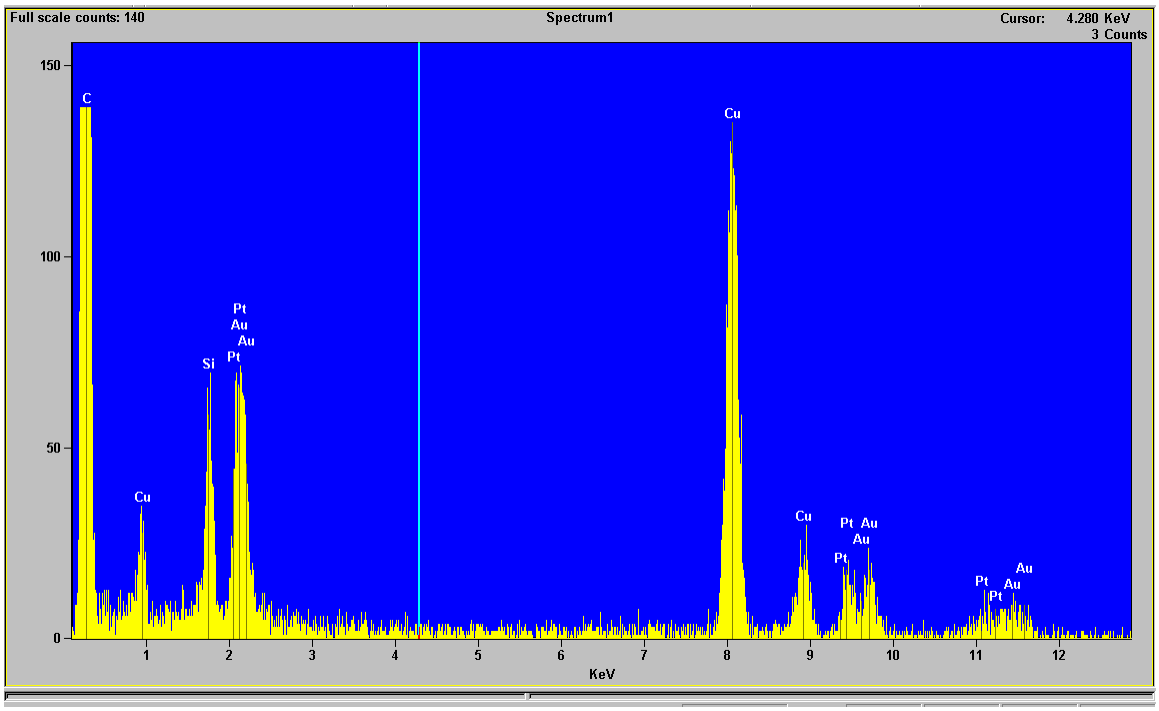

Figure 2.13. Representative EDS spectrum of one particle.

Table 2.3. Single particle composition analysis of 13 particles selected in figure 3.12.

# of particle	Pt% (atomic concentration)	Au%(atomic concentration)
1	45.9	54.1
2	48.8	51.2
3	49.5	50.5
4	67.1	32.9
5	28.6	71.4
6	55.5	45.5
7	43.0	57.0
8	26.0	74.0
9	43.3	56.7
10	49.5	50.5
11	53.0	47.0
12	65.8	34.2
13	35.8	64.2

Figure 2.14 shows the UV-Visible spectrums of AuPt colloid. The area of interest is around 520nm, where individual Au particles larger than 2 nm exhibit an SPR band. Clearly there is no absorption around 520nm. This result suggests that there are no individual Au NPs larger than 2 nm in the system, and likely indicates that no individual Au NPs exist because individual Au NPs would exhibit a shoulder in the spectrum due to poly-dispersiy. In contrast, heteroaggregate NPs show a shoulder near 520 nm, which indicates the Au cores are not fully covered by Pt tendrils.

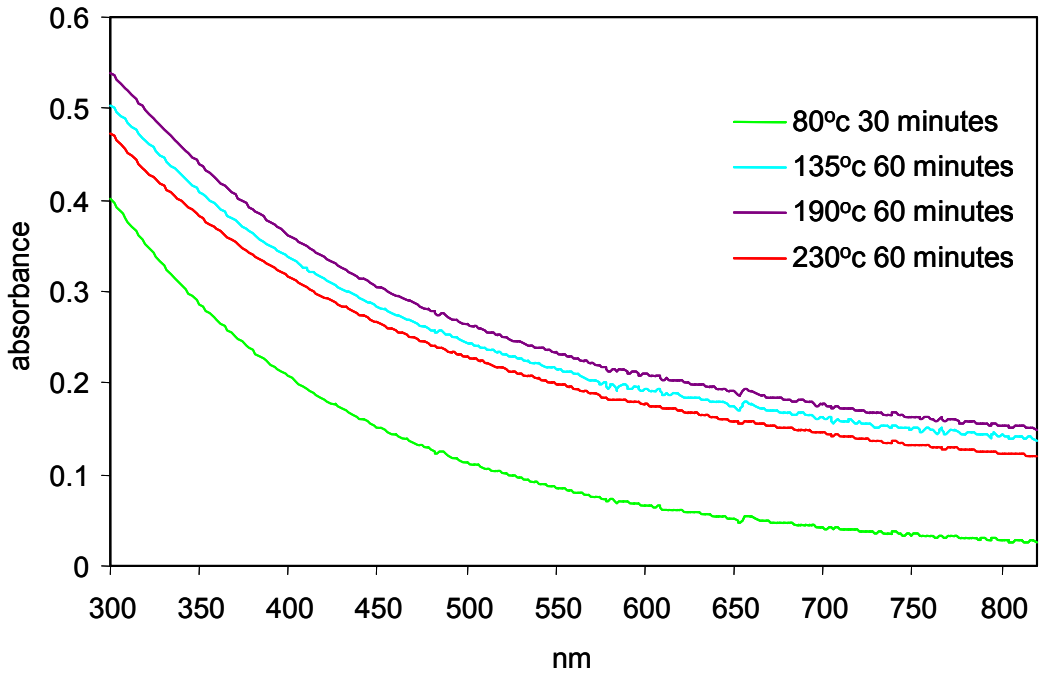

Figure 2.14. Time resolved UV-Visible study of colloids at different reaction stages. Sampling at different temperatures for different reaction times during temperature increasing process, other reaction conditions are same as the typical synthesis of alloy NPs.

The XRD studies, single particle analysis by EDS, and UV-visible studies clearly prove that these AuPt particles are alloys, i.e, a randomly distributed solid solution. To our knowledge, this is the first time that AuPt alloy particles have been synthesized in solution.

Figure 2.15 shows HRTEM images of AuPt alloy NPs. The most prominent lattice fringes (above 70%) have a ~2.30Å d-spacing. This d-spacing is consistent with the d-spacing of {111} surfaces of atom randomly distributed AuPt alloys.

An interesting phenomenon was found in the butyllithium reduction method. Butyllithium first reduces the precursors of Au and Pt to zero-valent metallic state. When the concentrations of compounds with zero-valent state reach a threshold point, they will nucleate to form NPs. For a typical synthesis of alloy NPs stated above, if just 20% of

precursor solution is injected into the butyllithium octyl ether solution, a clear solution is formed. However, if 30% of the solution is injected to butyllithium solution, a dark brown colloid is produced after several seconds. This high concentration of monomer is important for the following synthesis of NWs.

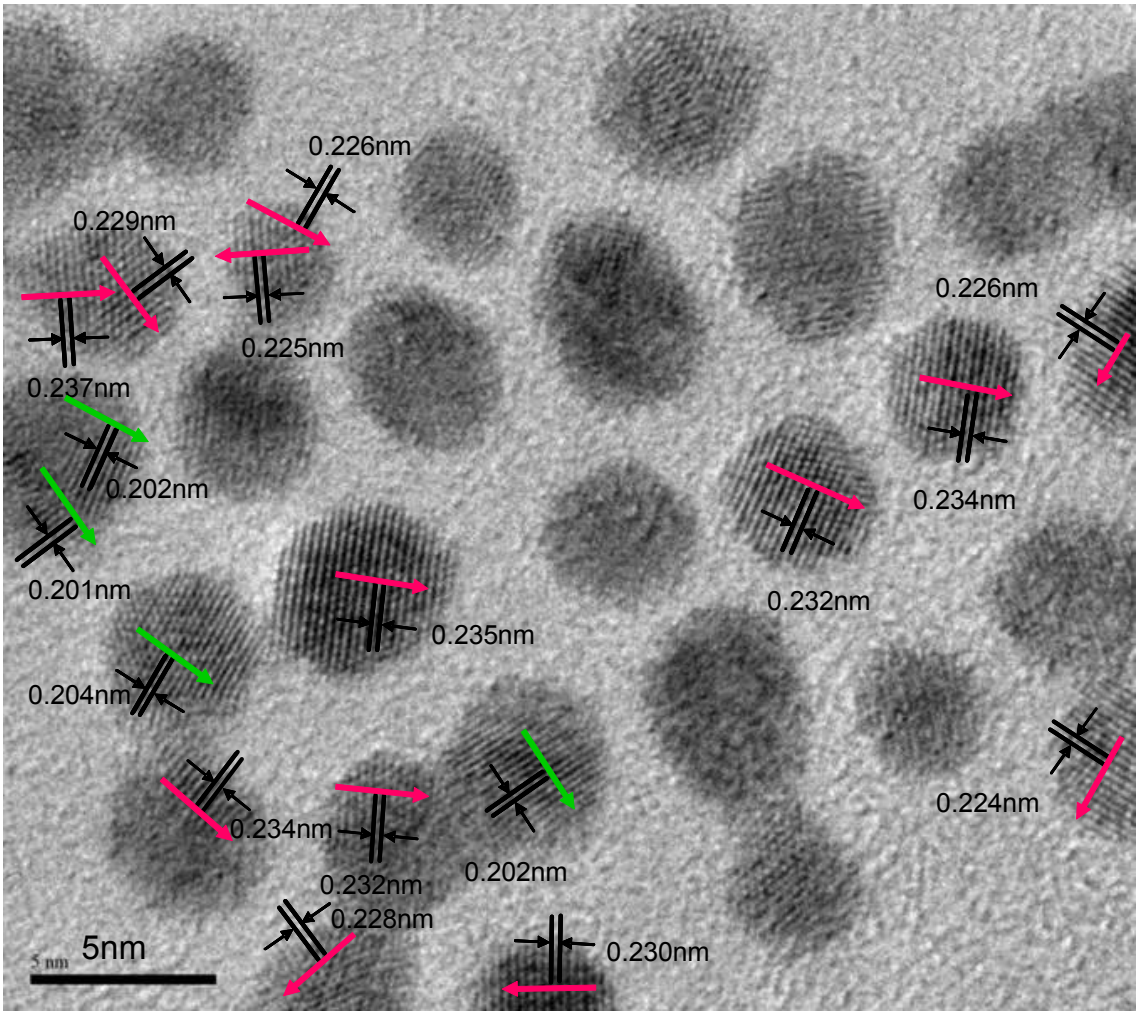

Figure 2.15. HRTEM image showing lattices of AuPt alloy NPs. The reddish arrows indicate the <111> direction, and the green arrows indicate the <100> direction.

The AuPt alloy nanowire synthesis is similar to that of the alloy NPs. The difference between the syntheses of NPs and NWs is that in the synthesis of NWs, a smaller amount butyllithium was used to reduce the precursor solution. First the solution of Au and Pt

precursor solution was injected into butyllithium solution, and a dark brown colloid was produced. After stirring at 78°C for 30 minutes, the temperature of the solution was increased to 190° and kept at 190°C for 2 hours. The formation of NWs at this temperature is very fast. After several minutes at 190°C the dark brown colloid (the color of alloy NPs in solvent) changed to a black colloid (the color of NWs in solvent). The length of the NWs was shortened with increasing reaction temperature.

Figure 2.16 shows the XRD pattern of NWs synthesized at 190°C for 2 hours. The diffraction peaks of AuPt NWs are between those of Au and Pt, indicating formation of a statistically distributed AuPt alloy. The pattern of the NWs is broader than that of alloy particles, indicating less crystalline materials synthesized at relative low temperatures (230°C for alloy particles, and 190°C for alloy NWs). UV-Visible spectrums of different colloids synthesized at different temperatures (not included) also show no absorption near 520 nm at any stage after co-reduction.

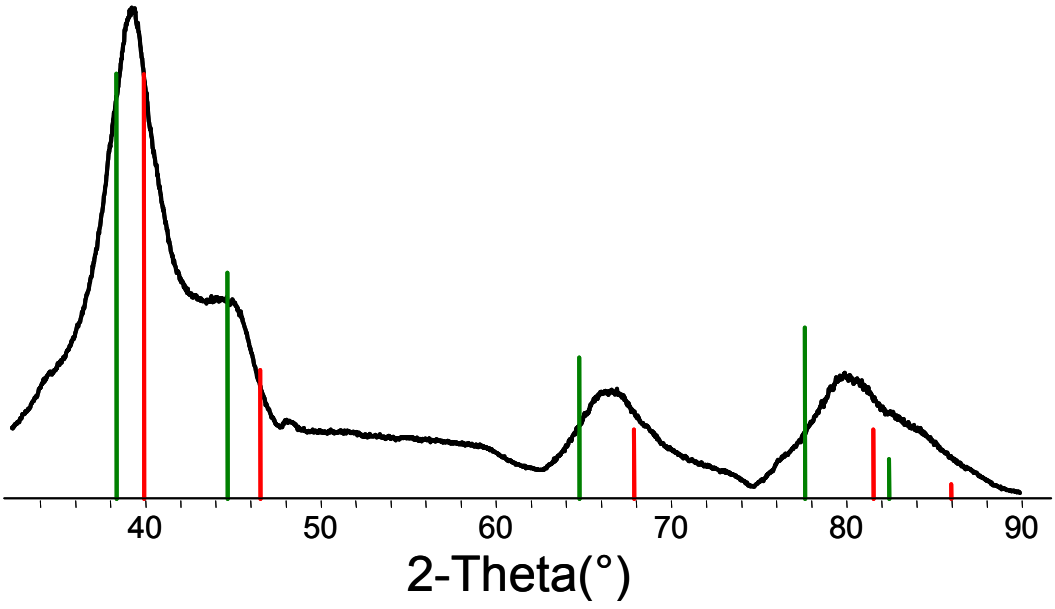

Figure 2.16. XRD pattern of AuPt NWs. The vertical green lines indicate the diffraction of Au (JCPDS 04-0784), and the red lines indicate the diffraction of Pt (JCPDS 04-0802).

Figure 2.17 shows low magnification TEM images of the AuPt NWs. These NWs are branched and multi-shaped, and the aspect ratio is approximately 5-25 with a 2-3 nm diameter. There are some NPs existing in the system, and these NPs account for less than ~5% (weight percent). In addition, NWs synthesized at higher temperatures (figure 2.17 b) are shorter, compared to the NWs synthesized at 190^{o}C. Using less butyllithium (0.8ml butyllithium cyclohexane solution, other conditions are same as described previously) will generate shorter and more branched NWs with NPs (figure 2.18). HRTEM images (Figure 2.19) show the lattice fringes of two individual NWs. The fringe spacing (~2.0Å) is consistent with the d-spacing of {200} surfaces. Three additional NWs were examined, and they were found to have lattices belonging to {200} surfaces. This behavior is in contrast to AuPt alloy NPs, where most lattices belong to the d-spacing of {111} surfaces. These NWs contain several domains with the same lattice fringes, and the growth directions match the <100> directions. However these <100> directions are not all in the long direction, indicating that these NWs are not a single crystal, and appear to be fused NPs.

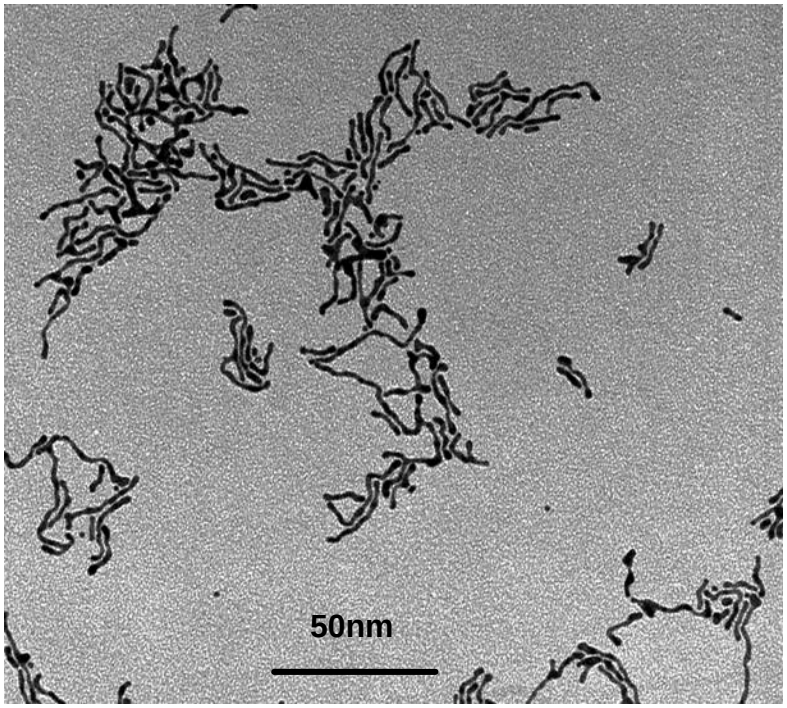

a) NWs synthesized at 190°C for 2 hours

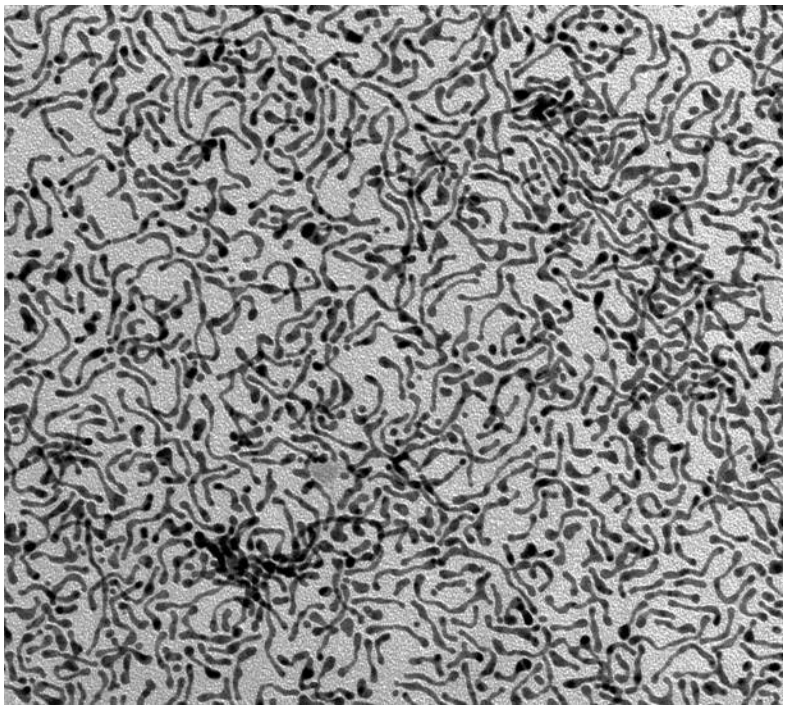

b) NWs synthesized at 210°C for 7 hours

Figure 2.17. Low magnification TEM images showing a) NWs synthesizeded at 190°C for 2 hours, and b) NWs synthesized at 210°C for 7 hours.

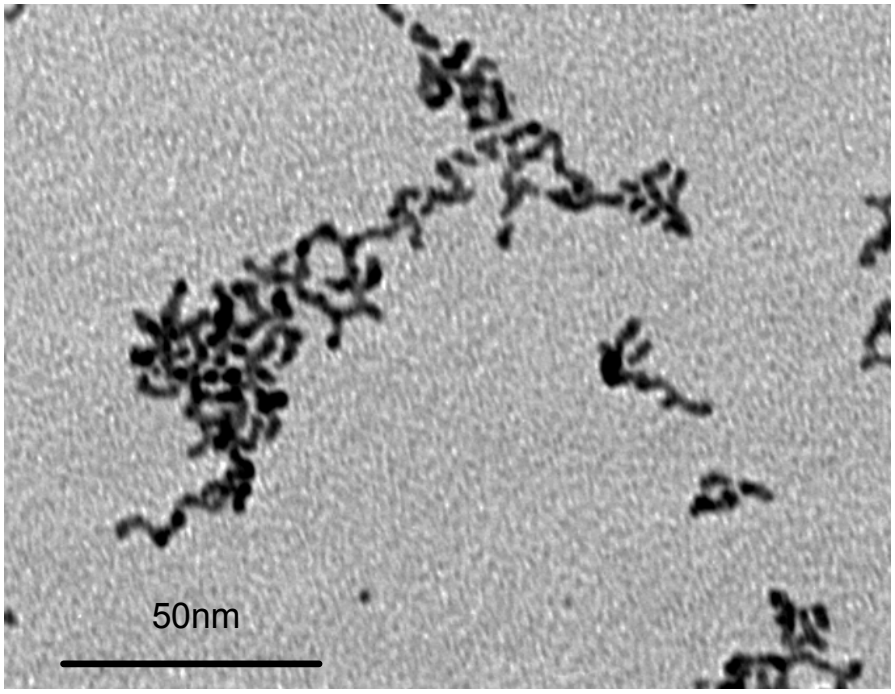

Figure 2.18. Low magnification TEM image of NWs synthesized by less amount of butyllithium.

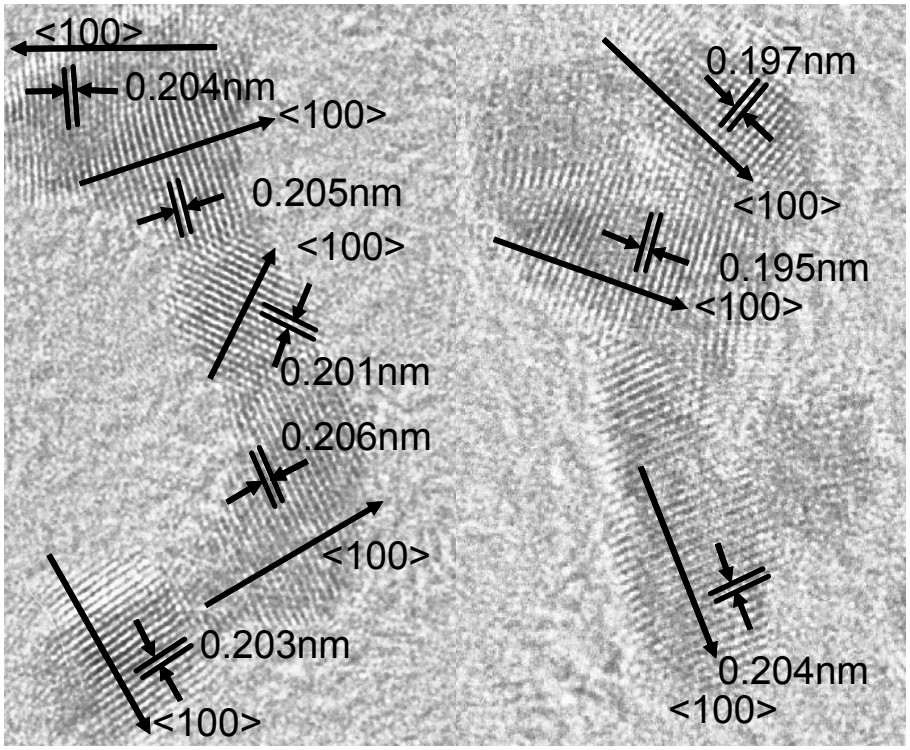

Figure 2.19. HRTEM image showing d-spacing of {200} surfaces of two NWs. The arrows indicate <100> direction.

2.3.3. CO Tolerant Hydrogen Catalytic Activation of Bimetallic AuPt Nanostructures

Low temperature polymer electrolyte membrane fuel cells (PEMFCs) have been intensely investigated in recent decades due to their high efficiency, small size and zero emissions.[102, 103] The fuel comes from pure H_2 or H_2-rich gas from reforming processes. The latter type of fuel usually contains a high level of CO.[104] The typical operating temperature range for PEMFCs is from 80°C to 100°C. In this temperature range, when the CO contaminated hydrogen fuel is applied in PEMFCs, the Pt electrode is poisoned due to strong bonding between the CO molecule and the Pt atom. This type of adsorption inhibits H_2 adsorption onto Pt surface, thus decreasing the cell performance. A commercial Pt anode electrocatalyst can tolerate no more than 10 ppm of CO in the fuel stream.[104, 105] Scientists use the term "CO-tolerance" to describe the magnitude of CO inhibition on hydrogen oxidation activity of catalysts. Much effort has been put into designing CO tolerant anode materials to accommodate higher CO concentrations. Bimetallic Pt materials are known to have an enhanced CO tolerant performance. Among these materials, RuPt is the most studied, and can tolerate 100-200 ppm CO.[106]

Another approach to solve this problem is to clean up the hydrogen fuel through a preferential CO oxidation pretreatment (PROX) before introduction to the fuel cell.[107] A good PROX catalyst should have a low H_2 oxidation and a high CO oxidation rate at an adequately low temperature. Pt group metals are currently used as PROX catalysts due to strong CO adsorption on surfaces.[108-111] Adding reducible oxides such as Fe_xO_y to the Pt catalyst can allow CO oxidation to occur at low temperatures.[112, 113] Another type of PROX catalysts is Au-based.[114-117] Au NPs with a small size (less than 4nm) are highly

active for low temperature CO oxidation. The high activity of the Au-based catalysts is due to a CO oxidation rate that is faster than that of H_2 oxidation. In this chapter, catalytic hydrogen oxidation in CO-H_2 mixtures was used to investigate the CO tolerance of AuPt heteroaggregate and alloy nanostructures as well as the PROX performance. Although the catalysts with enhanced CO tolerance in *thermal* catalytic hydrogen oxidation do not necessarily mean CO tolerant *electro*-catalysts in fuel cells, this catalytic method is certainly easier and faster than the electrochemical method and is a well established screening tool for potential CO tolerant anode materials.[106] The criterion for a potential CO tolerant material is that it has a high H_2 oxidation in a temperature range of 80-100^{o}C. This range is a typical PEMFC operating temperature range. The criterion for a good PROX catalyst is that it has a significantly faster CO oxidation than hydrogen oxidation at a given temperature.

Scheme 2.1 shows possible reactions of catalytic and electrochemical hydrogen oxidation in the presence of CO. In scheme 2.1, water gas shift reaction is not included. The tested temperature range for catalytic reactions in this study is from room temperature to 250^{o}C. Significant activity for water gas shift reaction of reducible oxides supported Pt catalysts is observed when the reaction temperature is above 200^{o}C.[118, 119] For heteroaggregate catalysts with or without Fe promoter, the CO conversion is completed below 200^{o}C. Furthermore, for heteroaggregate catalysts, most CO are consumed before significant water formation occurs. Therefore, for heteroaggregate catalysts, water gas shift reaction is possible, but is an insignificant reaction. For alloy catalysts, when the reaction temperature is above 126^{o}C, the CO conversion decrease as

the temperature increases, which suggest that the water gas shift reaction cannot be a significant reaction.

Scheme 2.1. Equations of catalytic and electrochemical $H_2/CO/O_2$ reactions.

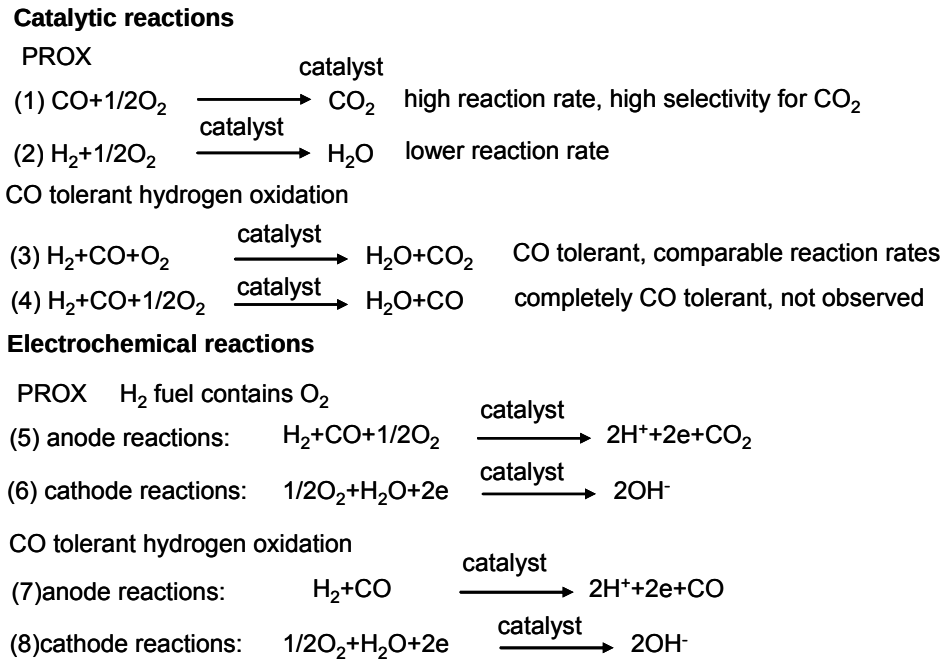

To keep a constant residence time of the reactants at different temperatures, the velocity of the reactant mixtures was fixed at 0.2085 m/s by varying reactant flow rates with reaction temperatures. The ramping rate of reactor furnace is 2^oC/minute. To simulate the CO contaminated H_2 fuel, the reaction stream was adjusted to give 50% H_2, 0.5% O_2, 0.2% CO and 49.7% Ar. The yields of H_2O and CO_2 are based on O_2-the limiting reactant. Therefore, the maximum yield of H_2O is 100% if all the O_2 is converted to H_2O, and the maximum yield of CO_2 is 20%. CO oxidation and hydrogen oxidation are parallel reactions as shown in Scheme 2.1. The sum of the yield of H_2O and CO_2 is equal to the O_2 conversion. To clarify, the percent of maximum concentration is used instead of yield in Figure 2.20-2.24, 2.26-2.27. The percent of maximum concentration is calculated by

dividing the real concentration by the maximum concentration. For example, at a certain temperature with an O_2 conversion of 70%, a yield of H_2O of 60% and a yield of CO_2 of 10%, the percent of maximum concentration of CO is 50% (10/20), and the percent of maximum concentration of H_2O is 60% (60/100). For O_2, the percent of maximum concentration of O_2 is 30% ((100-70)/100). Because the O_2 concentration can be obtained through the concentration of CO and H_2O, the percent of maximum concentration of O_2 is not included in Figure 2.20-2.23.

Figure 2.20 shows temperature programmable H_2 oxidations of pure Pt, AuPt alloy and heteroaggregate catalysts in the presence of 2000 ppm CO. The data were obtained after stabilized performances were achieved for all the catalysts (see experimental section). The pure Pt catalyst shows a 175^{o}C lightoff temperature and a 195^{o}C completion temperature for water formation, while without CO, the lightoff temperature is 50^{o}C and completion temperature is 60^{o}C. This result is consistent with the poisoning model of CO. CO strongly binds to the Pt surface, and inhibits H_2 and O_2 adsorption onto the surface. When the temperature reaches 140^{o}C, CO begins to desorb from the surfaces, and H_2 and CO oxidation begins to take over. The mixture of Au and Pt shows only a slightly lower lightoff temperature compared to the pure Pt catalyst. This result is as expected considering the particle size of Au NPs (for CO oxidation, a particle size less than 4 nm is required for Au catalysts). The performance of the AuPt heteroaggregate nanostructures is comparable to that of the pure Pt catalyst although the heteroaggregate catalyst shows approximately 10^{o}C enhancement (Figure 2.20). However, the AuPt alloy catalyst shows more than 60^{o}C enhancement compared to the pure Pt catalyst. The hydrogen oxidation and CO oxidation are initiated together, and water formation starts from 50^{o}C. The

maximum CO conversion of the alloy catalyst is 85%, and when the temperature is above 126^{o}C, the CO conversion decrease as the temperature increases, which may be caused by CO desorption from the catalyst surface at high temperatures. In contrast, the maximum of CO conversions of the heteroaggregate and pure Pt catalysts are 100%, and no significant CO conversion decrease at high temperatures was observed.

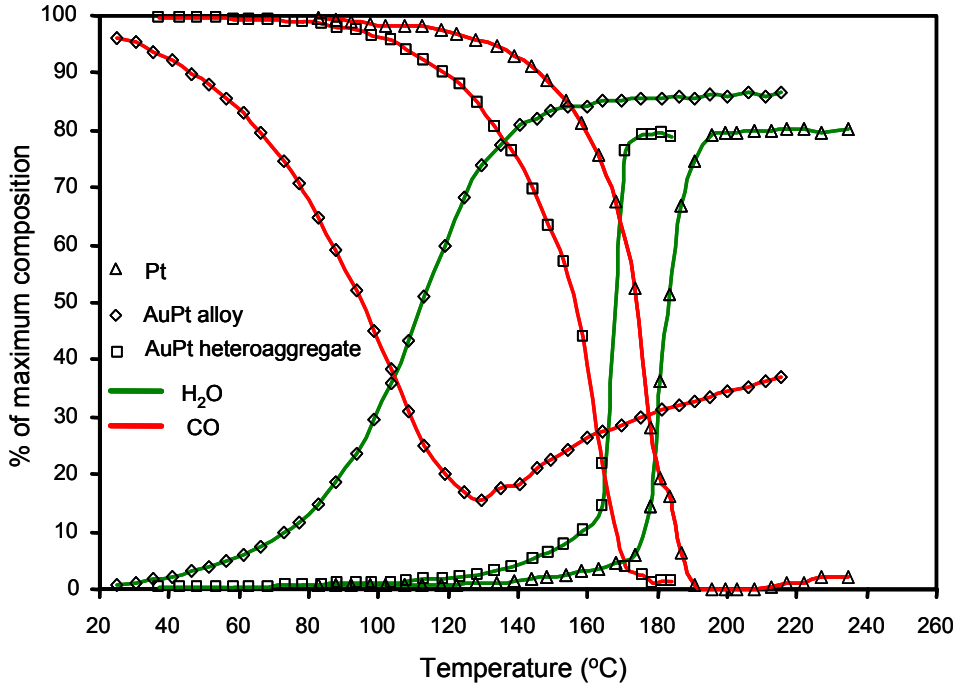

Figure 2.20. Comparison of temperature programmable reactions of Pt, alloy and AuPt heteroaggregate catalysts for H_2 oxidation in H_2/CO/O_2/Ar fuel streams (50:0.2:0.5:49.3) and fixed flow rate (0.2085m/s) in reactor. CO is normalized to inlet composition. H_2O composition is normalized with respect to H_2O generated if the limiting reactant O_2 were completely converted to H_2O.

For the pure Pt and the heteroaggregate catalysts, the temperature effect on reaction shows that hydrogen oxidation strongly depends on the concentration of CO, and accelerates as the CO concentration decreases. This behavior is due to the strong binding between the Pt atoms and the CO molecule. For significant hydrogen oxidation, these two catalysts require high CO conversions. However, the alloy catalyst does not require a

high CO conversion. Table 2.4 lists the CO conversions of the pure Pt, alloy and heteroaggregate catalysts at an H_2O yield of 15%. For the pure Pt catalyst, the CO conversion is 73%. The heteroaggregate catalyst shows a CO conversion of 80% at the same yield of H_2O. In contrast, the alloy catalyst only shows a CO conversion of 35%. The same trend of concentrations of the reactants and products of pure Pt and heteroaggregate nanostructures strongly indicates that the mechanism is same, i.e, CO oxidation prior to H_2 oxidation, and they are PROX catalysts (Scheme 2.1, equation 1-2). The catalytic behavior of the alloy catalyst suggests that the AuPt alloy is a CO tolerant catalyst (Scheme 2.1, equation 3).

Table 2.4. The CO conversions of the pure Pt, alloy and heteroaggregate catalysts at an H_2O yield of 15%.

Catalysts	H_2O yield (%)	CO conversion (%)	selectivity for CO_2 (%)
Pt	15	73	49
AuPt heteroaggregate	15	80	52
AuPt alloy	15	35	32

Figure 2.21 shows the performances of three sequential runs of the alloy catalyst. An enhancement in both CO and H_2 oxidation was observed from the first run to the third run. The catalyst was stabilized after three runs. In contrast, the pure Pt and heteroaggregate catalysts do not show significant difference from run to run. For heterogeneous catalysts, it is normal that the catalytic performance of the first several hours is different with the following performance. This phenomenon can be caused by the ligand leaching or surface reconstruction. For the alloy catalyst, the most likely reason is the oleylamine

ligand leaching, leading to more free catalytic sites for reactant adsorption. The alloy NPs were found to be difficult to remove the ligands. After washing with ethanol five times, these NPs are still redispersible in toluene. For dispersing NPs into solvent, the ligand is required to prevent NPs from aggregation and precipitation. The dispersibility of the AuPt alloy NPs after five washings with ethanol suggested that the NPs are still stabilized by sufficient oleylamine. In contrast, after washing with ethanol two times, the heteroaggregate NPs are not redispersible in toluene.

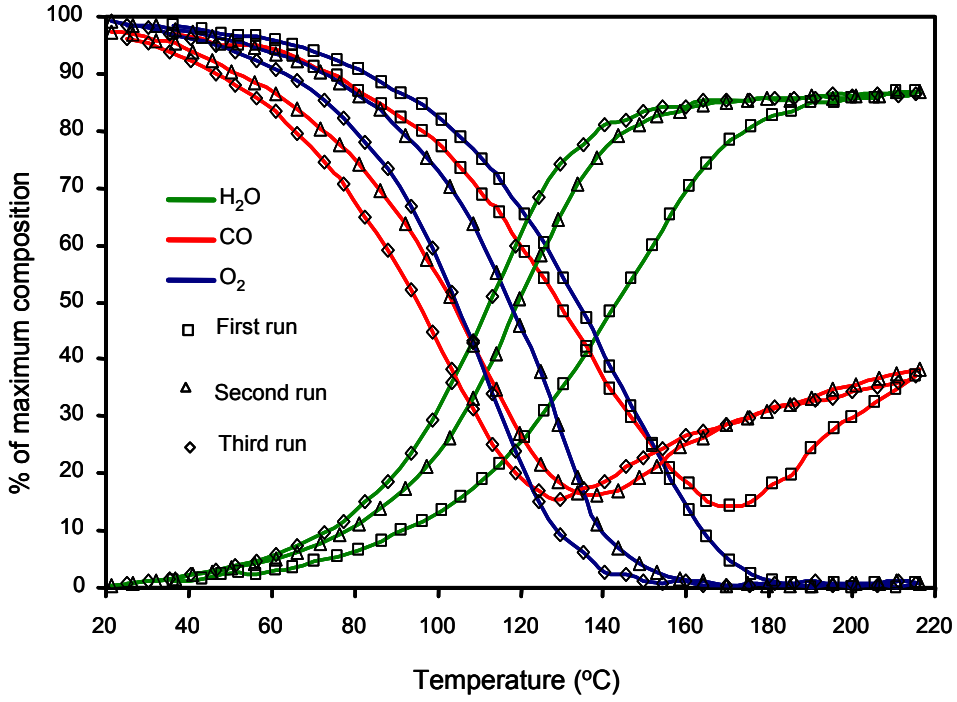

Figure 2.21. Comparison of three runs of temperature programmable reactions of AuPt alloy catalyst for hydrogen oxidation in $H_2/CO/O_2/Ar$ fuel streams (50:0.2:0.5:49.3) and fixed flow rate (0.2085m/s) in reactor. CO is normalized to inlet composition. H_2O composition is normalized with respect to H_2O generated if the limiting reactant O_2 were completely converted to H_2O.

To our surprise, using steel-CO cylinder instead of aluminum-CO cylinder results in a significant enhancement in the heteroaggregate catalyst. Figure 2.22 and Figure 2.23 shows the difference of the heteroaggregate and the alloy catalysts using different CO

cyclinders. The lightoff temperature of water formation of the heteroaggregate catalyst is 50°C lower than that of the aluminum-CO cylinder. It is interesting to note that the catalytic *behavior* of the heteroaggregate catalyst is very similar in both cases except that the reactions occur at lower temperatures using the steel cylinder CO. In contrast, there is no significant difference in the AuPt alloy activity with either the steel or aluminum CO tanks. These results indicate that an impurity in the steel-CO cylinder significantly enhances the catalytic performance of the heteroaggregate catalyst but not the alloy. The possible impurity is iron carbonyl, which was detected by FT-IR and EDX in this study and by other research groups.[120]

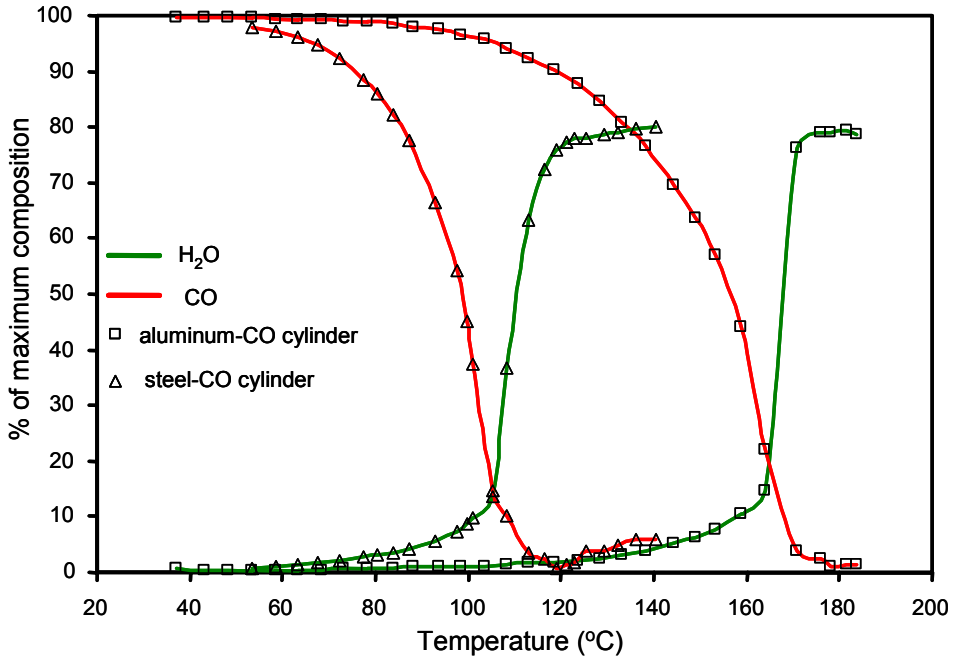

Figure 2.22. Comparison of temperature programmable reactions of AuPt heteroaggregate catalyst for H_2 oxidation in $H_2/CO/O_2/Ar$ fuel streams (50:0.2:0.5:49.3) with steel or aluminum-CO cylinders and fixed flow rate (0.2085m/s) in reactor. CO is normalized to inlet composition. H_2O composition is normalized with respect to H_2O generated if the limiting reactant O_2 were completely converted to H_2O.

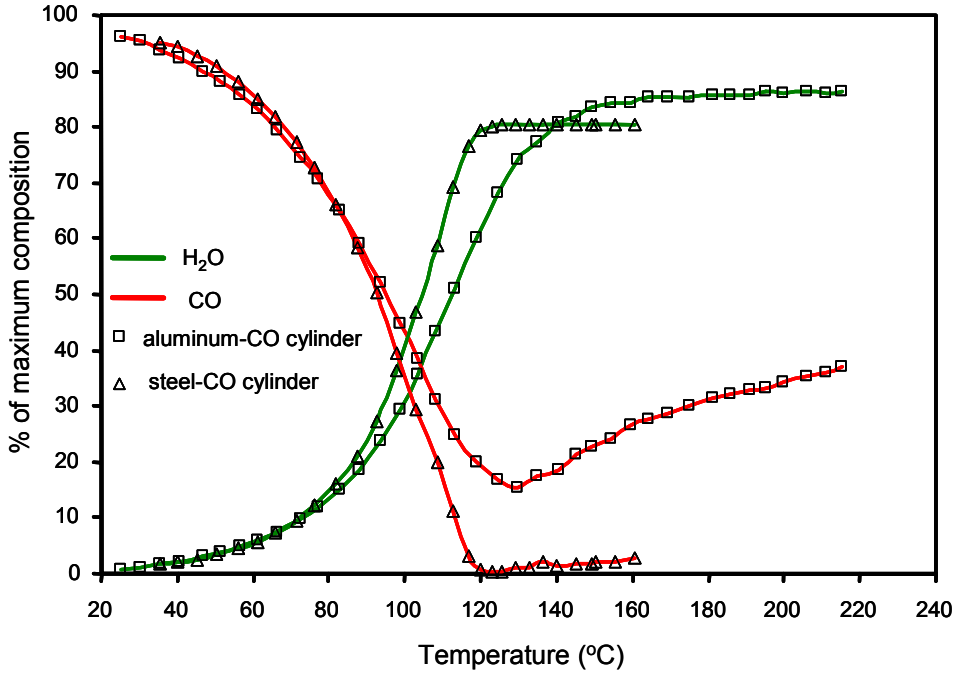

Figure 2.23. Comparison of temperature programmable reactions of AuPt alloy catalyst for H_2 oxidation in $H_2/CO/O_2/Ar$ fuel streams (50:0.2:0.5:49.3) with steel or aluminum-CO cylinders and fixed flow rate (0.2085m/s) in reactor. CO is normalized to inlet composition. H_2O composition is normalized with respect to H_2O generated if the limiting reactant O_2 were completely converted to H_2O.

To further probe the effect of iron promoter on catalytic behavior, the heteroaggregate catalyst with was prepared and subsequently doped with $Fe(NO_3)_3$. Figure 2.24 shows the catalytic performance of the heteroaggregate catalyst with and without Fe promoters. Before catalytic measurements, the catalysts were reduced in hydrogen at 200°C for three hours. The catalytic activity increases as the Fe loading increases. At the ratio 1/2 of Pt/Fe (weight/weight), the best performance was achieved, and no enhancement was observed when the Fe loading was further increased. At this ratio, the performance is very similar to that of the steel-CO cylinder, indicating that the enhancement of the steel-CO cylinder is due to iron carbonyl. Calcination of the catalyst under O_2 instead of H_2

gives a similar result, suggesting that the active Fe component is probably Fe_xO_y, which is a reducible oxide and can provide lattice oxygen to facilitate CO oxidation.

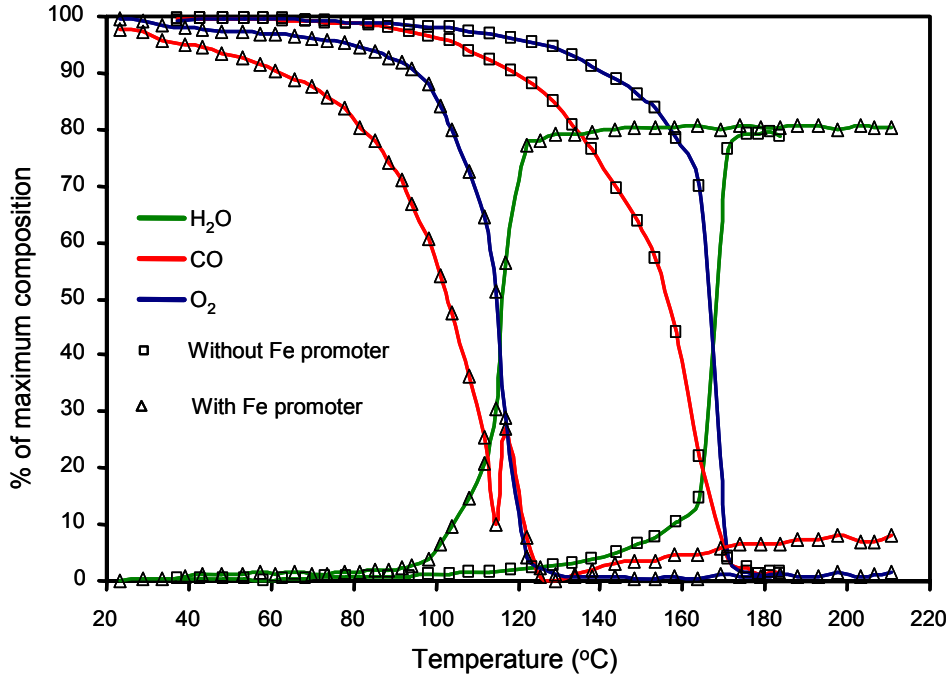

Figure 2.24. Comparison of temperature programmable reactions of AuPt heteroaggregate catalysts with or without Fe promoter for hydrogen oxidation in $H_2/CO/O_2/Ar$ fuel streams (50:0.2:0.5:49.3) and fixed flow rate (0.2085m/s) in reactor. CO is normalized to inlet composition. H_2O composition is normalized with respect to H_2O generated if the limiting reactant O_2 were completely converted to H_2O.

The control experiments of the Pt and the Au/Pt mixture catalysts with the $Fe(NO_3)_3$ promoter also show an enhancement. The Pt and the mixture catalysts with the $Fe(NO_3)_3$ promoter show a even higher CO oxidation at low temperatures. However, the completion temperatures of CO conversion and H_2O formation for these two catalysts are at least 20°C higher than that of the heteroaggregate catalyst with $Fe(NO_3)_3$ promoter, and no sharp lightoff behavior was found in these two catalysts. The CO oxidation occurs at lower temperatures, and CO oxidation gradually increases as the temperature increases. This phenomenon is consistent with literature reports, where reducible oxides enhance

CO oxidation at low temperatures.[112, 113, 121-126] However, for the AuPt heteroaggregate catalyst with the $Fe(NO_3)_3$ promoter or using steel-CO cylinder, sharp lightoff behavior was observed. In addition, the Pt and the Au/Pt mixture catalysts do not show enhancement using the steel-CO cylinder. The different behavior between these catalysts suggests that the Au component in the heteroaggregate NPs facilitates the CO oxidation and the deposition of iron carbonyl onto NPs when the steel-CO cylinder is used.

Although the same enhancement can be obtained using either the $Fe(NO_3)_3$ promoter or the iron carbonyl from the steel-CO tank, the iron carbonyl is more efficient in enhancing the CO oxidation and more selective regarding the absence of enhancement of the Pt and the Au/Pt mixture catalysts using the steel-CO cylinder. The subsequent experiments described in this chapter utilized iron carbonyl as the Fe promoter source. Several more experiments using the steel-CO cylinder under different conditions were carried out. All the following reactions were done using the steel-CO cylinder. Figure 2.25 shows the catalytic performance of the heteroaggregate structure in O_2 deficient conditions (O_2-0.2%, CO-0.45%). The selectivity for CO_2 formation is in the range of 55-75%, and decreases with increasing temperature. Again, this result shows that the heteroaggregate catalyst is a PROX catalyst.

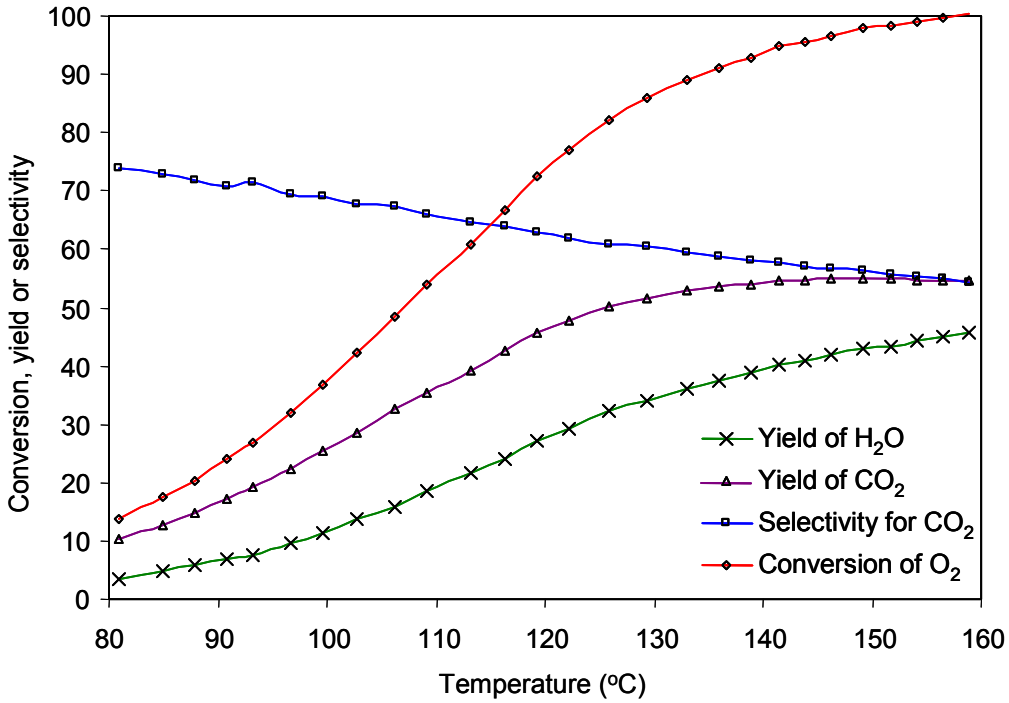

Figure 2.25. Temperature programmable reaction using the steel-CO cylinder with O_2 deficient condition showing AuPt heteroaggregate catalyst for H_2 oxidation in $H_2/CO/O_2/Ar$ fuel streams (50:0.45:0.2:49.35) and fixed flow rate (0.2085m/s) in reactor. Yields of CO_2 and H_2O are based on O_2-the limiting reagent. The selectivity for CO_2 is calculated by dividing the yield of CO_2 by the conversion of O_2.

Optimizing CO concentrations for the heteroaggregate catalyst using the steel-CO cylinder shows that, with 1000ppm CO, the lightoff temperature of hydrogen oxidation drops to 84°C and the completion temperature drops to 92°C (Figure 2.26). This temperature range is in the range of PEMFC operating temperatures. In addition, the conversion of CO is close to 100% near 80°C, and the water formation is insignificant. For example, at 84°C the conversion of CO is close to 100% with a 90% selectivity of CO_2. This result suggests that the AuPt heteroaggregate nanostructure is an excellent PROX catalyst with a high conversion of CO and a high selectivity for CO_2.

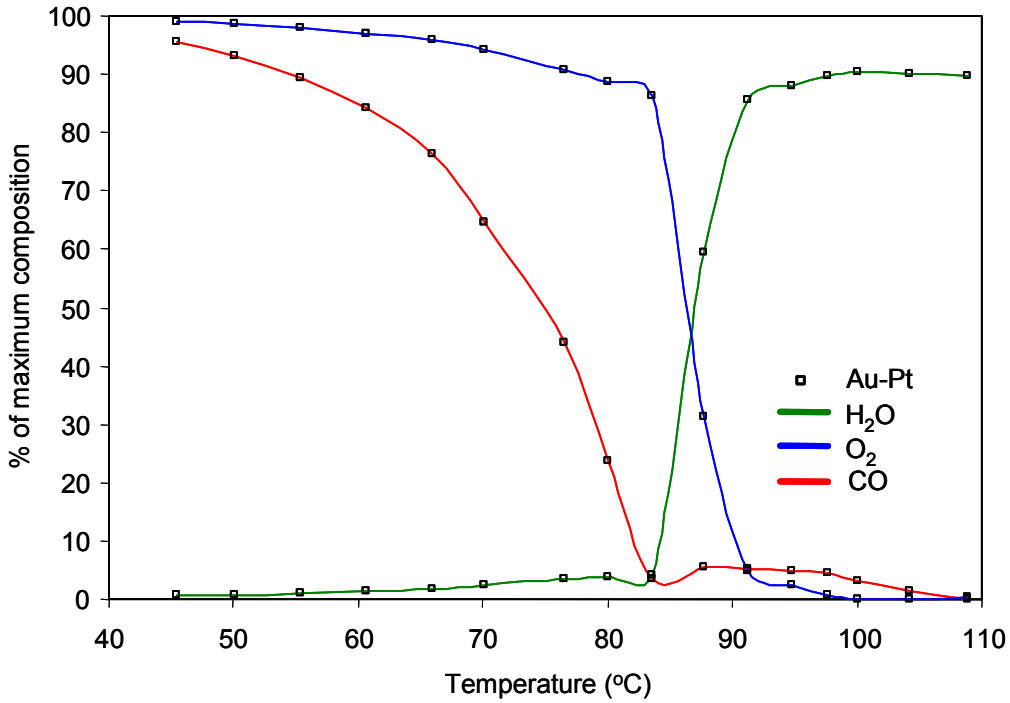

Figure 2.26. Temperature programmable reaction using the steel-CO cylinder showing the AuPt heteroaggregate catalysts for H_2 oxidation in $H_2/CO/O_2/Ar$ fuel streams (50:0.1:0.5:49.4) and fixed flow rate (0.2085m/s) in reactor. CO and O_2 are normalized to inlet composition. H_2O composition is normalized with respect to H_2O generated if the limiting reactant O_2 is completely converted to H_2O.

The CO tolerant performance of hydrogen catalytic activation of the AuPt alloy nanoparticle catalyst using the steel-CO cylinder was tested with the same method as the AuPt heteroaggregate structure. Figure 2.27 shows the performance using 2000 ppm CO. The water formation completion temperature is nearly the same as that of the AuPt heteroaggregate nanostructures using the same cylinder. While there is not a pronounced lightoff temperature, the formations of CO_2 and water begin together at 50°C, indicating that the mechanism is different from that of AuPt heteroaggregate structures, where PROX bbehavior was observed. With 1000 ppm CO, the water completion temperature is ca. 100°C, and 6°C higher than that of heteroaggregate structure in the same conditions. In addition, the CO_2 selectivity is significant lower than that of heteroaggregate structures

due to coincidence of CO and hydrogen oxidation. Although the water completion temperature is slightly higher than that of heteroaggregate structures, considering the lower temperature for water formation, these alloy NPs are potentially good CO tolerant catalysts for hydrogen oxidation.

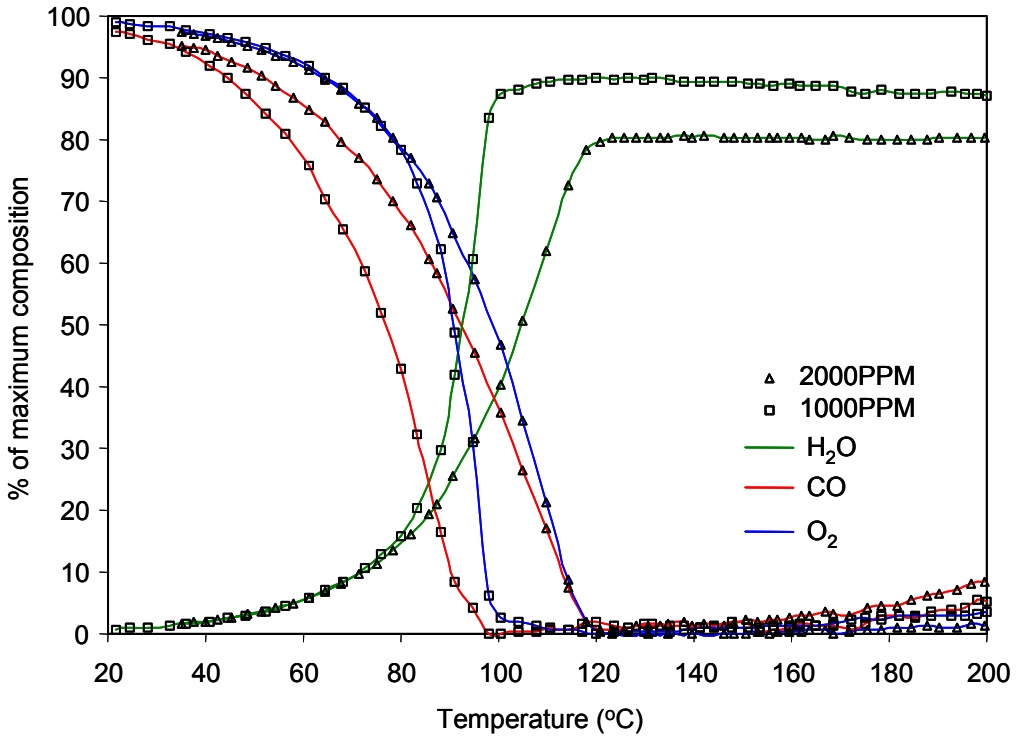

Figure 2.27. Comparison of temperature programmable oxidation reactions of the AuPt alloy nanoparticle catalysts using the steel-CO cylinder for hydrogen oxidation with different CO concentrations in $H_2/CO/O_2/Ar$ fuel streams (50:0.1-0.2:0.5:49.4-49.3) and fixed flow rate (0.2085m/s) in reactor. CO and O_2 are normalized to inlet composition. H_2O composition is normalized with respect to H_2O generated if the limiting reactant O_2 were completely converted to H_2O.

2.4. Discussion

2.4.1. Shape Control of AuPt Bimetallic Nanostructures

At equilibrium, nanomaterials typically have a spherical shape, and are bound by {111} surfaces. Other shapes are determined by the relative growth rate of different

facets. Specifically for fcc nanomaterials, shapes are determined by the relative growth rates of {111} and {100} surfaces.[39] For example, if <111> direction growth is favored, spherical NPs are formed. If <100> direction growth is favored, usually NWs or nanocubes are produced. In addition, surfactants also play an important role in controlling size and shape. Strong ligands generate small nanostructures due to energy release obtained from bonding between the metal atom and the surfactant molecule. Ligands may also selectively bind to some surfaces to favor anisotropic growth. Besides the above issues, Au and Pt are immiscible in a wide range of temperatures and compositions. According to the phase diagram[91] (thermodynamic behavior of bulk materials), in the range of the reaction temperatures, AuPt bimetallic nanomaterials should exhibit phase-separated structures, and the alloy phase can only be generated by kinetic control. In this work, the selection of shape or phase can be explained by the above concepts.

First let us discuss the formation of AuPt heteroaggregate nanostructures. Due to the phase behavior, using a soft reducing agent (oleylamine) and a sequential reduction method, the phase separated structure is not surprising. All of the core-shell or heteroaggregate structures satisfy the phase diagram. However the heteroaggregate nanostructures have less contacting area than core-shell structures, and can further decrease the strains caused by immiscibility of Au and Pt. Further stabilizing effect for heteroaggregate structures comes from the surfactant. Oleylamine selectively binds to some surfaces, and decreases the growth rate of these surfaces. Therefore the growth of other surfaces not bound tightly by oleylamine is favored, and generates individual rod-like shaped Pt NPs. For this reason, Pt components form the tendril shape in AuPt

heteroaggregate structures. Moreover, nucleation on Au templates is an energy favorable process, which favors the heteroaggregate structure.

The AuPt alloy phase can only be synthesized by kinetic control according to the phase diagram. Because of the higher reduction potential, the Au precursor is much easier to reduce compared to the Pt precursor. The common reducing agents usually produce phase separated AuPt bimetallic structures. Here, a very strong reducing agent-butyllithium was used as the reducing agent. This rapid reduction method prevents phase separation, and traps the metastable alloy phase (favored by entropy). Secondly, phase diagrams are generated by solid state method, and represent the properties of bulk materials. In our work, all the reactions are carried out in the solution. The solution may provide another stabilizing effect for the metastable phase. Recently there are several examples reported about metastable phases synthesized by the solution method.[57]

The shapes of AuPt alloys can be explained by the relative growth rate of {111} and {100} surfaces. {111} surfaces have lower surface free energy than {100} surfaces. At equilibrium, the growth rate in the <111> direction is favorable, and the resulting particles are bound by {111} surfaces. HRTEM studies confirm this growth direction. The most clearly seen lattices of AuPt alloy NPs belong to the d-spacing of {111} surfaces. In contrast, the NWs can only be produced by <100> direction growth through kinetic control, which was proven by HRTEM studies. The image shows that all the clearly distinguishable lattices of NWs examined belong to d-spacing of {200} surfaces, indicating the alloy NWs are favored by the <100> direction growth.

For the anisotropic growth of AuPt alloy NWs, the most important factor is the concentration of butyllithium. More butyllithium simply produces NPs, as shown in the

synthesis of alloy particles. Less butyllithium generates a mixture of shorter branched NWs and NPs. It is generally believed that a high concentration of monomer is needed to creat 1D nanostructures.[72] This high concentration of monomer provides a route for atoms to add or remove from the surfaces to adopt optimal positions. In this system, the monomer is the reduced Au and Pt complexes. We designed two experiments to prove the importance of a reduced complex. The first experiment is as follows: in a typical synthesis of AuPt alloy nanomaterials, 20% of the precursor solution was injected into butyllithium octyl ether solution, and a clear solution was generated; conversely, if more precursor solution (for example 30%) was injected into the same concentration of butyllithium solution, a dark brown colloid is generated. This experiment indicates that butyllithium first reduces the precursors to low oxidation state compounds. One possible explanation is that when the concentration of these compounds reaches a threshold point, they will nucleate to form NPs. The second experiment was designed to investigate the effect of concentration of butyllithium on nucleation. In a typical synthesis, 20% of the precursor solution was injected into the butyllithium solution, and a clear solution was generated; continuously adding more butyllithium to the reaction mixture finally resulted in a dark brown colloid. This experiment indicates that a high concentration of butyllithium helps nucleation.

Varying the amount of butyllithium will vary the concentration of low oxidation state compounds, which are the monomers for anisotropic growth. Higher concentrations of butyllithium decrease the concentration of monomers, and results in particles. This result is consistent with the formation of alloy particles using more butyllithium. Lower concentrations of butyllithium do not reduce all of the precursors, and leave some

oxidized precursors in solution. When the temperature of the mixture is increased, these oxidized precursors are reduced by oleylamine (or anions generated by reaction between oleylamine and butyllithiun) to form particles, along with NWs through monomers. This result is consistent with the observation of a mixture of shorter branched NWs and NPs using lower concentrations of butyllithium. Furthermore without butyllithium, heteroaggregate particles were generated by sequential reduction of precursors by oleylamine. This is a one pot synthesis of heteroaggregate NPs, which was done in decahydronaphthalene with $HAuCl_4$ and $Pt(acac)_2$ precursors.

While the above explanation is the most plausible, other explanations exist. It is well known that butyllithium can deprotonate amine to produce the amide anion, which can work as a reducing agent as well as a stabilizing agent. Varying butyllithium amounts varies the ratio of amine to amide anion. More amide anion may stabilize the spherical AuPt NPs. Less amide anion generates a mixture of particles and branched NWs. At a suitable ratio of amine and amide anion, anisotropic growth may be favored to form NWs. The detailed mechanism for the formation of AuPt NWs requires more work on control experiments with pre-synthesized amide.

2.4.2. The Origin of CO Tolerance

For low temperature CO oxidation using Au catalysts, a small particle size of Au NPs (less than 4nm) and reducible oxides such as Fe_xO_y, Ti_xO_y, and Ce_xO_y are generally required.[121-126] Although recent report of Au NPs on alumina obtained significant activity for CO oxidation,[127] most research on alumina supported Au catalyst did not show good performance. In this study it was found that iron carbonyl impurity in steel-CO cylinders enhance CO oxidation. This finding suggests that those work showing low temperature

CO oxidation on *non*-reducible oxide supported Au catalysts needs to be reexamined. In this work, the requirement of iron promoter for heteroaggregates in CO tolerant hydrogen oxidation is quite consistent with other reported results.[125] First of all, heteroaggregates are not low temperature CO oxidation catalysts, which can be explained by the large size of the Au cores. The control experiment of Au and Pt mixture also suggests the CO tolerance was not due to CO oxidation by Au itself. The only reasonable explanation is from the unique heteroaggregate structure. Since the Au cores of heteroaggregates have a large size (11nm), CO preferentially binds to Pt tendrils. Through oxygen activation by Au/Fe_xO_y pairs, CO oxidation occurs in the Au-Pt interface. The hydrogen oxidation is facilitated by continuously cleaning CO from the Pt tendrils. The observation of CO oxidation prior to hydrogen oxidation for heteroaggregate catalysts is consistent with the proposed mechanism.

The alloy catalysts have another type of mechanism, indicated by a different behavior in catalysis. Although the alloy catalysts were also enhanced by Fe promoter, the influence of the Fe promoter is much less than that of the AuPt heteroaggregate catalyst. After conditioning, the water completion temperature of the alloy catalyst is approximately 10^oC higher than that with the steel-CO cylinder. In contrast, with the Fe promoter the heteroaggregate catalyst shows a 50^oC enhancement compared to the water completion temperature without the Fe promoter. The alloy catalyst shows a CO tolerant hydrogen oxidation. The hydrogen oxidation and CO oxidation are initiated together with a low selectivity for CO_2, which indicates that CO does not bind strongly to the surface. A conversion of less than 100% CO in the system without the iron promoter also indicates CO does not bind tightly to alloy surface. This phenomenon may be explained

by strong interaction between Au and Pt atoms in alloy system. The strong interaction causes weak binding between the Pt atom and the CO molecule, and allows activation of oxygen by Au components at a low temperature. XPS studies provide additional evidence for the interaction between Au and Pt. The surface oxidized Au components were found in alloy particles. In contrast, pure Au particles and AuPt heteroaggregates did not exhibit measurable oxidized species in XPS studies. The formation of oxidized Au species in air suggests the Au component can activate oxygen, and facilitate CO oxidation. The proposed mechanisms for CO tolerant hydrogen oxidation are summarized in Scheme 2.2. The mechanism of CO oxidation by Au is still under contest in the literature, and understanding the detailed mechanism needs more work possibly using *in-situ* spectroscopic studies.

Scheme 2.2. Proposed catalytic mechanisms for $H_2/CO/O_2$ over the AuPt heteroaggregate and alloy catalysts.

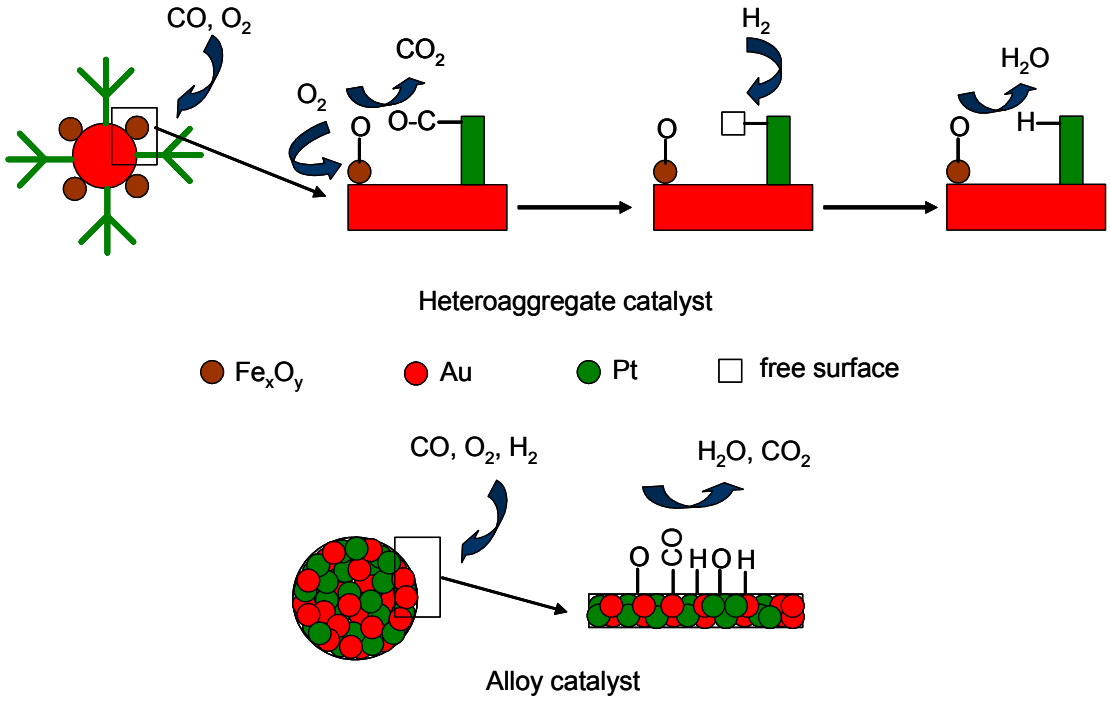

Chapter 3

Syntheses of Pt Group Based Nanoparticles and Their Applications in De-NO_x Reactions with Hydrogen

3.1. Introduction

The adverse effect of NO_x (defined as $NO+NO_2$), the byproduct of high temperature combustion, on environment and personal health is well known. Removal of NO_x from the exhaust of stationary sources (e.g. power plants) and mobile sources (e.g. vehicles) is a government requirement. Three way catalysts (TWCs) have been successfully applied to remove NO_x for several decades with current vehicle engines that operate close to stoichiometric conditions of oxygen and fuel in the temperature range from 400^{o}C to 800^{o}C.[128, 129] Under these conditions, the air/fuel ratio adjusted by electric control is only enough to convert all the hydrocarbons to carbon dioxide and water. The effluent of vehicle engines contains hydrocarbons, which work as a reducing agent to reduce NO_x to dinitrogen. The current TWCs can remove the products of incomplete combustion, carbon monoxide and NO_x, simultaneously.[128-131] The remarkable performance of TWCs has been intensely reviewed in the last 30 years. However TWCs can not function properly with a large excess of air, which is found in power plants , "lean burn" (LB) engines and diesel engines.[128, 129]

The effluent of power plants contains a few hundred parts per million (ppm) of NO_x and several percent of oxygen (i.e. lean burn conditions). Under the high concentration of oxygen, the reductant has to be able to selectively reduce NO_x to dinitrogen. Selective catalytic reduction (SCR) of NO_x under these conditions is very difficult and great effort

has been made to address this issue. Ammonia was found to be an SCR agent for removal of nitrogen oxides, and has been applied in industrial power plants.[132] Other reducing agents containing nitrogen atoms, such as urea or cyanuric acid, are also efficient in SCR of NO_x. The main drawbacks of this method are the cost due to expense of ammonia, its limited distribution networks and environmental problems caused by unreacted ammonia.[128]

The more efficient "lean burn" (LB) engine and diesel engines, which operate in a large excess of air below 400^oC can gain 10% more fuel efficiency compared to the same engine operated on stoichiometric conditions.[128] The main obstacle is to meet the standards for particulate and NO_x emissions simultaneously. A stable SCR catalyst may provide a possible solution for applications of these types of engines. Among the current approaches, the selective catalytic reduction of NO_x with hydrocarbons (HC-SCR) is the most promising, and receives significant attention. The reductants range from methane, ethane, propane/-ene to larger molecules, and show activities for SCR.[133-145] The main advantage of HC-SCR is that the exhaust contains unburned hydrocarbons, which can be used as reducing agents. However the lack of significant activity below 200^oC remains a problem.[146]

Hydrogen may offer another possible solution to removal of NO_x in lean burn conditions.[129, 146-154] H_2 can be generated on-board from fuels, and was found to be active at low temperatures. While this method is promising, there is a dearth of literature due to a low selectivity of hydrogen. Under lean burn conditions, hydrogen is readily consumed by oxygen to form water.[146]

Supported Pt catalysts were found to be the most active for $NO/H_2/O_2$ or NO/H_2 reactions at low temperatures.[150] Among the common supports, silica was found to be inactive for de-NO_x reactions. In contrast γ-alumina is active for SCR with a high selectivity to dinitrogen, but only at high temperatures (above 400^oC).[129]

Burch and co-workers have studied the mechanism of NO/H_2 reaction over 5% metal loading Pt/SiO_2 catalysts by temperature programmable reaction (TPR) and steady state isotope transient kinetic analysis (SSITKA).[147-149] TPR studies show that the conversion of NO reaches a maximum at 100^oC, and then decreases to a minimum at 175 ^oC followed by reaching 100% at 210 ^oC. The yield of N_2 parallels to the conversion of NO, and finally reaches a yield of 80%. At low temperatures N_2O is the main product. It reaches a maximum at 125 ^oC, and then decreases slowly. The ammonia formation is observed during a temperature range of 50 ^oC to 200 ^oC. Mechanistic studies suggest that the N_2O formation is from a surface species containing two nitrogen atoms, and N_2 formation is mainly from the impact of weakly bounded NO or gaseous NO with a surface species containing one nitrogen atom.[148] However, the same catalyst shows poor performance for the $NO/H_2/O_2$ reaction. NO_2 is the main product at lower and higher temperatures, and in the middle range of temperature N_2O is dominant. In contrast to the NO/H_2 reaction, ammonia formation was not observed under lean-burn conditions. This is reasonable because ammonia can not exist in net oxidizing conditions. It is interesting to note that N_2 formation reaches a maximum at 120 ^oC, and then decreases slowly as the temperature increases. Within the reaction temperature range, the highest N_2 yield is close to 25% with a selectivity of 25%. While the mechanism of N_2 and N_2O formations by SSITA is very similar to that of NO/H_2 reaction, NO_2 formation occurs through two

mechanisms. At lower temperatures, the NO_2 forms from a gas phase reaction between gaseous NO and gaseous O_2. At high temperatures, NO_2 forms through reaction between gaseous (or chemisorbed) NO and adsorbed O.

The effect of addition of a promoter has been investigated by modifying Pt/Al_2O_3 with Na_2O and MoO_3.[146] For all tested loadings of Na_2O, no selectivity enhancement was observed. At lower loadings of sodium, the NO conversion increased. As the loading increases, an adverse effect for the NO conversion and the N_2 selectivity was revealed. In contrast, both the NO conversion and N_2 selectivity were enhanced for all the tested loadings of MoO_3. The reason for activity enhancement by sodium is still not clear. It may involve the strengthening of the bond between the Pt atom and NO molecule. The electropositive sodium may cause the bond between the Pt atom and NO molecule (an electron acceptor adsorbate) to become stronger, leading to weakening N-O bond.[155] This interaction further enhances the dissociation of the N-O bonds. In contrast to an indirect effect of sodium, the effect of MoO_3 is significant. MoO_3 may have a direct effect on the N_2 formation in addition to any small change of electronic properties of Pt. The MoO_3 promoter greatly increases the concentration of intermediate leading to N_2 formation. The possible intermediates are reduced nitrogen species, such as ammonia or NH_x type species. Indeed, molybdenum compounds containing nitrogen atoms such as ammonium molybdate are well-known.

Costa and co-workers have investigated support effects on catalytic behavior with $La_{0.5}Ce_xSr_{0.5-x}MnO_3$ and $La_{0.7}Sr_xCe_{0.3-x}FeO_3$.[150, 151] The Pt loading is 0.1% (wt %), which is in contrast to most reported studies with 1 to 5% Pt loading. The Pt/ $La_{0.5}Ce_{0.5}MnO_3$ catalyst exhibits a maximal NO conversion of 75% with a N_2 selectivity of 75%. The

operating temperature window (activity >20%) ranges from 100°C to 160°C. The Pt/ $La_{0.7}Sr_{0.2}Ce_{0.1}FeO_3$ system shows a wider operating temperature window ranging from 100 °C to 250°C with a maximal NO conversion of 83%. The N_2 selectivity ranges from 77% to 93%. The authors also studied these two catalysts for NO/H_2 reactions. They show high N_2 selectivity in NO/H_2 stream even with a ratio of 1 to 4 (NO to H_2). The most surprising property of these systems was that no ammonia and NO_2 were found either in lean-burn conditions or NO/H_2 system, which is in contrast to all other reports in the literature. The supports are suggested to have direct and indirect influence on catalytic behavior in these systems. In particular, the supports are thought to provide a means for adsorption of NO with the nitrogen atom on Pt metals and O atoms on oxygen vacancies of supports, leading to a higher rate of dinitrogen formation compared to the NO on the Pt surface alone.

All the conventional Pt catalysts investigated in de-NO_x reactions exploited a wet impregnation method, i.e, impregnating precursor solutions with supports followed by calcination and reduction to form metallic active components. This method is convenient, and sometimes achieves good performance. However the effect of particle size of the active components by this method can't be fully understood due to difficulties with imaging the active components on supports and difficulties with tuning the particle size. In some cases the metal-support interaction caused by reduction or calcination complicates the interpretation. For multi-component catalysts, this problem becomes even more serious due to the lack of knowledge regarding the phase of the catalytic components.

The present work exploits nanoparticles (NPs) as active components to study de-NO_x reactions with hydrogen and/or oxygen. The typical preparation procedures include impregnating alumina with the pre-synthesized metallic nanoparticle colloid from suspensions, vacuum drying to remove solvent at low temperatures followed by thoroughly washing with acetone and water to remove the excess stabilizing agent. The particle size of active components is adjusted by changing the amounts or type of stabilizing agent. In this work, monometallic Pd and Pt NPs, bimetallic PdCu, PtCu, and PdPt NPs were synthesized and studied for de-NOx reactions. The structures of bimetallic NPs are fully characterized by XRD, UV-visible, XPS, FT-IR, and TEM (with EDS). The structures include alloy structures (PdCu and PtCu), and core-shell structures (Cu@Pt, Pt@Cu, Pd@Pt, and Pt@Pd). Among these bimetallic NPs, the Cu@Pt NPs exhibit an abnormal stability upon high temperature annealing. We attribute this phenomenon to Kirkendall mass transport effect. In contrast the Pt@Cu core-shell NPs are readily transformed into a more thermodynamically stable alloy structure upon annealing. As prepared PdCu NPs also exhibit a kinetically stable solid solution structure with copper rich surface, which is in contrast to the phase diagram. Annealing this material affords an ordered phase and further high temperature annealing transforms the ordered phase back into the solid solution phase, which is consistent with the phase diagram. Under NO/H_2 reaction (rich conditions), bimetallic alloy PdCu and PtCu NPs have higher selectivity for N_2 at the expense of activity drop. However, for bimetallic Cu@Pt, Pd@Pt core-shell structures they maintain high activity of pure Pt NPs and have higher selectivity for N_2 than that of the Pt NPs. At 4/1 H_2/NO ratio, the maximum of the selectivity for N_2 of the Pd@Pt NPs is 62%, which is two times more than that of pure Pt

NPs at the same reaction conditions. In addition, the Pt@Pd NPs exhibit the activity enhancement as well as the selectivity enhancement compared to pure Pd NPs, which are attributed to the near surface alloy effect. While most bimetallic structures show an enhanced N_2 selectivity in NO/H_2 reaction, the monometallic NPs have the better performance than the bimetallic structures under lean-burn conditions. In particular, the small Pt NPs (1-2 nm) show the highest activity for the $NO/H_2/O_2$ reaction. Generally the Pt/Al_2O_3 catalysts prepared by metallic nanoparticle colloid method in this work have a wider operating temperature window. Compared with $Pt/La_{0.5}Ce_xSr_{0.5-x}MnO_3$ and $Pt/La_{0.7}Sr_xCe_{0.3-x}FeO_3$ catalysts, the Pt/alumina catalyst exhibits NO conversion above 50% in the range of 100 ^oC to 400 ^oC with a selectivity range from 50% to 75%.

3.2. Experimental Section

3.2.1. Materials

Palladium(II) acetate ($Pd(OAc)_2$, 99.9+%), copper(II) acetate ($Cu(OAc)_2$, 98%), platinum(II) acetylacetonate ($Pt(acac)_2$, 97%), potassium tetrochloroplatinate(II) (K_2PtCl_4, 99.99%), PAMAM-OH dendrimer (Generation 4, 10wt% solution in methanol), Poly(vinylpyrrolidone) (PVP, Average Mw ca. 55,000 or 29,000), copper(II) acetylacetonate ($Cu(acac)_2$,97%), oleylamine ($C_{18}H_{37}N$, tech., 70%), oleic acid ($C_{18}H_{34}O_2$, 99% (GC), cell culture tested), decahydronaphthalene ($C_{10}H_{18}$, anhydrous, 99+%, mixture of cis and trans), and 2-ethoxyethanol (99+%, spectrophotometric grade) were purchased from Sigma-Aldrich. Cupric sulfate ($CuSO_4.5H_2O$, 99.06%) was purchased from Mallinckrodt. Ethylene glycol (boiling range 196-199^oC) was purchased from Fisherchemicals. Palladium chloride ($PdCl_2$, 60wt% of Pd) and platinous chloride

($PtCl_2$, 73.07wt% of Pt) were purchased from Engelhard. γ-alumina (S. A. 80-120 m^2/g, 3 micron APS powder) was purchased from Alfa Aesar. All the chemicals were used without any further purification. H_2, O_2, Ar, and NO cylinders with ultra high purity were purchased from Airgas, and used without further purification.

3.2.2. Syntheses of Monometallic, Bimetallic NPs, and γ-alumina Supported Catalysts

3.2.2.1. Synthesis of of PdCu NPs

The synthesis of PdCu NPs is a modified version of Bradley *et al*.[156]

1.75 mmol $Pd(OAc)_2$ and $Cu(OAc)_2$ with 54.4 mg PVP_{55000} were co-dissolved in 20 ml 2-ethoxyethanol in a round-bottom flask with stirring. The resulted solution was then refluxed for 2 hours to generate a black colloid. This colloid contains PdCu particles with an average size of 3.4 nm. It was then cooled down to room temperature, washed with acetone and precipitated via centrifugation. The resulting powders were isolated by decanting the top solution. The acetone washing/centrifugation procedure was repeated five times. The powders were then dried at 60 ^oC overnight for XRD analysis and annealing experiments. The same procedure was used for all particles unless stated.

2-ethoxyethanol can be substituted ethylene glycol as solvent in the synthesis of PdCu NPs.

3.2.2.2. Synthesis of Pd_xCu_y NPs

$PdCu_2$ was synthesized as discussed above. 0.25 mmol $Pd(OAc)_2$, 0.50 mmol $Cu(OAc)_2$ and 31 mg PVP_{55000} were co-dissolved in 5.8 ml 2-ethoxyethanol. The resulting solution was then refluxed for 2 hours to form a black colloid. For synthesis of

Pd_3Cu, the starting materials contained 0.45 mmol $Pd(OAc)_2$, 0.15 mmol $Cu(OAc)_2$, 13.6 mg PVP_{55000}, and 5 ml 2-ethoxyethanol. Other procedures are same to those of $PdCu_2$.

3.2.2.3. Synthesis of Pd NPs

0.51 mmol $Pd(OAc)_2$ and 15.5 mg PVP_{55000} were co-dissolved in 5.8 ml 2-ethoxyethanol. The resulting solution was then refluxed for 2 hours to form a black colloid, which contained Pd particles with an average size of 11.5 nm.

3.2.2.4. Synthesis of PtCu NPs

The following method is a modified version of Toshima *et al*.[157]

A 25 ml three-neck round-bottom flask was charged with 0.11 mmol $Pt(acac)_2$, 0.11 mmol $CuSO_4.5H_2O$, 3 mg PVP_{55000}, and 5 ml glycol. It was then slowly heated with strong stirring to dissolve the chemicals. The solution was further refluxed for 2 hours to form a black colloid, which contained PtCu particles with an average size of 3.3 nm.

$Cu(acac)_2$ and $Cu(OAc)_2$ were also exploited to investigated the effect of reduction potentials of the precursors on formation of alloy structure. The procedures are same as above except charging the flask with 0.46 mmol $Pt(acac)_2$, 0.46 mmol $Cu(acac)_2$, 14 mg PVP_{55000}, and 7.5 ml glycol. For the synthesis using $Cu(OAc)_2$, 0.46 mmol $Pt(acac)_2$, 0.46 mmol $Cu(OAc)_2$, 9.3 mg PVP_{55000}, and 5 ml glycol were charged into the reaction flask.

3.2.2.5. Synthesis of Pt NPs

0.11 mmol $Pt(acac)_2$ and 3 mg PVP_{55000} were co-dissolved in 5ml glycol. The resulting solution was then refluxed for 2 hours to form a black colloid, which contains Pt particles with an average size of 15.3nm.

3.2.2.6. Syntheses of Cu@Pt and Pt@Cu NPs

0.156 mmol $Cu(acac)_2$, 116 mg PVP_{55000}, and 32 ml glycol were charged into a 100 ml round-bottom flask. It was then slowly heated with strong stirring to dissolve chemicals. The resulted blue solution was further refluxed for 20 minutes to form a reddish Cu colloid with an average particle size of 4 nm. The mixture was then cooled down to room temperature, and charged with 0.156 mmol $Pt(acac)_2$. The reaction mixture was then slowly heated and refluxed for 1 hour to give a black colloid. This colloid contained Cu@Pt particles with an average particle size of 8.8 nm.

For the synthesis of Pt@Cu, 0.315 mmol $Pt(acac)_2$, 18.8 mg PVP_{55000}, and 7.7 ml glycol were charged into a 25 ml round-bottom flask with strong stirring. The reaction mixture was then slowly heated to dissolve precursors. The mixture was then refluxed for 2 hours to give a black colloid. The colloid was then cooled down to room temperature and charged with 0.315 mmol $CuSO_4.5H_2O$. The mixture was then slowly heated to dissolve $CuSO_4.5H_2O$, and then refluxed for 2 hours to give a black colloid, which contained Pt@Cu particles with an average size of 18.3 nm.

3.2.2.7. Synthesis of Mixture of Pt and Cu NPs

The mixture of Pt and Cu colloid was obtained by mixing the Cu colloid with an average particle size of 4 nm formed in the synthesis of Cu@Pt and the Pt colloid with an average particle size of 15.3 nm.

3.2.2.8. Syntheses of Pt NPs Stabilized by Oleylamine and Pt_{40} NPs Stabilized by Dendrimer

0.157 mmol $Pt(acac)_2$ and 4.4 ml oleylamine were co-dissolved in 26.4 ml decahydronaphathelene in 50 ml three-neck round-bottom flask. The reaction mixture was slowly heated with strong stirring to dissolve the precursors. The resulting solution was then refluxed for 2 hour at boiling to form a black colloid. This colloid contained Pt particles with an average particle size of 4.5 nm.

Pt_{40} NPs stabilized by dendrimers was synthesized by the reported method of Crooks etal.[32] 0.00258 mmol G4-OH denderimer 10% (wt%) methanol solution was dried at room temperature under vacuum in 100 ml three neck round-bottom flask. 0.103 mmol K_2PtCl_4 was dissolved in 51 ml H_2O, and then added to the flask containing G4-OH with strong stirring. The resulting solution was stirred under N_2 for 0.5 hours. 5ml of aqueous solution containing 0.515 mmol $NaBH_4$ was then added to the reaction mixture. The reaction mixture was then stirred under N_2 for 3 hours to give a black Pt colloid. HCl aqueous solution (0.1M) was then added to the colloid to neutralize the excess $NaBH_4$. This colloid contained Pt_{40} particles with an average particle size of 1.3 nm.

3.2.2.9. Syntheses of Pd@Pt and Pt@Pd NPs

The following method is a modified version of Toshima *et al*.[158]

0.352 mmol $PdCl_2$ and 62.5 mg PVP_{55000} were co-dissolved in 25 ml ethylene glycol in 50 ml three-neck round-bottom flask. The reaction mixture was slowly heated with strong stirring. The temperature of the mixture was then increased to 180^{o}C and kept for 2 hours resulting in the formation of a black colloid. The colloid was then cooled down to room

temperature, and charged with 0.352 mmol $PtCl_2$ and 31 mg PVP_{55000}. The mixture was then slowly heated to 180°C, and kept at this temperature for 2 hours. The resulting colloid contained Pd@Pt particles with an average particle size of 8.0 nm.

For the synthesis of Pt@Pd, 0.282 mmol $PtCl_2$ and 62.5 mg PVP_{55000} were co-dissolved in 20 ml ethylene glycol in 50 ml three-neck round-bottom flask. The reaction mixture was slowly heated to 180°C with strong stirring, and heated for 2 hours at this temperature to give a black colloid. The colloid was then cooled down to room temperature, and charged with 0.282 mmol $PtCl_2$ and 31 mg PVP_{55000}. The mixture was then slowly heated to 180°C, and kept at this temperature for 2 hours. The resulting colloid contained Pt@Pd particles with an average particle size of 8.2 nm.

3.2.2.10. Preparation of γ-alumina Supported Catalysts

Supported catalysts were prepared by mixing a required amount metal colloid with γ-alumina to generate slurry and subsequently removing solvent at around 80°C in vacuum. The resulting gray powder was further washed with acetone and ethanol at least five times to remove the organic residues and then dried at 60°C overnight. For monometallic catalysts, the metal loading of all the catalysts is 1.0 % (weight percent). For bimetallic catalysts, the loading of heavy metal is 1.0 % (weight percent), and the mole ratio of the light metal to the heavy metal is 1 to 1.

3.2.3. Characterization of Samples

3.2.3.1. UV-Visible Absorption Spectroscopy

For UV-Visible absorption spectroscopy, metal colloids were first diluted in ethylene glycol, and then measured using ethylene glycol as background on HP 8452A diode array

spectrometer with a deuterium lamp having a resolution of 2nm. The concentrations of metal colloids were adjusted to have a comparable maximum absorption.

3.2.3.2. Transmission Electron Microscopy (TEM)

All low magnification images were taken using a Zeiss EM 10CA transmission electron microscopy with an accelerating voltage of 80 kV. 4 μl diluted metal colloids were deposited onto CFC-300Cu grids (purchased form Electron Microscopy Sciences), and dried in air. FE-STEM images for Cu@Pt and Pt@Cu NPs were taken by Kevin MaIlwrath at Hitachi High Technologies America on HD-2300 200kv dedicated FE-STEM with EDX detector with a high sensitivity. Other HRTEM images were recored on JEOL 300 kV TEM.

3.2.3.3. Powder X-ray Diffraction (XRD)

Powder XRD was operated on Bruker C2 Discover X-ray Powder Diffractometer with a Hi-Star area dedector and CuK_{α} radiation. Analyses of XRD patterns were performed using the JADE® software package with the JC-PDF database and auto indexing. Diffraction patterns were measured in the 2Θ range from 5 to 90°. XRD samples were prepared by pressuring powder onto a glass plate. Prior to the measurement, the samples were thoroughly washed by ethanol to remove excess organic chemicals.

3.2.2.4. X-ray Photoelectron Spectroscopy (XPS)

XPS measurements were conducted on a Kratos Axis 165 spectrometer by Dr. Bindhu Varughese using Mg K_{α} radiation in a vacuum of 4×10^{-10} Torr. The hybrid mode was applied for measurements of 10 scans with a step size of 0.1 eV and a sweep time of 60s. The spectra were recorded in the FAT analyzer mode with a pass energy of 80 eV. The

data processing was performed using graphical analysis software. The spectra were fit with 60% Gaussian/ 40% Lorentzian peaks after linear background subtraction. The minimum number of peaks were used to deconvolute the spectral envelops.

3.2.3.5. Infrared Spectroscopy (IR)

The measurement of IR-CO probe spectrum was carried out on Thermo Nicolet Nexus 670 FT-TR. The metal colloid of interest was bubbled with CO stream with stirring for 30 minutes. The mixture was then charged into an IR cell with a CaF_2 window with a 0.15mm thickness of liquid layer. The IR spectra were measured in a range from 1800 to 2800cm^{-1} by subtracting the spectrum of the same metal colloid without CO.

The reliability of the method was tested by changing the CO purge with N_2 purge. The spectrum of metal colloid bubbled with N_2 or without any treatment was a straight line, indicating that this method is reliable.

3.2.4. Evaluation of Catalysts for NO/H_2 and $NO/H_2/O_2$ Reactions

The catalytic behavior of supported NPs for NO/H_2 and $NO/H_2/O_2$ reactions were measured by placing the supported catalysts in a packed bed arrangement in a 6.4mm internal diameter (ID) quartz tube centered in a vertical programmable tube furnace. The catalyst charge was 5.5mm in height. The packed bed consisted of 105mg of catalyst (including support) intermixed with 135mg of 1-μm quartz particles to provide adequate flow through the bed. For monometallic catalysts, the metal loading is 1.0% (wt %). For bimetallic catalysts, the heavy metal loading is 1.0%, and the ratio of heavy metal to light metal is 1/1 (atomic ratio). The catalyst bed was held in place by quartz wool above and beneath, which assisted in preheating the gases to the prescribed furnace temperature.

The reactor is shown in Figure 2.1. Computer-controlled electronic mass-flow controllers were used to vary flow rates and to fix reactor residence times and the reactant gas velocity (0.1597 m/s). The reactant mixture contained 0.75-3% H_2, 0.75% NO, 0-5% O_2, with an Ar balance. Product gases were measured continuously with a carefully calibrated mass spectrometer (VG Prima δB). Product compositions were determined from the calibrated sensitivities and ion-cracking patterns for the analyzed gases. The catalytic data were obtained after stabilized performance was achieved for all the catalysts.

3.3. Results

3.3.1. PdCu Alloys

PdCu alloy NPs can be prepared from aqueous solution or non-aqueous solution method.[156, 157, 159] Bradley and coworkers have synthesized PdCu bimetallic NPs from reductions of $Pd(OAc)_2$ and $Cu(OAc)_2$ in 2-ethoxyethanol with PVP_{40000}.[156] The 2-ethoxyethanol functions as a reaction solvent, as well as a reducing agent. Reductions of oxidized noble metal precursors by alcohol or polyol have been well known for several decades.[38, 40-43, 46] Products from these reactions are metallic noble metal NPs, aldehydes and carboxylic acids. However, the detailed mechanism is still not clear. It may involve an oxidative addition of an O-H bond followed by a β-hydrogen elimination or other solvent degradation pathways. PVP was used as a stabilizing agent in these reactions. It coordinates to the surface atoms of the NPs by its functional groups to give stabilizing NPs, which terminates particle growth.

The mechanism of formation of PdCu NPs suggested by the authors[156] is that 2-ethoxyethanol first reduces $Pd(OAc)_2$ to metallic Pd, which further reduces $Cu(OAc)_2$ to Cu. This redox cycle continues to form PdCu bimetallic NPs. While the bimetallic structure was proven by the single particle EDS and IR-CO probe spectroscopy, the real structure (alloy, core-shell, or heterodimeter) was not assigned. In this work, we slightly modified their recipes, and exploited XRD to obtain phase information of these bimetallic NPs. By significantly decreasing the concentration of PVP and increasing the volume of solvent, the PdCu colloid is more suitable for preparation of supported catalysts. Figure 3.1a shows the XRD pattern of as-prepared PdCu alloy particles synthesized in 2-ethoxyethanol. The absence of diffractions from individual Pd or Cu NPs is consistent with the alloy structure. However, the peak positions slightly shift to Cu side, indicating the formation of a gradient alloy. UV-visible measurements did not show any SPR signals of Cu NPs, indicating the absence of Cu NPs larger than 4nm.

In bulk studies of CuPd system, at 1/1 ratio of Pd/Cu (atomic ratio) while the β-ordered alloy phase is more thermodynamically stable in the reaction temperature range (below 200^{o}C), the α solid solution disordered phase (atoms statistically distributed system) can only be prepared by high temperature annealing (above 500^{o}C).[160] Interestingly, XRD pattern (Figure 3.1a) of the "as prepared" CuPd NPs (reaction temperature below 200^{o}C) exhibit a similar pattern to that of the α solid solution disordered phase, which disobeys the phase diagram.

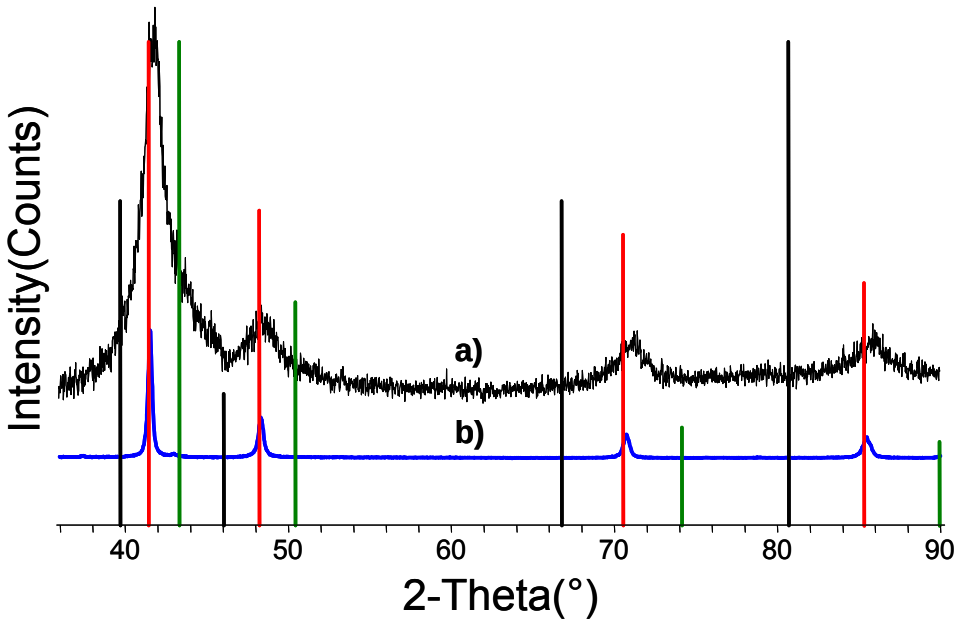

Figure 3.1. XRD patterns of PdCu NPs showing a) as prepared PdCu particles, b) PdCu particles annealed at 550°C for 2 hours. The vertical lines show the peak positions of Pd (black, JCPDS 01-1310), PdCu alloy (red, JCPDS 48-1551), and Cu (green, JCPDS 04-0836).

While XRD pattern of as prepared CuPd NPs is close to that of the α solid solution phase, a small shift to Cu side was observed. The small shift to Cu side suggests that the particle surfaces are Cu-rich, and the NPs are compositionally gradient particles. Annealing as prepared sample at 550°C for 2 hours give a well-defined XRD pattern of 1:1 PdCu α alloy phase(Figure 3.1b), which gives further evidence for a gradient alloy structure in the as prepared sample. The peak positions of this alloy are between those of Pd and Cu and consistent with Vegard's law, indicating the formation of statistically disordered solid solution alloy phase (the α phase).

Switching solvents from 2-ethoxyethanol to glycol resulted in a similar PdCu gradient alloy structure. The XRD pattern of the sample with a reaction time of two hours is shown in Figure 3.2a. However, XRD pattern of the sample with a reaction time of three

hours shows three additional peaks, indicating the formation of a new phase-the β-ordered alloy phase (Figure 3.2b).

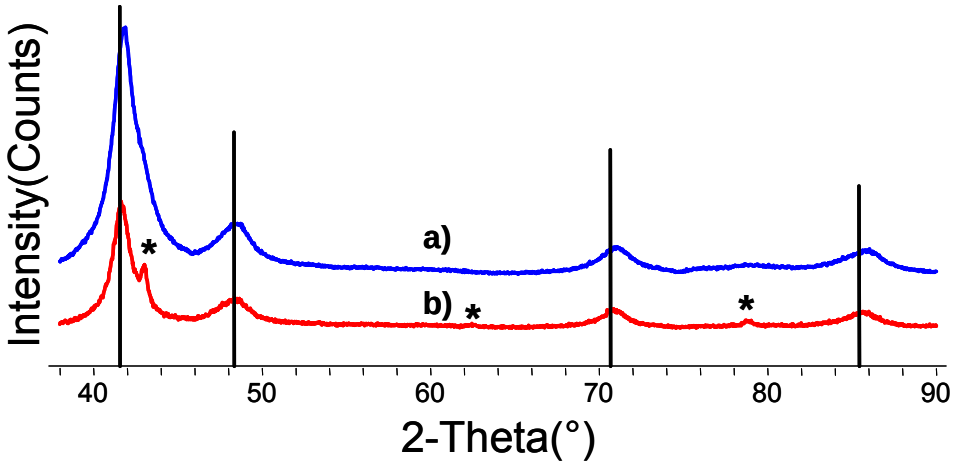

Figure 3.2. XRD patterns of PdCu particles prepared by glycol with different reaction time showing a) 2 hour, b) 3 hours. The vertical lines show the peak positions of PdCu alloy (JCPDS 48-1551), and stars indicate three new peaks.

To further prove the formation of β phase, annealing experiments of as-prepared gradient PdCu alloy NPs were carried out in vacuum to study their thermodynamic structures. Figure 3.3b shows the XRD pattern of the sample annealed at 300^{o}C for two hours. As illustrated in figure 3.2a, the as-prepared sample is a gradient alloy. However, annealing this sample at 480^{o}C resulted in six new peaks (Figure 3.3c), and the peak positions of the main peaks match those additional peaks of the as prepared sample with a reaction time of three hours (Figure 3.3a).

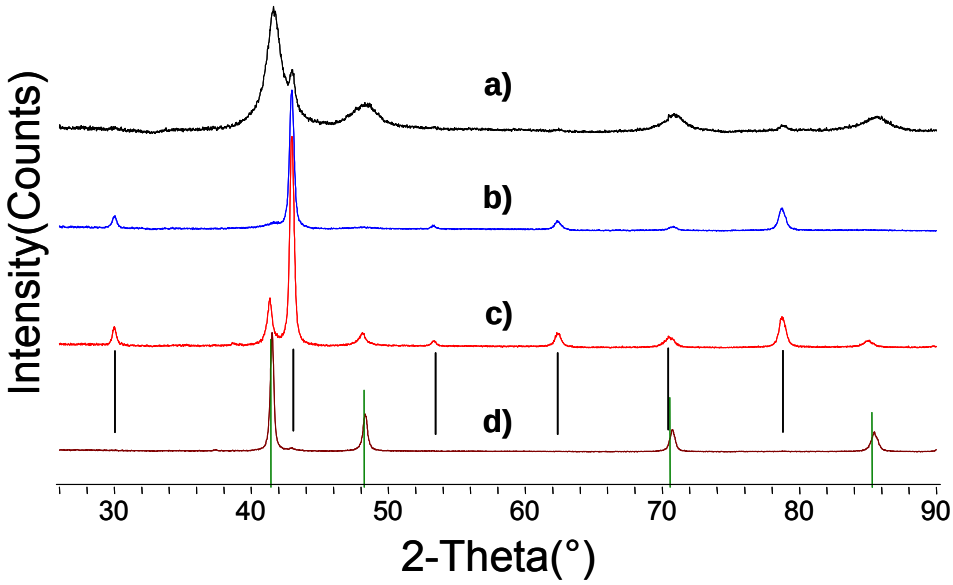

Figure 3.3. XRD patterns of the annealed PdCu particles synthesized in glycol with a reaction time of 2 hours showing a) as-prepared sample with a reaction time of 3 hours, b) the sample annealed at 300°C for 2 hours (nearly pure β-ordered phase), c) the sample annealed at 480°C for 2 hours (the mixture of α and β phases), and d) the sample annealed at 550°C for 2 hours (pure α phase). The vertical green lines show the peak positions of α alloy of PdCu (JCPDS 48-1551), and the vertical black lines indicate the peaks position of β alloy of PdCu.

Further annealing at 550°C gives a nearly pure α alloy. While the phase transformation phenomena are consistent with the phase diagram, the dominant phase of the as-prepared sample is metastable α solid solution phase, which is in contrast to bulk materials. Upon annealing, this α alloy phase transforms to the β-ordered phase, and then transforms back to the α alloy phase.

Indexing those peaks of β phase against JCPDS data shows a fcc structure (face centered cubic structure) with a lattice parameter of 2.98Å, which is consistent with the data reported in the literature.[161] The index results are shown in Table 3.1.

Table 3.1. The indexed β-ordered CuPd XRD data of the sample (with a reaction time of 2 hours in glycol) annealed at 300^{o}C for 2 hours.

Cell=2.980×2.980×2.980<90.0×90.0×90.0>.

d(Å)	h	k	l	2-Theta (^{o})
2.980	1	0	0	30.0
2.107	1	1	0	42.9
1.720	1	1	1	53.2
1.490	2	0	0	62.3
1.333	2	1	0	70.6
1.217	2	1	1	78.6

Figure 3.4 shows the low magnification TEM images of PdCu alloy and pure Pd NPs. the PdCu NPs are nearly monodispersed with an average particle size of 3.4 nm (Figure 3.5a). It is also proven by the XRD pattern (Figure 3.1a), which shows a line broadening phenomenon, indicating a poor crystallinity with small particles. Annealing these particles gives a sharp XRD pattern (Figure 3.1b) due to crystallinity increase with particle size increase. Annealing in solution also cause atoms reconstruction to form alloy particles with smaller composition gradients. As shown in Figure 3.2b the XRD pattern of the particles prepared by the glycol method have smaller shifts compared to that of the particles by the 2-ethoxyethanol method (glycol: b.p. 197 ^{o}C; 2-ehoxyethanol: b.p. 135^{o}C). Figure 3.4b shows the low magnification TEM image of pure Pd NPs. These particles are polydispersed with an average particle size of 11.5 nm. While the roughly

spherical shape is dominant, other shapes including triangle, square and hexagonal cannot be neglected.

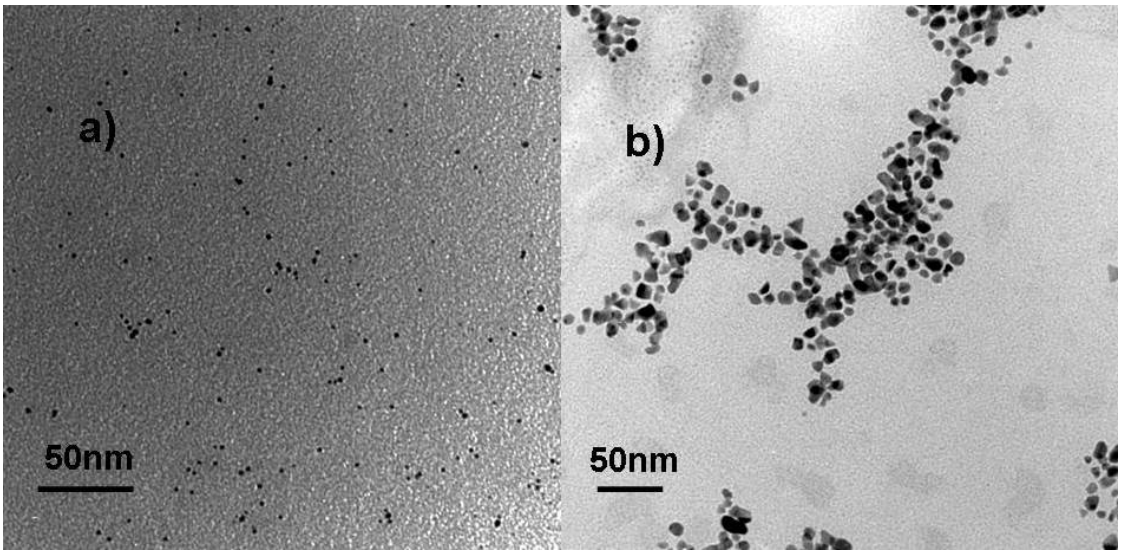

Figure 3.4. Low magnification TEM images showing a) PdCu alloy NPs prepared by 2-ethoxyethanol, and b) pure Pd NPs.

A control experiment showed that $Cu(OAc)_2$ cannot be reduced by 2-ethoxyethanol in the absence of $Pd(OAc)_2$. This observation is consistent with the mechanism proposed by the authors, and is also consistent with the formation of a gradient alloy with a copper rich surface. XRD patterns of PdCu with different compositions show that the diffraction patterns change with the composition changes. More Cu in PdCu will shift the peaks to higher 2Θ (Figure 3.6). Table 3.2 lists comparison of compositions calculated from Vegar's law and nominal compositions from starting materials. All the alloys display a high angle shift from predicted values, indicating a Cu rich surface compared to the nominal composition (Table 3.2), which further prove the proposed mechanism. In figure 3.4, it was found that the average particle size of PdCu alloy NPs is significant smaller than that of pure Pd NPs. In the syntheses of PdCu alloy and Pd NPs, the PVP/Pd ratio

and the concentration of $Pd(OAc)_2$ are same, and the only difference is that $Cu(OAc)_2$ is present is in the synthesis of PdCu alloy NPs. The small size of PdCu alloy NPs suggests that co-reduction of Pd and Cu precursors produces more seeds, which further produce small PdCu alloy NPs.

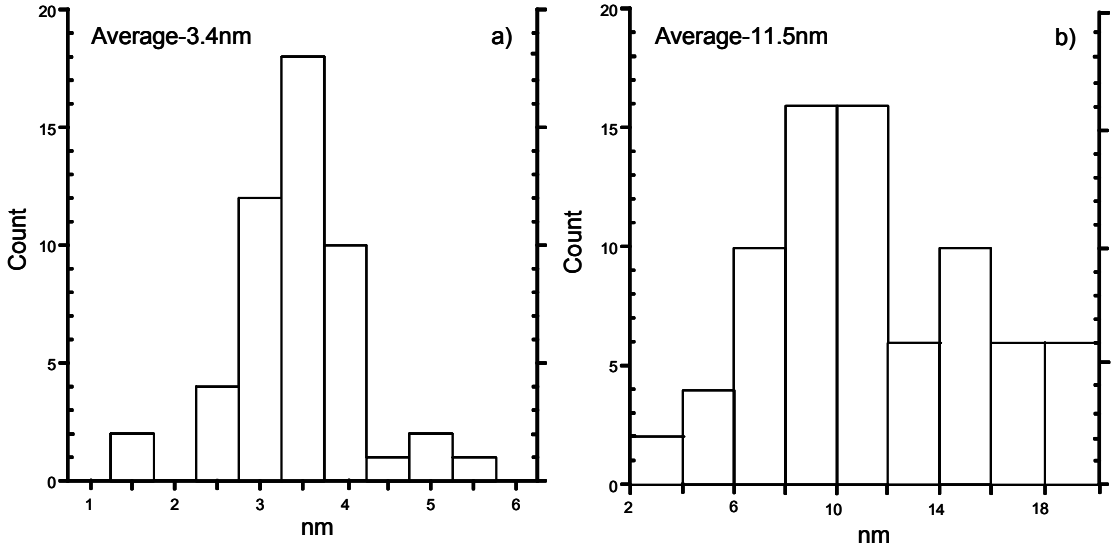

Figure 3.5. Histograms of particle distributions of PdCu and Pd NPs showing a) PdCu alloy NPs, and b) Pd NPs.

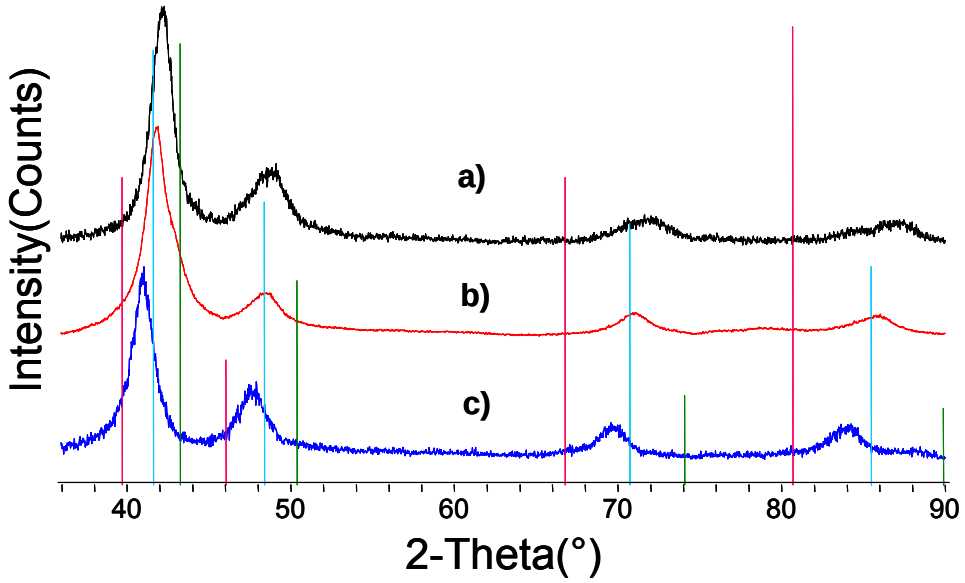

Figure 3.6. XRD patterns of Cu-Pd alloys with different compositions showing a) $PdCu_2$, b) PdCu, and c) Pd_3Cu. The vertical lines show the peak positions of Pd (red, JCPDS 01-1310), PdCu alloy (blue, JCPDS 48-1551), and Cu (green, JCPDS 04-0836).

Table 3.2. Comparisons of nominal compositions and compositions by Vegard's Law through XRD patterns of different PdCu alloys.

Materials	composition (% Cu)	Calculated composition (%Cu) by Vegard's law
$PdCu_2$	66.7	69.7
PdCu	50.0	58.1
Pd_3Cu	25.0	35.3

3.3.2. PtCu Alloys

Toshima and coworkers have synthesized PtCu NPs in aqueous solution.[157] In their method, NaOH was exploited to transform $H_2PtCl_6.6H_2O$ and $CuSO_4.5H_2O$ precursors to a PVP_{40000} stabilized hydroxide colloid. Refluxing the hydroxide colloid in ethylene glycol resulted in a black PtCu colloid. The alloy structure was proven by XRD and UV-

visible spectroscopy which showed no SPR absorption of Cu. While alloy NPs without compositional gradients were prepared by this method, the disadvantages of using Na cations in this system and large amounts of PVP made this system not suitable for preparation of supported catalysts. Here, we designed a new method to synthesize PtCu alloy particles.[162] In our method, $Pt(acac)_2$ and $CuSO_4.5H_2O$ were co-reduced by ethylene glycol with PVP_{55000} as a stabilizing agent. All byproducts are easily removeded by acetone washing and no transformations to hydroxide colloids are required. The resulting gradient alloys can be transformed into alloy structures without compositional gradient upon annealing. Figure 3.7a shows the XRD patterns of PtCu alloys. As illustrated in the synthesis of PdCu, the shifts to Cu side in the XRD pattern of as prepared PtCu was also observed. Upon annealing, an atomic reconstruction generated alloy structures without compositional gradients (Figure 3.7b). The proposed mechanism is similar to that of PdCu. First, $Pt(acac)_2$ is reduced to metallic Pt by glycol, and then Pt further reduces $CuSO_4.5H_2O$ to Cu, leading to a gradient alloy with Cu rich surface. The proposed mechnism is consistent with the control experiment of $CuSO_4.5H_2O$ in glycol giving no metallic Cu in the absence of $Pt(acac)_2$.

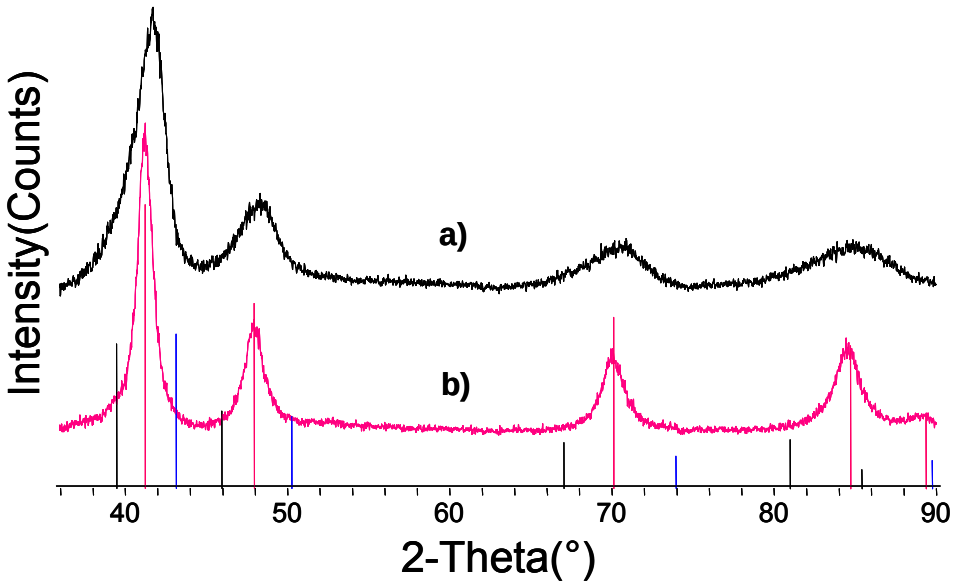

Figure 3.7. XRD patterns of PtCu alloy NPs showing a) as prepared PtCu NPs, and b) the samples annealed at 300°C for 2 hours. Vertical lines indicate the peak positions of Pt (black, JCPDS 04-0802), PtCu alloy (red, JCPDS 48-1549), and Cu (blue, JCPDS 04-0836).

Figure 3.8 shows XRD patterns of samples prepared by using different Cu precursors. It is clearly shown that reduction potentials of precursors play an important role in the formation of alloys. When $Cu(acac)_2$ is used as the precursor, the alloy cannot be formed. XRD patterns show that there are individual Pt and Cu particles (Figure 3.8b). Switching $Cu(acac)_2$ to $Cu(OAc)_2$ generates a mixture of monometallic and bimetallic NPs (Figure 3.8c).

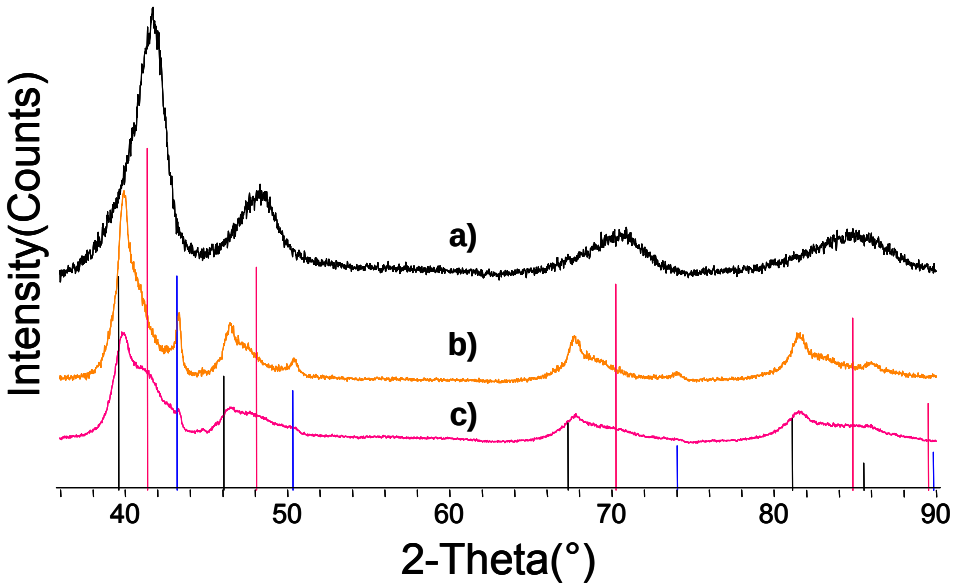

Figure 3.8. XRD patterns of samples prepared by using different Cu precursors showing a) sample with $CuSO_4.5H_2O$, b) sample with $Cu(acac)_2$, and c) sample with $Cu(OAc)_2$. Vertical lines indicate the peak positions of Pt (black, JCPDS 04-0802), PtCu alloy (red, JCPDS 48-1549), and Cu (blue, JCPDS 04-0836).

Figure 3.9 shows TEM images of PtCu alloy and pure Pt NPs. The PtCu alloy NPs are spherical, and nearly monodispersed with an average particle size of 3.6 nm (Figure 3.9a and Figure 3.10a). Pure Pt NPs prepared by this method show a hexagonal shape with an average particle size of 15.3 nm (Figure 3.9b and Figure 3.10b). As observed in the syntheses of PdCu and Pd, the monometallic Pt NPs have a significant large particle size compared to bimetallic PtCu alloy NPs. The reason of formation of small PtCu alloy NPs is same as that of PdCu alloy NPs. Co-reduction of Pt and Cu precursors produces more seeds, leading to formation of small PtCu alloy NPs.

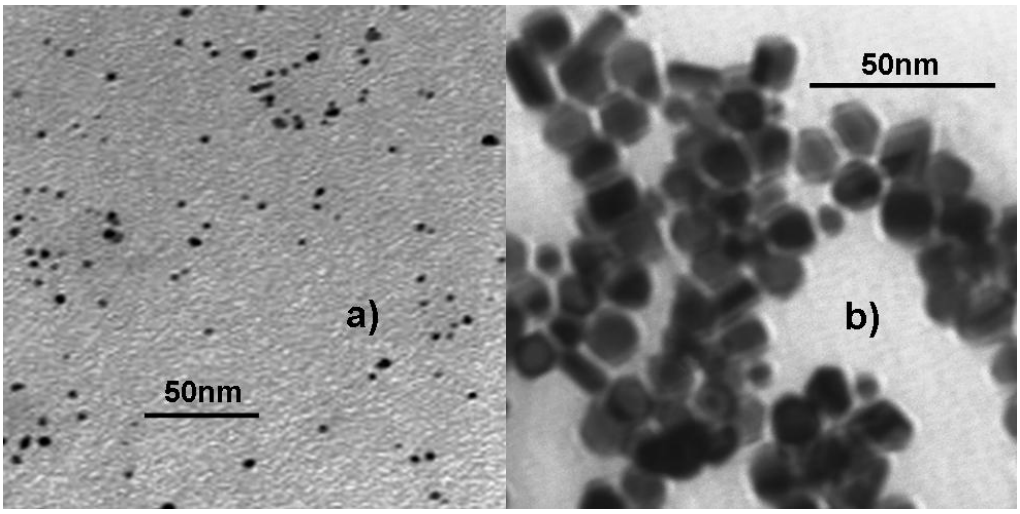

Figure 3.9. TEM images of Pt-Cu alloy and Pt NPs showing a) PtCu alloy NPs, and b) Pt NPs.

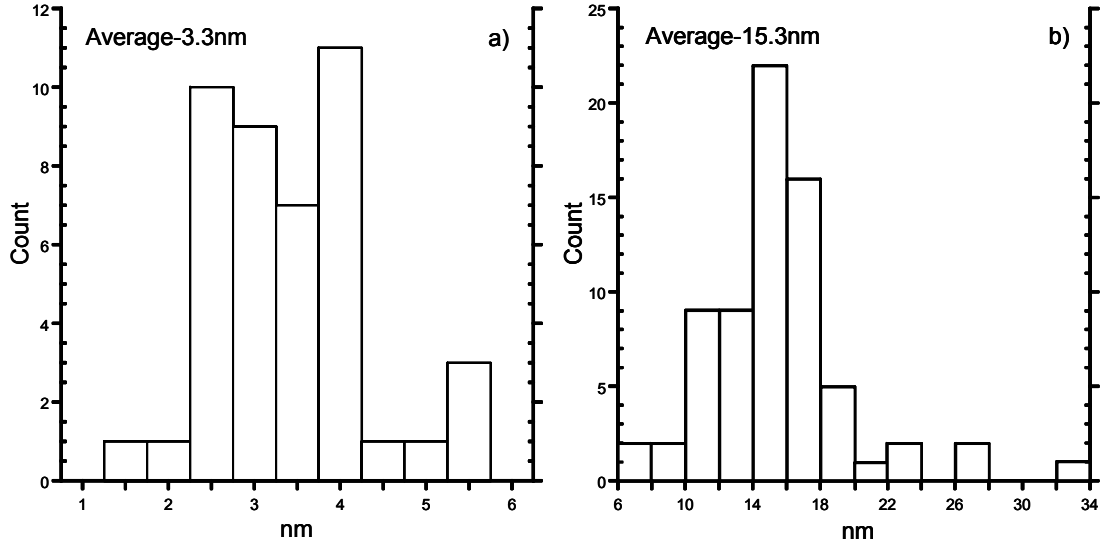

Figure 3.10. Histograms of particle distributions of PtCu and Pt NPs showing a) PtCu alloy NPs, and b) Pt NPs.

3.3.3. Oleylamine Protected Pt NPs and Dendrimer Protected Pt NPs

Hiroki and Osterloh have synthesized Au and Ag NPs by using oleylamine as a reducing agent.[30] We applied the same method for the synthesis of Pt particles. Refluxing $Pt(acac)_2$ in decahydronaphthalene with oleylamine results in Pt NPs with an average particle size of 4.5 nm (Figure 3.11). The oleylamine works as a reducing agent as well as

a stabilizing agent. It is known that the functional group of amine can be oxidized by metal ions to nitriles. In other words, the metal ions are reduced by the amine to the metallic state. The double bond in oleylamine seems not to be important in the redox reaction because saturated amines work equally well. The XRD patterns of particles clearly show the formation of metallic Pt NPs. Low magnification TEM image shows that the Pt particles have branched, rod-like shapes (Figure 3.11), suggesting an important role of stabilizing agent on shape control (hexagonal shape with PVP).

Pt_{40} NPs protected by dendrimers were synthesized by the reported method of Crooks *et al*.[32] TEM images show that Pt_{40} NPs are nearly monodispersed and spherical in shape with an average particle size of 1.3 nm, which is same as reported in the literature.

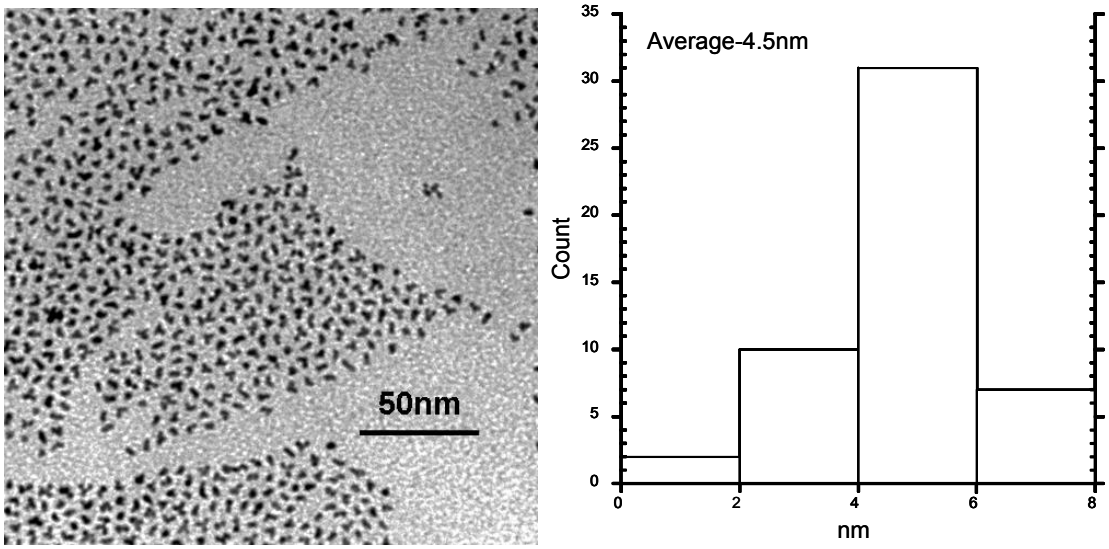

Figure 3.11. Low magnification TEM image of 4.5 nm Pt and its particle size distribution.

3.3.4. Cu@Pt and Pt@Cu Core-shell Structures

Cu@Pt NPs were prepared by a sequential reduction method.[162] $Cu(acac)_2$ was first reduced in refluxing ethylene glycol. The resulted reddish Cu colloid was further charged

with $Pt(acac)_2$ and then refluxed resulting in a black colloid. Figure 3.12a shows the TEM images of the Cu@Pt NPs. A hexagonal shape was observed for the particles. The shape of the Cu@Pt NPs is similar to that of the pure Pt NPs and is different from the spherical PtCu alloy NPs, consistent with the different structures of the two particles. The Pt@Cu NPs were prepared by depositing Cu on Pt nanoparticles.[162] As illustrated in the synthesis of the PtCu alloy NPs, metallic Pt can catalyze the reduction of $CuSO_4.5H_2O$ to metallic Cu. A sequential reduction procedure was exploited to make Pt@Cu core-shell NPs. Figure 3.12b shows the TEM image of Pt@Cu NPs. In contrast to the spherical PtCu alloy NPs, Pt@Cu has a hexagonal shape with an average particle size of 18.3 nm (Figure 3.13b). Compared to the metallic Pt seeds (Figure 3.10b) the increase of particle size suggests that the Cu deposits on the Pt NPs.

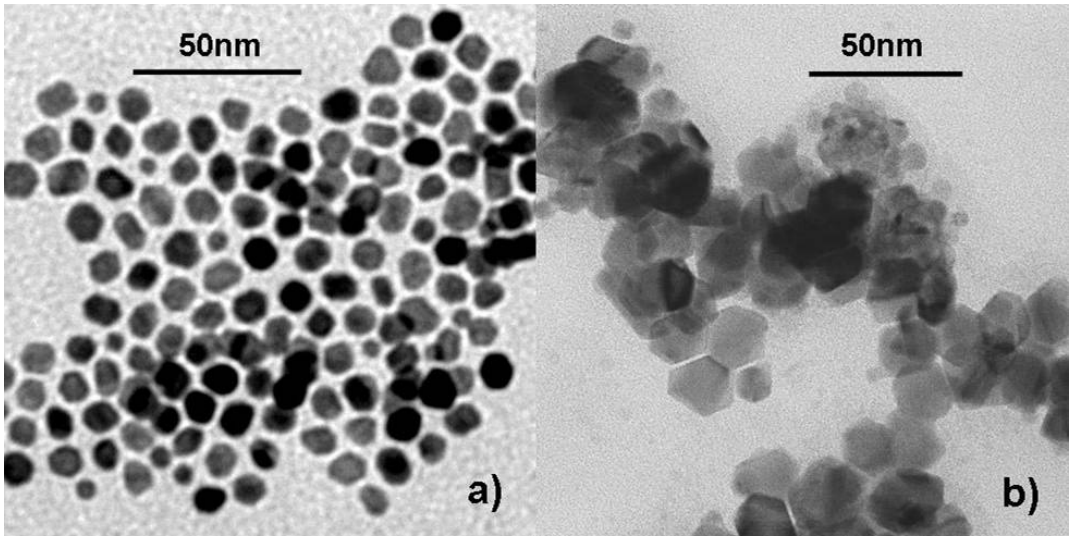

Figure 3.12. Low magnification TEM images showing a) Cu@Pt, and b) Pt@Cu core-shell particles.

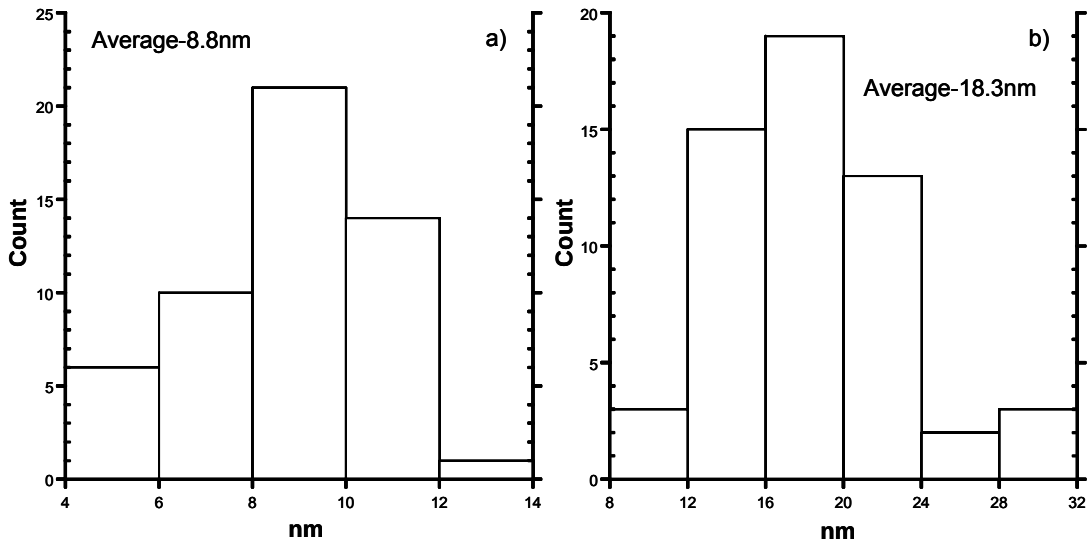

Figure 3.13. Histograms of particle distributions showing a) Cu@Pt, and b) Pt@Cu.

UV-Visible spectroscopy was used to test for the presence of an ~560 nm SPR band due to Cu NPs. The measurements for the Cu@Pt and Pt@Cu NP colloid did not show any signals of Cu SPR absorption, suggesting the absence of Cu NPs larger than 4 nm (only the Cu particles larger than 4 nm have SPR absorption).

To exclude out the presence of monometallic NPs, FE-STEM with EDS was employed to obtain detailed compositional information. Figure 3.14a and 3.14b show the FE-STEM images of Cu@Pt and Pt@Cu NPs. Figure 3.14c and 3.14d show the Cu phase maps of these particles. Figure 3.14e and 3.14f show the Pt phase maps of these NPs, respectively. It is clearly illustrated that every Cu@Pt and Pt@Cu particle contain Pt and Cu components and the presence of monometallic particles can be excluded out.

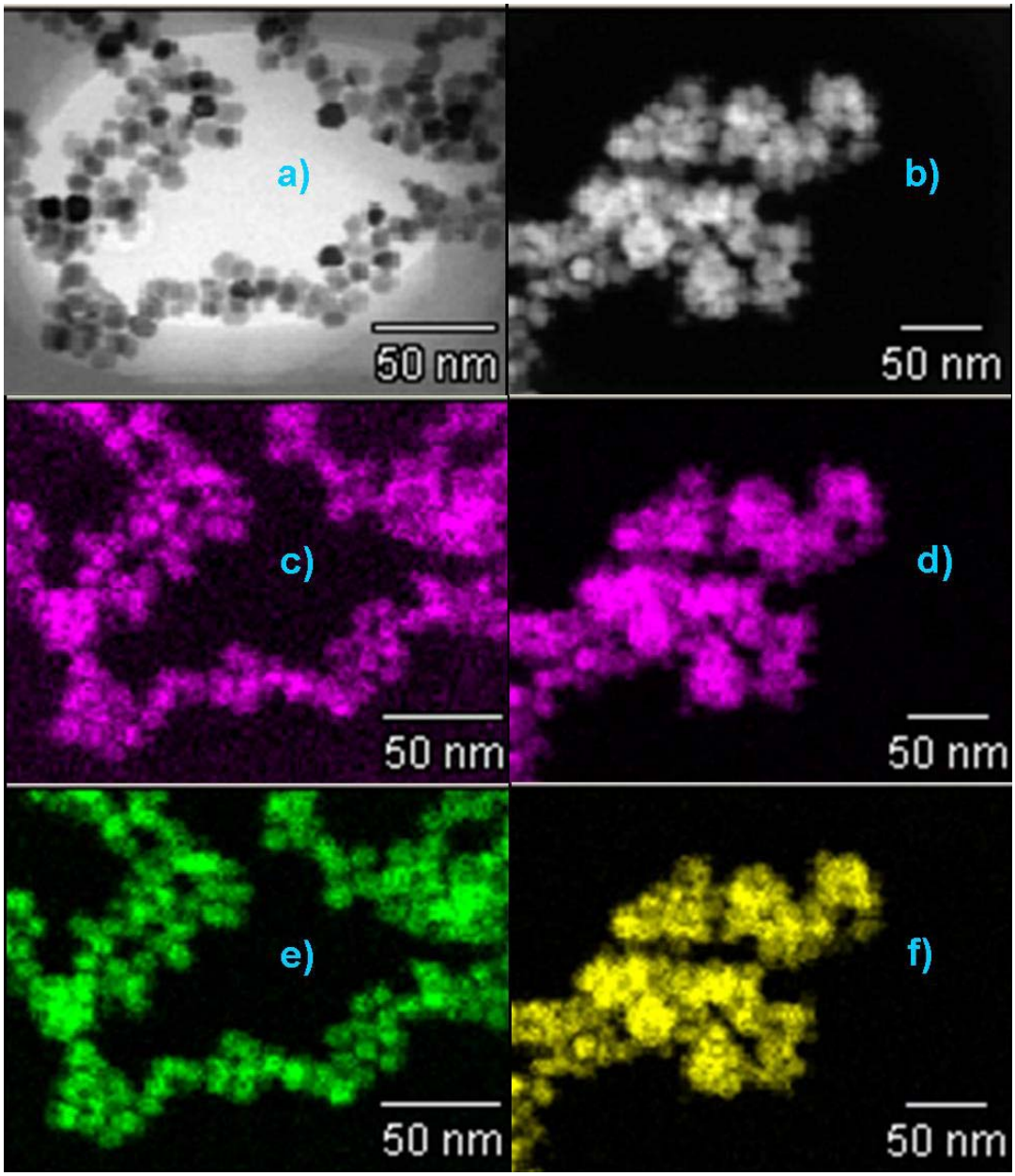

Figure 3.14. Images of FE-STEM with EDS showing a) the FE-STEM image of Cu@Pt, b) the FE-STEM image of Pt@Cu, c) the Cu phase map of Cu@Pt, d) the Cu phase map of Pt@Cu, e) the Pt phase map of Cu@Pt, and e) the Pt phase map of Pt@Cu.

Figure 3.15 shows the XRD patterns of Cu@Pt and Pt@Cu NPs. It is clearly shown that the Cu@Pt NPs contain pure Pt and Cu components (Figure 3.15e). While the core-shell structures and physical mixtures are all consistent with the XRD pattern, when this XRD data is combined with FE-STEM with EDS, the XRD pattern indicates a core-shell

structure. In contrast, "as prepared" Pt@Cu NPs show a pure Pt core and Cu rich alloy shell phase (Figure 3.15d). According to Vegard's Law, this Cu rich phase has an approximate composition of $Cu_{0.8}Pt_{0.2}$. These XRD data are consistent with a physical mixture or a core-shell structure of these phases. However the FE-STEM with EDS excludes the presence of monometallic NPs. The only intersecting result is the core-shell structure.

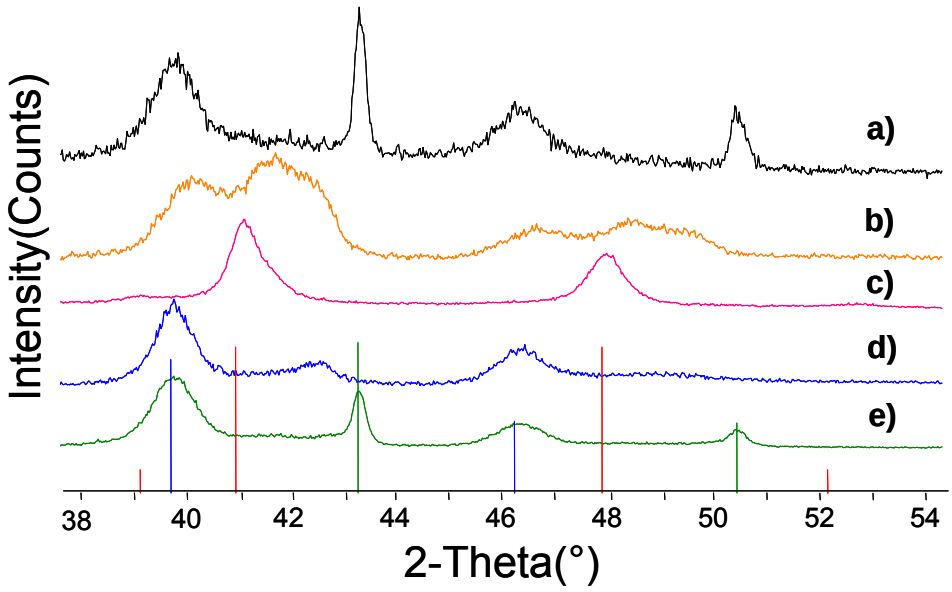

Figure 3.15. XRD patterns of CuPt showing a) the physical mixture of Cu and Pt NPs annealed at 370°C for 5 hours, b) Cu@Pt annealed at 370°C for 5 hours, c) Pt@Cu annealed at 370°C for 5 hours, d) as-prepared Pt@Cu, and e) as-prepared Cu@Pt. Vertical lines indicate the peak positions of Pt (blue, JCPDS 04-0802), PtCu alloy (red, JCPDS 29-0547, another alloy phase of PtCu), and Cu (green, JCPDS 04-0836).

The annealing behavior of Cu@Pt, Pt@Cu and physical mixtures of Cu and Pt NPs with the roughly same size are quite different. Figure 3.15a shows the XRD pattern of the physical mixture annealed at 370°C in vacuum. It is clearly shown that no alloy formation occurs under these conditions. However, Pt@Cu core-shell structures are readily transformed into alloy structures upon annealing (Figure 3.15c). In contrast, Cu@Pt

structures partially alloy, leading to a nearly pure Pt shell and a Cu rich core phase (Figure 3.15b). HRTEM images of the annealed Cu@Pt and Pt@Cu also support these observations. As illustrated in Figure 3.11, the as-prepared Cu@Pt and Pt@Cu have hexagonal structures. Upon annealing, the Cu@Pt NPs still maintain the hexagonal shape, indicating no significant structure change on the surface (Figure 3.16a). In contrast, the Pt@Cu NPs change their shape from hexagonal to spherical, suggesting the formation of spherical alloy NPs.

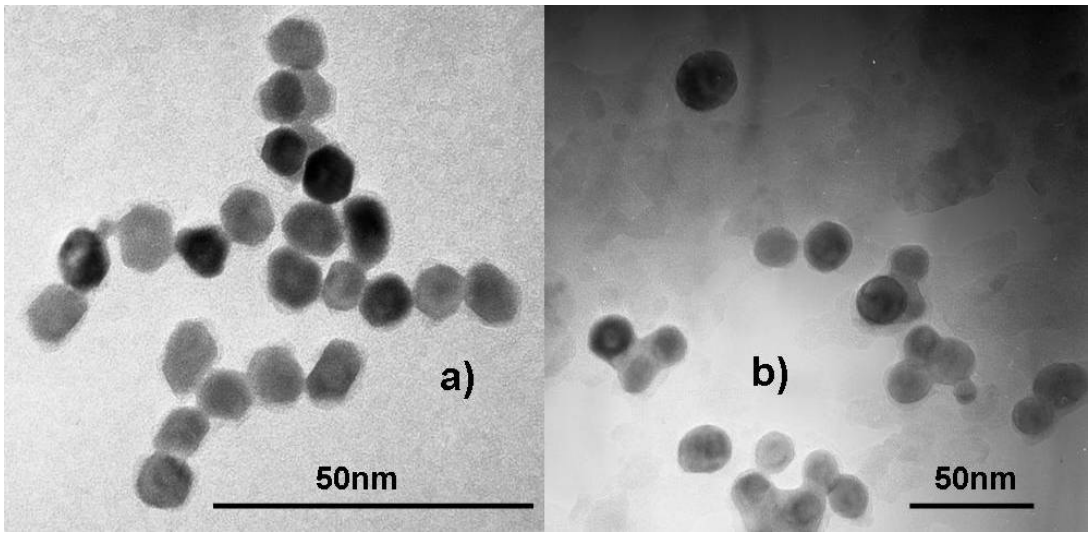

Figure 3.16. HRTEM images of annealed Cu@Pt and Pt@Cu NPs showing a) Cu@Pt annealed at 370^{o}C for 5 hours, and b) Pt@Cu annealed at 370^{o}C for 5 hours.

Based on the XRD, FE-STEM with EDS, and annealing experiments, it is suggested that Cu@Pt has a core-shell structure with a pure Pt and pure Cu phase. Pt@Cu has a core-shell structure with a pure Pt and $Cu_{0.8}Pt_{0.2}$ alloy phase. While the relative positions of these two phases in core-shell structures are suggested by the sequential reduction method, the definitive evidence come from XPS investigations. Table 3.3 lists the atomic compositions of Cu@Pt and Pt@Cu NPs obtained by XPS. Each metal contains metallic

and oxidized states. Considering processing samples for XPS in non air-free conditions, the presence of oxides is not surprising.

Table 3.3. Compositions of Pt@Cu and Cu@Pt by XPS before etching.

Materials	metallic Pt	oxidized Pt	metallic Cu	oxidized Cu	total Pt	total Cu
Pt@Cu	26.7%	9.6%	33.5%	30.2%	36.3%	63.7%
Cu@Pt	68.2%	19.2%	12.6%	0%	87.4%	12.6%

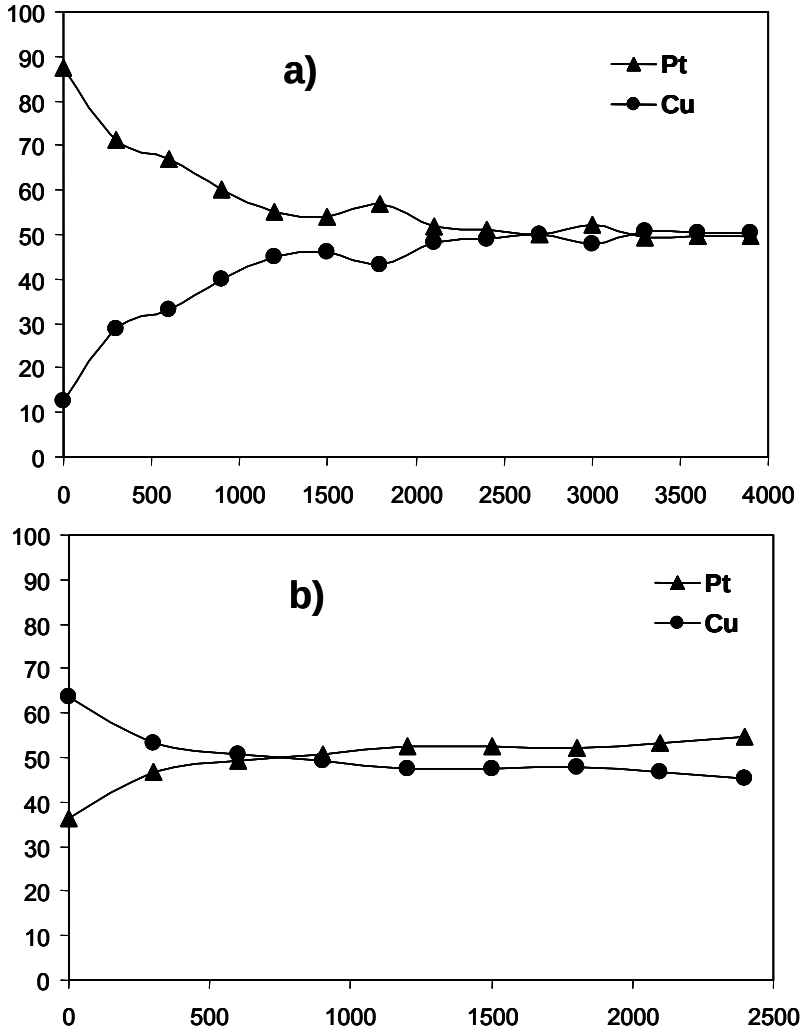

Figure 3.17. The compositions of Pt and Cu in Cu@Pt and Pt@Cu by XPS with sequential etching showing a) Cu@Pt, and b) Pt@Cu.

Figure 3.17 show the relative atomic compositional change of Cu@Pt and Pt@Cu NPs with Ar plasma etching. Before etching, the Cu@Pt NPs show a composition of 87.4% Pt and 12.6% Cu, indicating a high Pt concentration on surface (Table 3.3). As the etching proceeds, the Pt concentration decreases and Cu concentration increases. After 2700 seconds of etching, the ratio of Pt to Cu reaches 1 to 1, which is the stoichiometry of the products. The same phenomenon was observed with Pt@Cu NPs. The smaller compositional difference between Pt and Cu is consistent with the $Cu_{0.8}Pt_{0.2}$ shell phase.

Based on XRD, FE-STEM, XPS, and annealing experiments, it is concluded that Cu@Pt has a core-shell structure with a pure Cu core and Pt shell, and Pt@Cu has a core-shell structure with a pure Pt core and $Cu_{0.8}Pt_{0.2}$ alloy shell.

3.3.5. Pd@Pt and Pt@Pd core-shell NPs

Wang and co-workers have synthesized Pd@Pt and Pt@Pd core-shell NPs by way of the polyol method.[158] The core-shell structures were proven by IR-CO probe measurements. Although Pd@Pt and Pt@Pd were prepared with well-controlled core-shell structures, the procedures were relatively complicated. In their syntheses, the Pd and Pt precursors were first dissolved in dioxane, and mixed with ethylene glycol. The solution was then converted to a hydroxide colloid with sodium hydroxide. The hydroxide colloid was then refluxed in glycol to give either a Pd or Pt core colloid. The core colloids were treated with hydrogen for 2 hours in a mixture of water, ethanol, and ethylene glycol (1:1:1), and then reacted with an aqueous solution of the shell metal precursors. The resulting core-shell particle colloids were very dilute with a large excess of PVP (typically 60 mg NPs in 300 ml solution with 833 mg PVP). To make a colloid suitable for the preparation of supported catalysts, we simplify the preparation procedure

and made concentrated colloids with less PVP. The procedure is as follows: $PdCl_2$ or $PtCl_2$ was dissolved in glycol and reacted at 180°C; it was then cooled down and charged with the $PtCl_2$ or $PdCl_2$, and reacted at 180°C to form the core-shell NPs (typically 60 mg NPs in 15 ml solution with 56 mg PVP).

Figure 3.18 shows TEM images of Pd and Pd@Pt NPs. Pd NPs prepared by this simple method exhibited a narrow particle distribution with an average particle size of 6.2 nm. Figure 3.19 illustrates the particle distribution of these particles. It was clearly demonstrated that the Pd@Pt particle size increased from 6.2 nm (monometallic Pd) to 8.0 nm, indicating Pt deposition on Pd NPs.

In contrast to Pd NPs, monometallic Pt exhibited multi-shape particles. While a roughly spherical shape is dominant, some rod-like NPs were observed (Figure 3.20). In addition, the particle distribution was broader than that of the Pd NPs. The average particle size of the Pt NPs is 6.5 nm. As expected, the Pt@Pd particles show a particle size increase (8.2 nm), suggesting Pd deposition on Pt NPs.

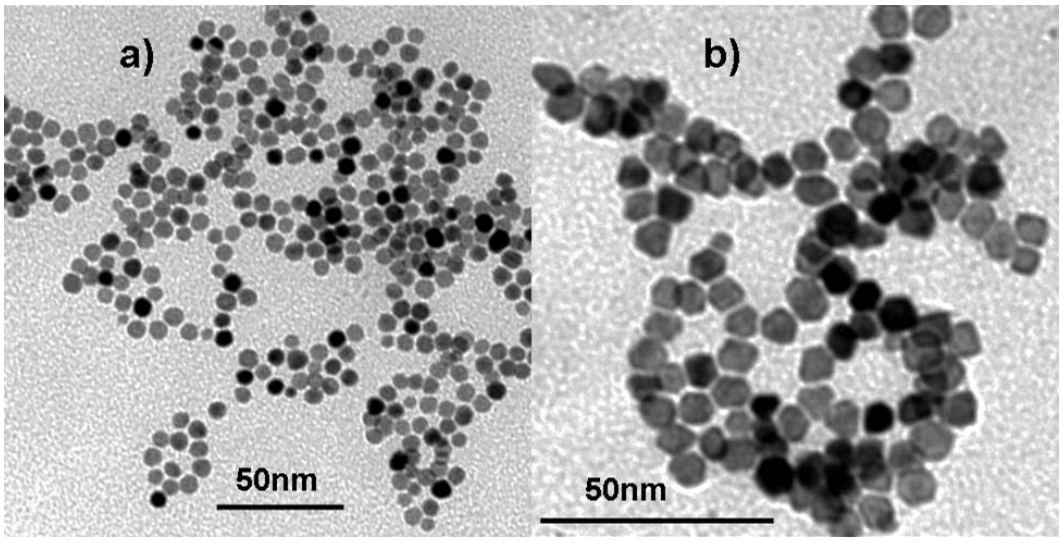

Figure 3.18. Low magnification TEM images of a) Pd and b) Pd@Pt NPs.

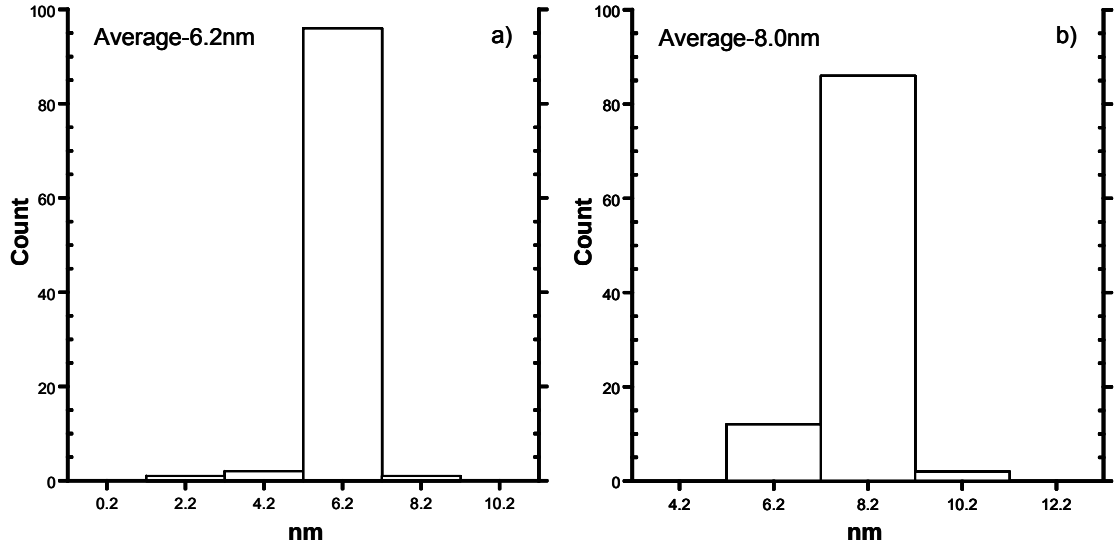

Figure 3.19. Histograms of Pd and Pd@Pt NPs showing particle distributions of a) Pd NPs, and b)Pd@Pt NPs.

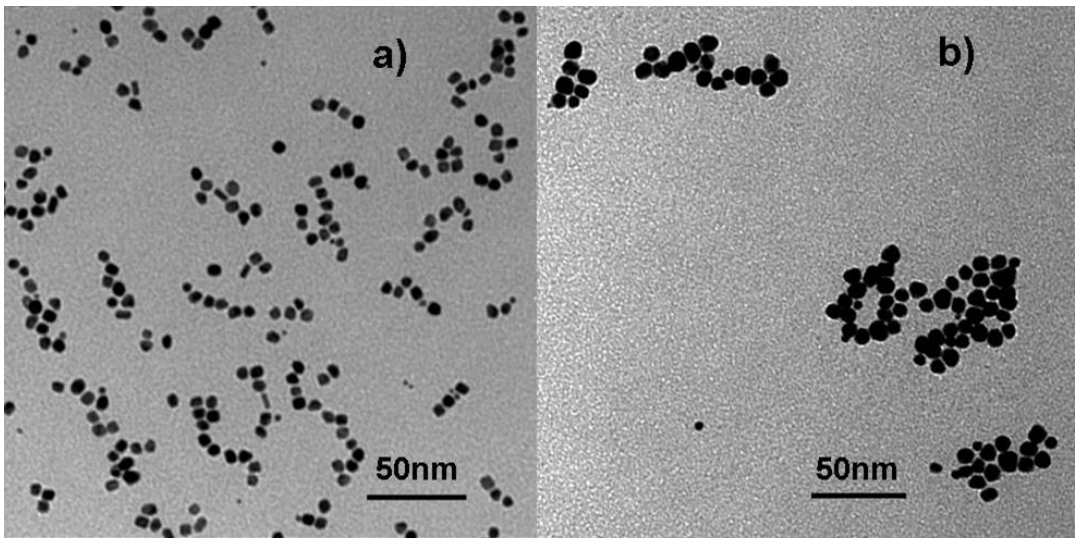

Figure 3.20. Low magnification TEM images showing a) Pt NPs, and Pt@Pd NPs.

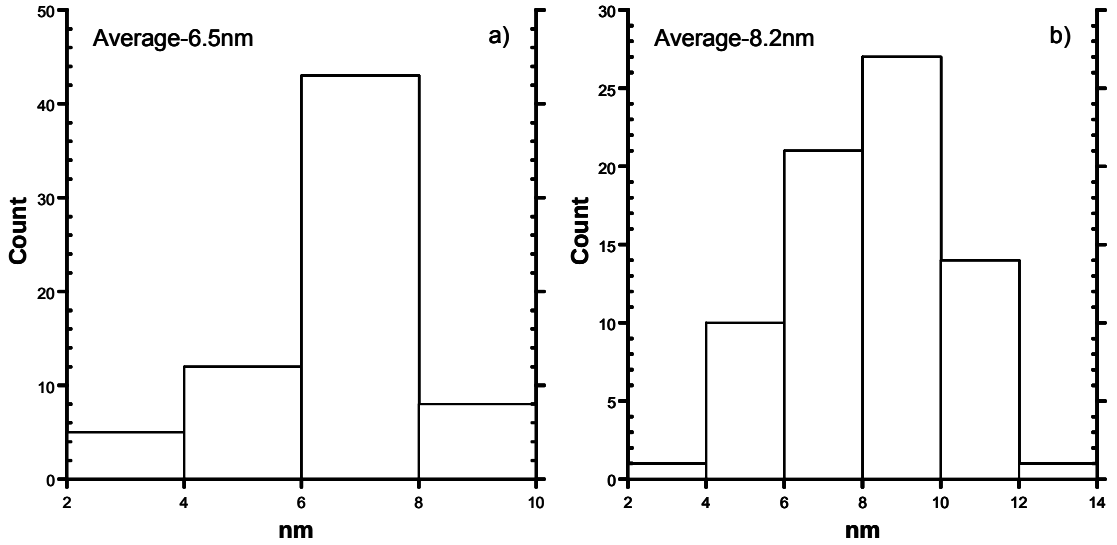

Figure 3.21. Histograms of Pt and Pt@Pd showing particle distributions of a) Pt, and b) Pt@Pd.

Because of the similarity of structure and unit cell of Pd and Pt, we were unable to get phase information by XRD due to overlapping of peak positions. HRTEM with EDS and IR-CO probe measurements were used to investigate the structures of these NPs.

The EDS spectra in HRTEM measurement demonstrated that every particles tested contained components of Pd and Pt. Figure 3.22a shows the EDS spectra of Pd@Pt NPs in HRTEM. The ratio of Pd to Pt of a collection of several particles is 50.5 to 49.5 (Table 3.4), and is very close to the nominal ratio. Figure 3.22b shows the EDS spectra of Pt@Pd. The ratio of Pd to Pt is 44 to 56, and is also in good agreement with the nominal ratio considering the accuracy of EDS for small particles. As shown in Figure 3.22b, the chloride was found in the Pt@Pd sample, which is expected due to using the chloride precursors.

Figure 3.23 shows the FT-IR spectra of CO probe of PdPt colloids. For IR-CO probe measurements of Pd colloids, a strong band at 1957cm^{-1} and a weak band at 1937cm^{-1} were clearly observed (Figure 3.23d). These two bands were assigned to μ_2 and μ_3

bridged CO adsorption sites, respectively.[158] Carefully examining the particles shows that Pd NPs have polyhedral shapes. The coordination number of Pd atoms changes at different surfaces or edges, leading to different CO adsorption bands. The spectra of the Pt colloid (Figure 3.23b) show a strong band at 2066cm^{-1} and a weak band at 1895cm^{-1}. While the 2066cm^{-1} band, assignable to linear CO adsorption on Pt surface, is consistent with Wang's work, the weak band due to μ_2 bridged CO group, shows a 35cm^{-1} blue shift.[158] The reason for this shift is not clear at this time. It may involve a solvent effect. The detailed explanation of this phenomenon needs a systematic investigation of particle size, shape, and solvent effects. Figure 3.23a shows the spectra of the mixture of Pd and Pt NPs. It was clearly shown that the strong bands of Pd and Pt are in agreement with the monometallic colloids. For the spectra of core-shell structures, the Pd@Pt NPs show all of the diagnostic absorptions of the monometallic Pt (Figure 3.23c), indicating of the Pt shell surface. In addition, no observable Pd absorption was found, suggesting the absence of individual Pd NPs. The same phenomenon was observed in Pt@Pd colloid (Figure 3.23e). The spectra of Pt@Pd are similar with monometallic Pd, and no observable Pt absorption was found. As illustrated in the EDS studies, the Pd@Pt and Pt@Pd are bimetallic NPs. Based on the studies of FT-IR, EDS, and particle size analysis, it is concluded that Pd@Pt has a core-shell structure with a Pd core and a Pt shell, and Pt@Pd has a core-shell structure with a Pt core and a Pd shell. Due to the absence of XRD data, the degree of alloying at the interfaces of these two particles is unknown at present.

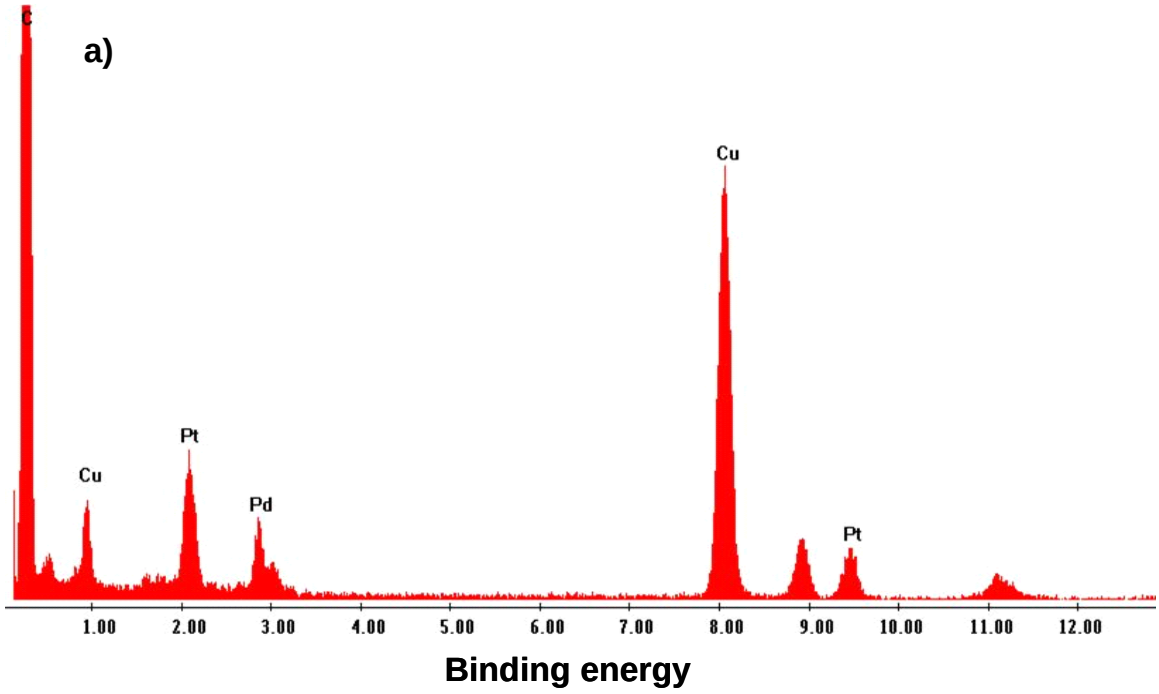

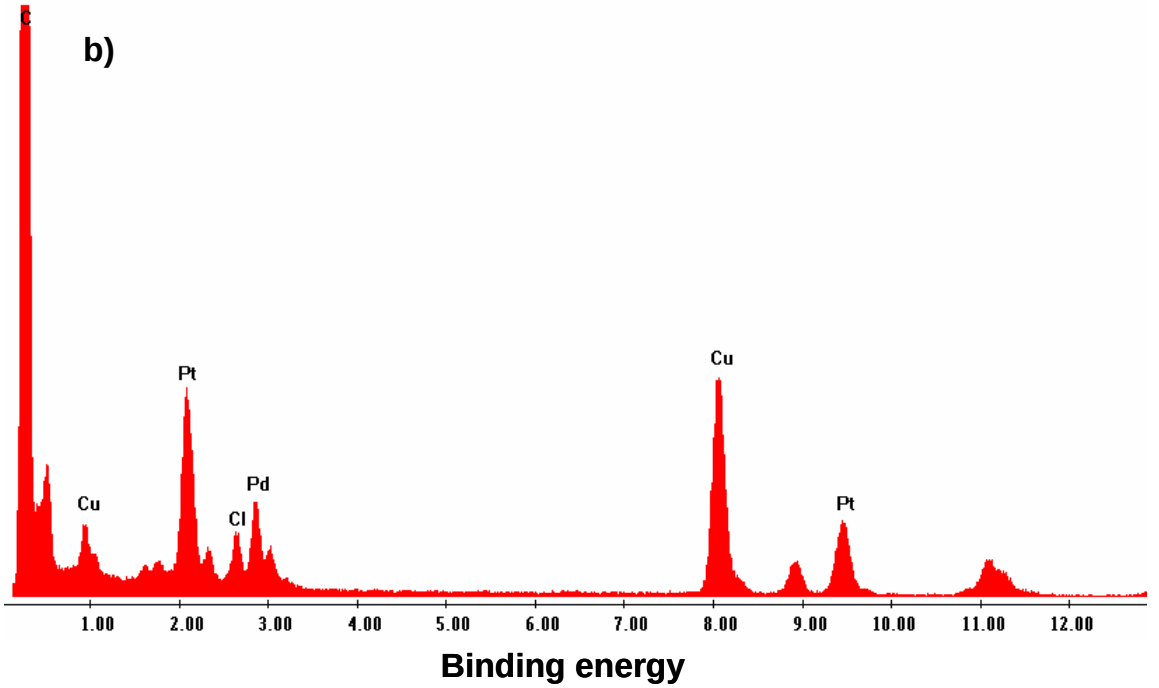

Figure 3.22. The spectra of EDS in HRTEM showing a) Pd@Pt, b) Pt@Pd.

Table 3.4. Compositions of Pd@Pt and Pt@Pd NPs by EDS in HRTEM.

Materials	Pd (atomic %)	Pt (atomic %)
Pd@Pt	50.5	49.5
Pt@Pd	43.9	56.1

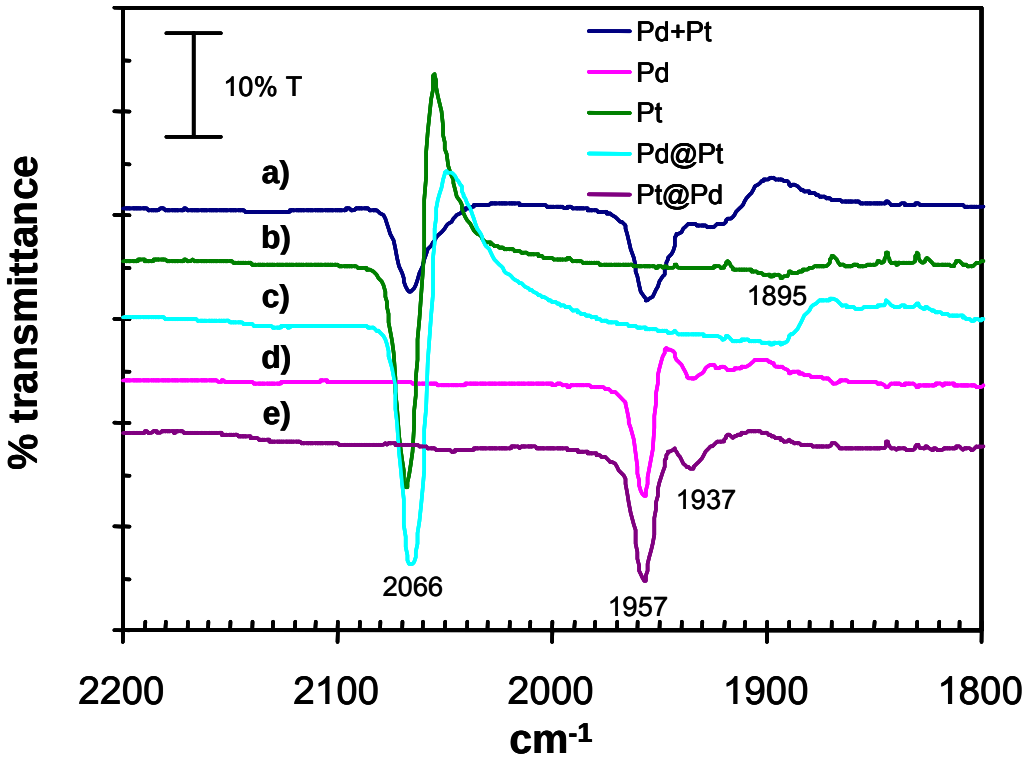

Figure 3.23. FTIR spectra of CO adsorbed on metal NPs showing a) the physical mixture of Pd and Pt colloid, b) Pt colloid, c) Pd@Pt colloid, d) Pd colloid, and e) Pt@Pd colloid.

3.3.6. NO Reduction in Lean-burn Conditions with Monometallic Pd and Pt NPs

In lean-burn conditions of hydrocarbon fuels (engines and power generators), there is a large excess of O_2 that makes selective reduction of NO_x with H_2 (or excess fuel) very chanllenging. Considering the ratio of O_2 to NO_x, which is usually from 5 to 20, the

selective reduction of NO_x by hydrogen will require highly selective catalysts. The possible products of NO_x reduction by H_2 are N_2O, NO_2, and N_2.[149] The "deep reduction" product-NH_3 is usually not observed due to the net oxidizing environment.[149] The following equations show all the possible reactions.

$$2NO+2H_2 \rightarrow N_2+2H_2O \quad (1)$$

$$2NO+H_2 \rightarrow N_2O+H_2O \quad (2)$$

$$2NO+O_2 \rightarrow 2NO_2 \quad (3)$$

$$2H_2+O_2 \rightarrow 2H_2O \quad (4)$$

Monometallic Pd, Pt and Rh catalysts have been used in stoichiometric gasoline engines (*i.e.* no excess O_2) at 400°C -800°C for past several decades. They are efficient in removing NO_x, CO and unburned hydrocarbons, and are referred to as three way catalysts (TWCs).[130] However, with exhaust containing a large excess of oxygen in the same temperature range, TWCs do not function properly. While Pd and Pt catalysts are inefficient for lean-burn NO_x reduction at high temperatures, it was found by Hamada and Obuchi that Pd and Pt catalysts perform well at low temperatures (typically below 300°C, the operating temperatures for LB engine).[163, 164] After their excellent work, the selective catalytic reduction of NO_x with hydrocarbons (HC-SCR) using platinum group metal catalysts was intensely investigated, and great advances have been achieved in the past decades. However the application of SCR catalysts still hides somewhere in the future.

In contrast to conventional catalysts, the work described here employed well-characterized metal colloids as active components. By this method, the effect of particle size can be clearly seen. In the following sections, standard operating conditions are

given in the experimental section. All the metal loading of supported catalysts is 1.0 wt% except where noted.

Figure 3.24 shows the temperature programmable reaction (TPR) for lean NO_x reduction using Pd/γ-alumina. Prior to 120°C, NO_2 formation is dominant, and occurs through a non-catalyzed gas phase reaction between NO and O_2. This process is well known and is a main pathway for NO_2 formation in environment, which causes acid rain. Catalytic conversion of NO and NO_2 starts from 120°C. The major product is N_2, and at 178°C the N_2 yield reaches 43% with a selectivity of 79%. Here, the selectivity for N_2 is calculated by dividing the N_2 yield by the NO conversion. As the reaction temperature increases, the N_2 yield decreases. N_2O formation reaches a maximum at 178°C, and remains constant at high temperatures. While the Pd catalyst shows a low activity (30-50% in the temperature range of 160-390°C), it is a highly selective NO reduction catalyst with a N_2 selectivity of 60-80%.

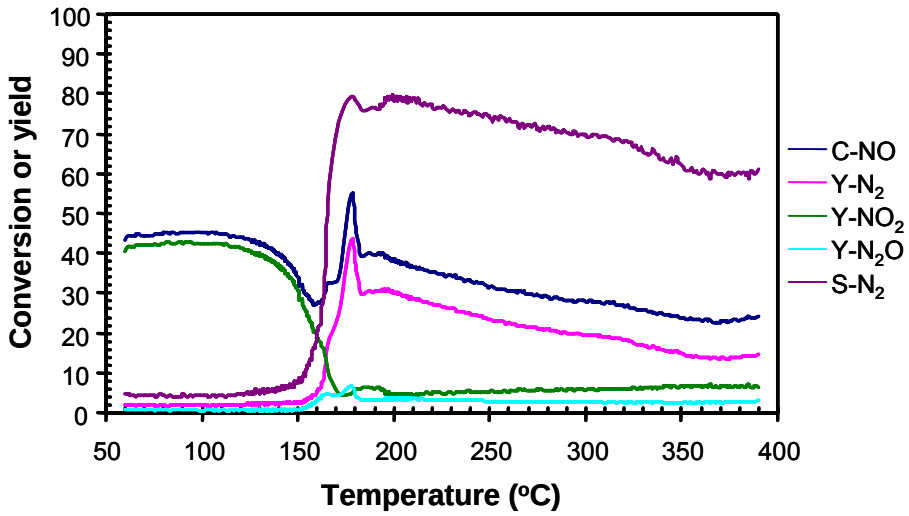

Figure 3.24. Temperature programmable reaction with $NO/H_2/O_2$ showing the catalytic performance of Pd/γ-alumina catalyst (11.5 nm Pd). The y-axis represents the conversion of NO (C-NO), selectivity of N_2 (S-N_2), yields of N_2 (Y-N_2), yield of NO_2 (Y-NO_2) and yield of N_2O (Y-N_2O). The selectivity of N_2 is calculated by dividing Y-N_2 by C-NO. The reactant mixture contains 0.75% NO, 3% H_2, 5% O_2 and Ar balance.

In contrast to the Pd catalyst, the Pt catalyst shows a higher activity (Figure 3.25). The lightoff temperature decreases from 152°C (Pd catalyst) to 92°C.The catalytic conversion of NO_x starts from 80°C. The conversion of NO is above 32% in the temperature range from 95°C to 384°C, and reaches a maximum of 73% at 113°C. The N_2 yield reaches a maximum of 43% with an N_2 selectivity of 68%, and then decreases followed by an increase from 255°C. The big difference between the Pd and Pt catalysts is that for the Pt/alumina catalyst, significant N_2O formation is observed in the temperature range from 94°C to 121°C, and at high temperatures, the NO conversion and the N_2 selectivity increases as temperature increases. Considering the conversion and selectivity, the Pt catalyst has a better performance than the Pd catalyst.

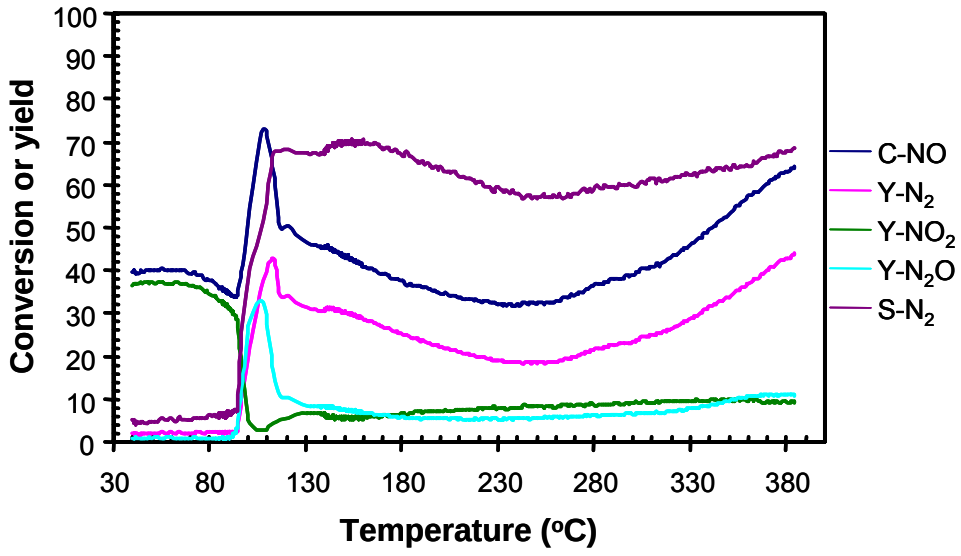

Figure 3.25. Temperature programmable reaction with $NO/H_2/O_2$ showing the catalytic performance of the Pt/γ-alumina catalyst (15.3 nm Pt). The reactant mixture contains 0.75% NO, 3% H_2, 5% O_2 and Ar balance.

To test the effect of particle size on catalytic performance, oleylamine protected 4.5 nm Pt NPs and dendrimer protected 1.3 nm Pt NPs were synthesized. Figure 3.26 shows the TPR of the supported 4.5 nm Pt catalyst. The lightoff temperature is 60°C, 32°C lower

than that of the 15.3 nm Pt catalyst. In the temperature range from 70°C to 390°C, the NO conversion is above 50%, and the N_2 selectivity is 60-80%. The N_2 yield reaches a maximum of 52% at 250°C with an N_2 selectivity of 75%. Figure 3.27 shows TPR of the 1.3 nm Pt catalyst. To remove the stabilizing agent (dendrimers), the supported 1.3 nm Pt catalyst was calcined in an Ar stream with 3% of O_2 at 400°C for 2 hours followed by reduction with H_2. This catalyst shows the highest activity. The maximum NO conversion reaches 95%. In the temperature range from 100°C to 400°C, the N_2 selectivity is 50-65%.

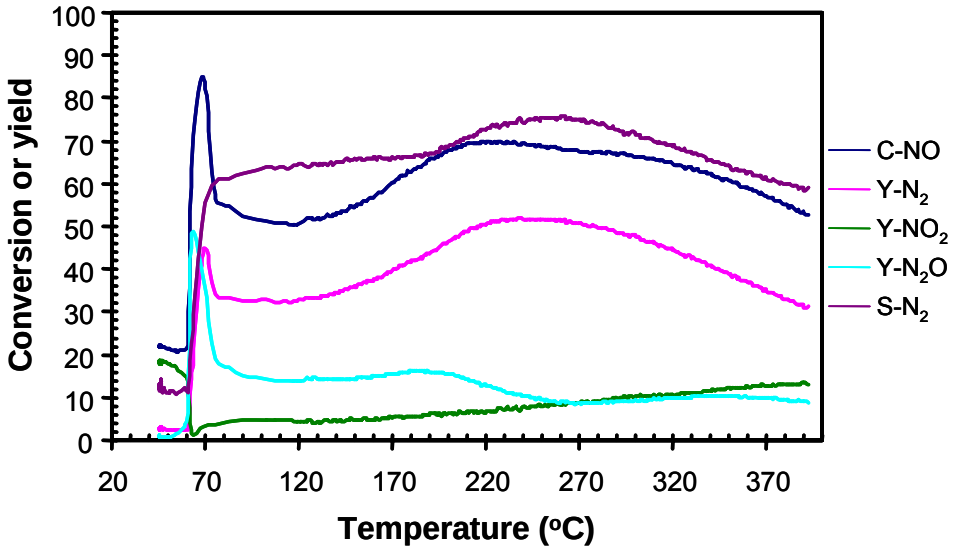

Figure 3.26. Temperature programmable reaction with $NO/H_2/O_2$ showing the catalytic performance of the Pt/γ-alumina catalyst (4.5 nm Pt). The reactant mixture contains 0.75% NO, 3% H_2, 5% O_2 and Ar balance.

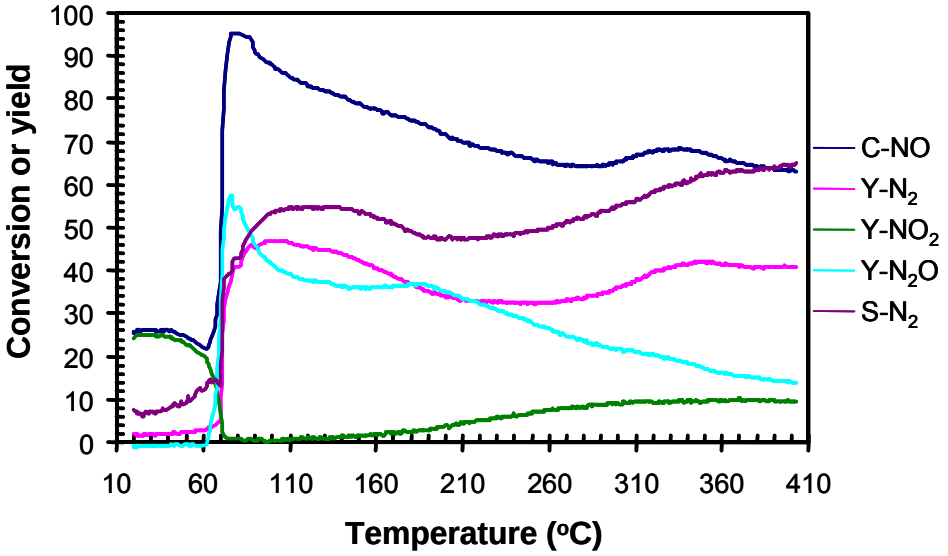

Figure 3.27. Temperature programmable reaction with $NO/H_2/O_2$ showing the catalytic performance of the Pt/γ-alumina catalyst (1.3 nm Pt). The reactant mixture contains 0.75% NO, 3% H_2, 5% O_2 and Ar balance.

To clearly demonstrate the particle size effect on catalytic performance, all the TPRs of different Pt catalysts were ploted in Figure 3.28. It is clearly shown that the small particles enhance the activity, as indicated by the decreasing order of NO conversions from the 1.1 nm Pt, 4.5 nm Pt to 15.3 nm Pt NPs. However, for the N_2 selectivity, the 1.1 nm Pt catalyst shows the worst selectivity. The highest N_2 selectivity was observed in the 4.5 nm Pt catalyst. For overall catalytic performance, the 4.5 nm Pt catalyst seems to show the optimum combination of conversion and selectivity. The reason of 4.5 nm Pt showing optimum performance is not clear at this time, and may relate to the fine surface structure of the particles.

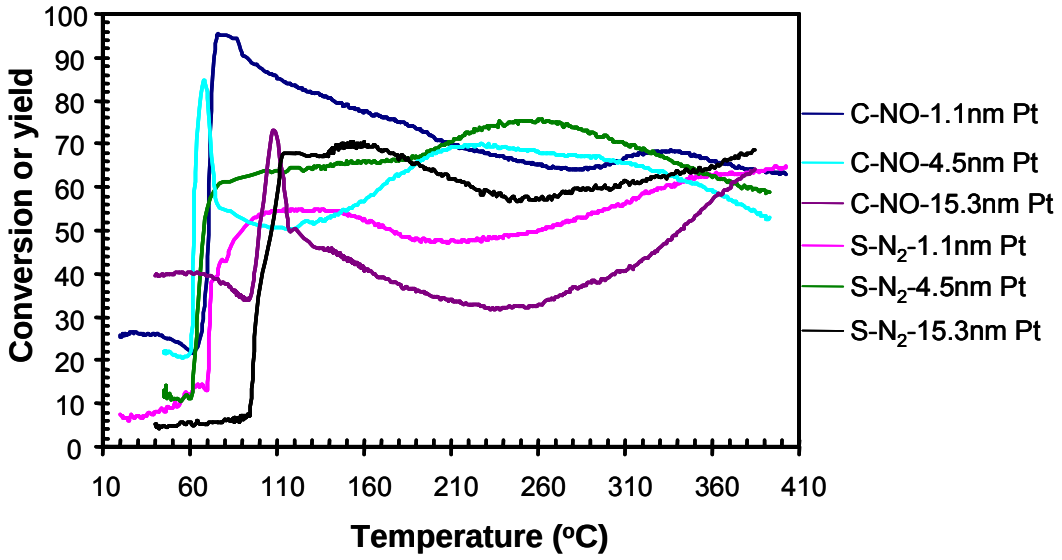

Figure 3.28. Comparison of the catalytic performances of the Pt catalysts with different particle size. The reactant mixture contains 0.75% NO, 3% H_2, 5% O_2 and Ar balance.

Due to different reaction conditions reported in the literature, direct comparison of different catalysts is difficult. Costa and co-workers reported a highly active and selective catalyst-Pt/$La_{0.5}Ce_{0.5}MnO_3$ (Pt/LCM, 0.1wt% Pt loading). In our lab, the Pt/LCM catalyst was prepared by the literature method and tested at the same conditions for comparison. Figure 3.29 shows the TPR of the Pt/γ-alumina catalyst (15.3 nm Pt, 0.1% metal loading same as the Pt/LCM). The NO conversion and the N_2 selectivity do not show a significant difference between 1.0% loading and 0.10% loading. However, the 0.1% loading has a lightoff temperature of 144°C, 52°C higher than the 1.0% loaded catalyst. Figure 3.30 shows TPR of the Pt/LCM catalyst. The NO_2 formation at room temperature is significantly lower than that of the Pt/γ-alumina catalyst, suggesting that the Pt/LCM can convert NO_2 (formed by the gas phase reaction) back to NO. However, NO and NO_2 are all pollutants. Transformation between NO and NO_2 is not helpful in this regard. At high temperatures, the NO conversion over the Pt/LCM catalyst is higher than that of the Pt/γ-alumina catalyst. However, N_2O is the major product in most temperatures tested, leading

to a relatively low selectivity for N_2. The maximum N_2 yield for the Pt/LCM catalyst is 33%. In contrast, the 15.3 nm Pt/γ-alumina catalyst shows a maximum of 55%. In comparing theses two catalyst, the Pt/γ-alumina catalyst prepared by the nanoparticle colloid method in this work has a better catalytic performance.

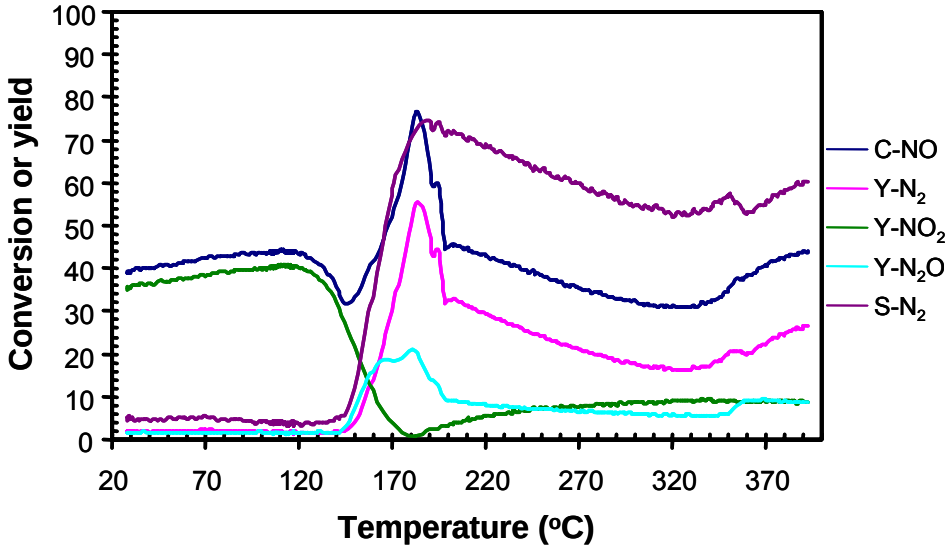

Figure 3.29. TPR of the 15.3 nm Pt/alumina catalyst with a Pt loading of 0.1%. The reactant mixture contains 0.75% NO, 3% H_2, 5% O_2 and Ar balance.

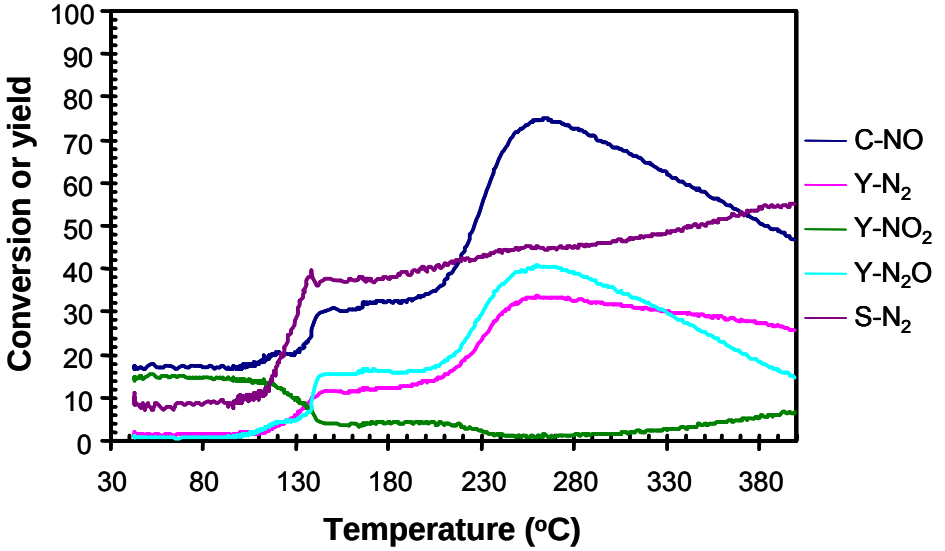

Figure 3.30. TPR of the Pt/LCM catalyst with a Pt loading of 0.1%. The reactant mixture contains 0.75% NO, 3% H_2, 5% O_2 and Ar balance.

3.3.7. NO Reduction with H_2 Using Monometallic NPs

In the absence of O_2 (rich conditions), these catalysts have a better catalytic performance for de-NO_x reactions. Literature studies revealed that the possible products are N_2, N_2O, and NH_3.[147, 148] In contrast to lean-burn conditions, NO_2 is absent in the product mixtures under rich conditions due to a net reducing environment. The following equations show all the possible reactions. From these equations, it is apparent that higher NO/H_2 ratios give deeper reduction products.

$$2NO+4H_2 \rightarrow 2NH_3+H_2O \quad (1)$$

$$2NO+2H2 \rightarrow N_2+2H_2O \quad (2)$$

$$2NO+H_2 \rightarrow N_2O+H_2O \quad (3)$$

Figure 3.31 shows the de-NO_x reaction with the 11.5 nm Pd catalyst. The NO conversion is significantly higher than the NO conversion under lean-burn conditions. At low temperatures, N_2O is the major product, and at high temperatures, NH_3 is the major products. The N_2 yield is below 12% in the whole temperature range. At 1/1 H_2/NO ratio, the NO conversion decreases, and the N_2 yield increases (Figure 3.32). However, the N_2 yield is still low, and the N_2 selectivity is below 50% (not shown in the figure for clarity).

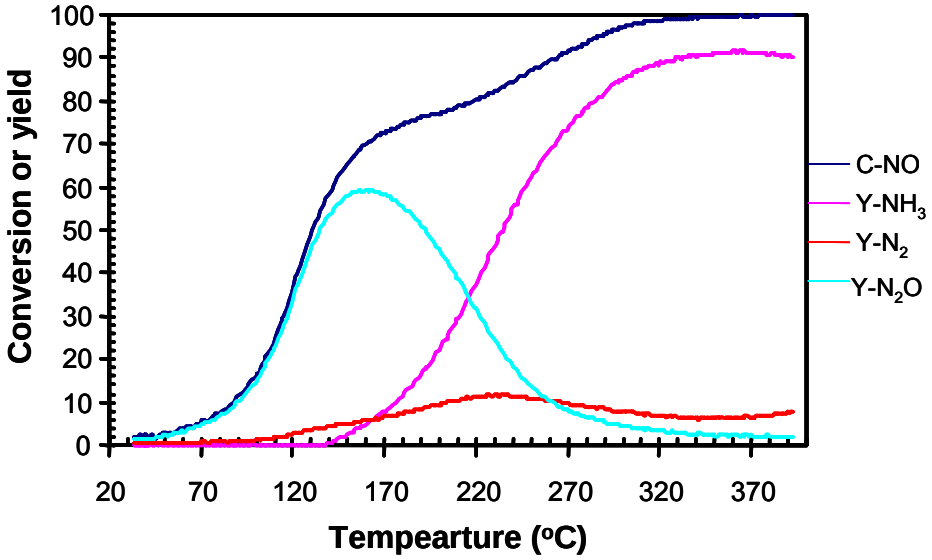

Figure 3.31. TPR of the Pd/γ-alumina with a Pd loading of 1% (11.5 nm). The reactant mixture contains 0.75% NO, 3% H_2 and Ar balance.

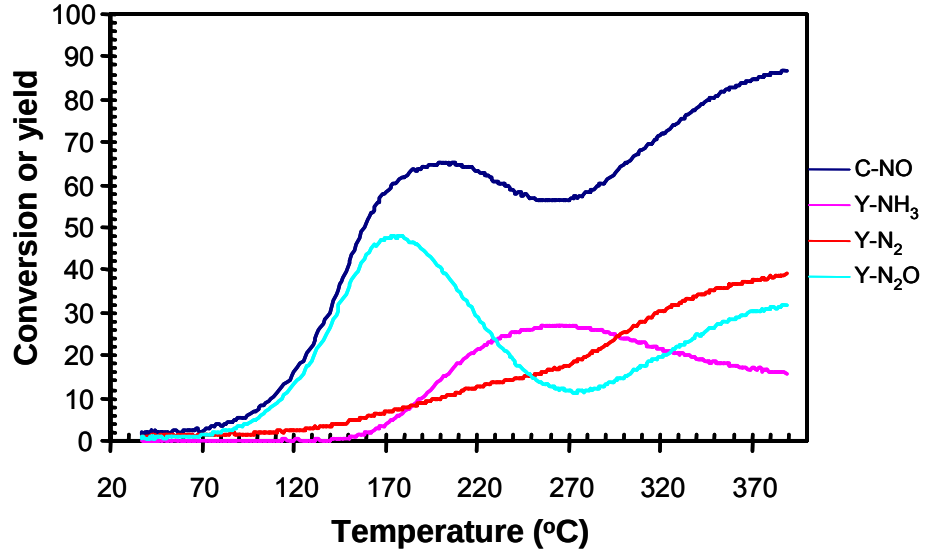

Figure 3.32. TPR of the Pd/γ-alumina with a Pd loading of 1% (11.5 nm). The reactant mixture contains 0.75% NO, 0.75% H_2 and Ar balance.

Figure 3.33 shows the TPR of the 15.3 nm Pt/γ-alumina catalyst under 4/1 H_2/NO conditions. This catalyst shows a high activity. The NO conversion reaches 100% at 108°C. N_2O formation reaches a maximum at 104°C, and then decreases as temperature increases. NH_3 formation increases as temperature increases, and is the main reaction at

high temperatures. While the N_2 yield is higher than the Pd catalyst under the same conditions, N_2 is still a minor product (around 20%). At 1/1 H_2/NO ratio the NO conversion decreases compared to that of 4/1 H_2/NO ratio, and reaches the first maximum at 153°C, and then decreases followed by increasing again (Figure 3.34). As expected, the NH_3 formation is significantly lower than under a 4/1 ratio of H_2 to NO. The N_2 yield reaches 20% at 150°C, and remains unchanged in the temperature range from 150°C to 350°C. From 350°C, the N_2 yield then sharply increases and reaches 76% at 392°C. The maximum of N_2 selectivity is 80%, which is consistent with the reported result of a 5% Pt/silica catalyst.[147, 148] Apparently, the Pt catalyst has a better performance than the Pd catalyst.

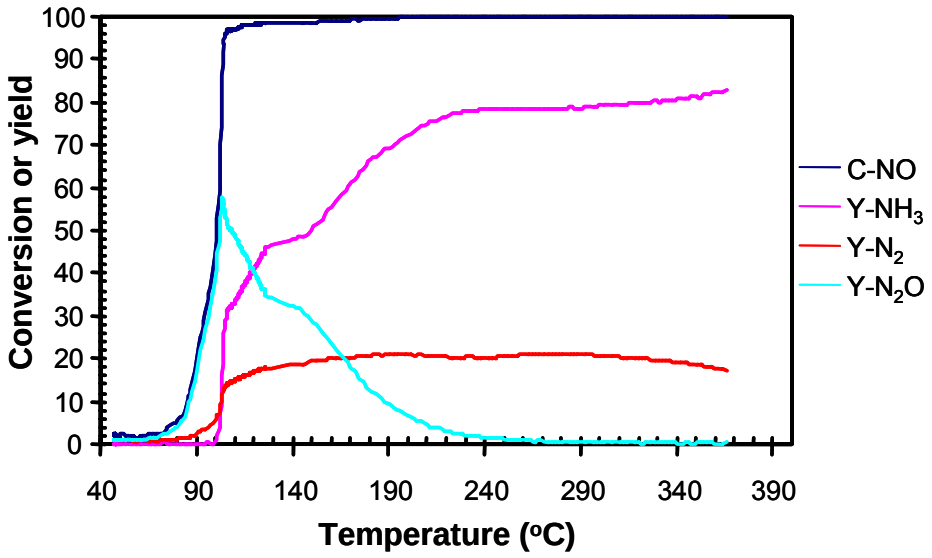

Figure 3.33. TPR of the Pt/γ-alumina with a Pt loading of 1% (15.3 nm). The reactant mixture contains 0.75% NO, 3% H_2 and Ar balance.

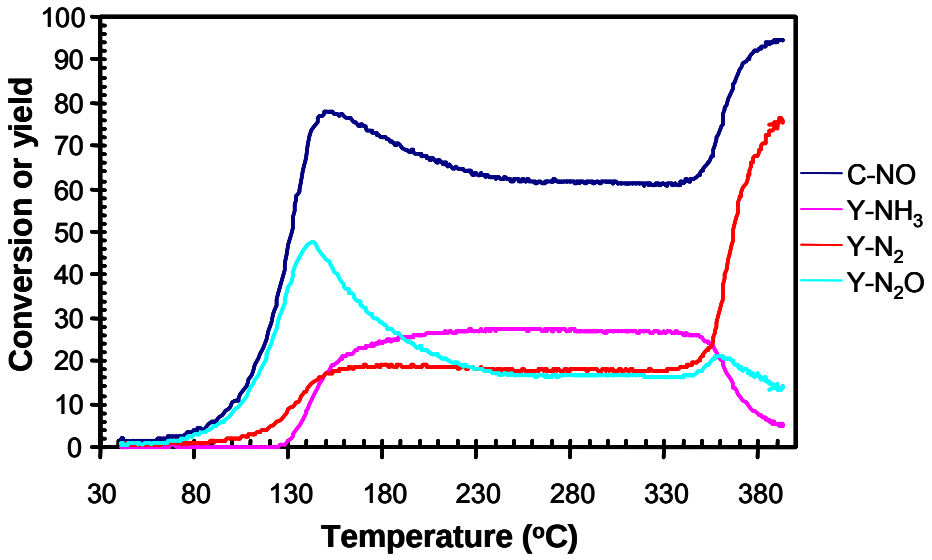

Figure 3.34. TPR of the Pt/γ-alumina with a Pt loading of 1% (15.3 nm). The reactant mixture contains 0.75% NO, 0.75% H_2 and Ar balance.

Figure 3.35 shows the TPR of the 4.5 nm Pt/γ-alumina catalyst under a 4/1 H_2/NO ratio. The lightoff temperature is 50°C, 34°C lower than that of the 15.3 nm Pt catalyst. The trends for N_2O and NH_3 formation are the same as for the 15.3nm Pt catalyst. The N_2 yield reaches a maximum of 25% at 180°C, and then decreases as the temperature increases. At 380°C, the N_2 yield of is only 4%. While small Pt NPs exhibit a high activity, they are selective for NH_3 formation under 4/1 H_2/NO conditions (95% at 380°C), with a 1/1 H_2/NO ratio (Figure 3.36), all of the NO conversion and the N_2 yield is higher than those of the 15.3 nm Pt catalyst. The NO conversion reaches the first maximum of 98% at 109°C, and then decreases followed by increasing again. At 295°C the NO conversion reaches 100%. The N_2 yield approaches the first maximum of 40% at 103°C, and then decreases followed by sharp increase during the temperature range from 225 to 280°C. At 290°C the N_2 yield is 87%, and remains unchanged from 290°C to 390°C. The maximum N_2 selectivity is 88%.

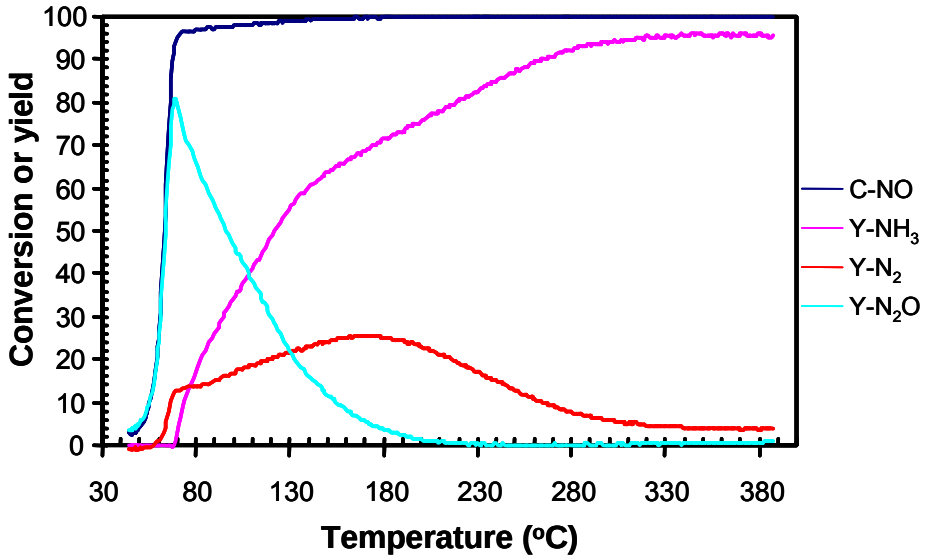

Figure 3.35. TPR of the Pt/γ-alumina with a Pt loading of 1% (4.5 nm). The reactant mixture contains 0.75% NO, 3% H_2 and Ar balance.

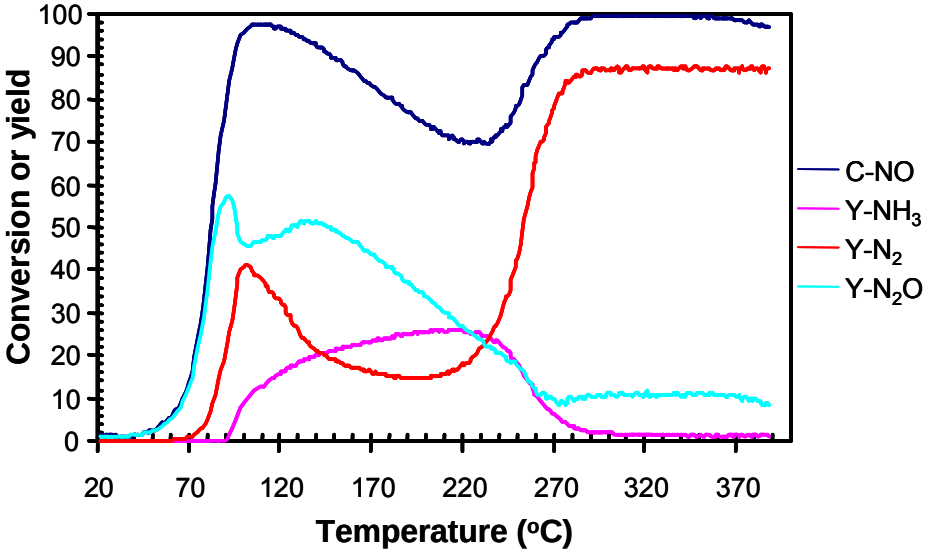

Figure 3.36. TPR of the Pt/γ-alumina with a Pt loading of 1% (4.5 nm). The reactant mixture contains 0.75% NO, 0.75% H_2 and Ar balance.

3.3.8. NO Reduction with H_2 Using Bimetallic Core-shell NPs

Bimetallic catalysts have wide application in heterogeneous catalysis. The common industrial catalyst applied wet impregnation method using precursor solution. Although

some catalysts prepared by this method perform well, obtaining the phase information of the active components is difficult. In this work well-characterized bimetallic nanoparticle colloids were used as the active components. By this method, the catalytic performance can be easily assigned to the known structure and phase. The first class of bimetallic catalyst tested is copper-based alloy catalysts. CuPd and CuPt alloy catalysts were tested for de-NO_x reactions under NO/H_2 conditions (oxygen free). Figure 3.37 shows the TPR of the PtCu alloy catalyst under a 4/1 H_2/NO ratio. The result shows that the N_2 selectivity increases to 50% at the expense of activity when compared to the pure Pt catalysts. The same phenomenon was observed in the CuPd alloy catalyst. The selectivity enhancement is assigned to the interaction between the Cu and noble metals. However, the surface noble metal atoms are diluted by Cu, which causes an activity drop. To avoid the activity drop, Cu@Pt core-shell structures were designed and tested for de-NO_x reactions under NO/H_2 conditions.

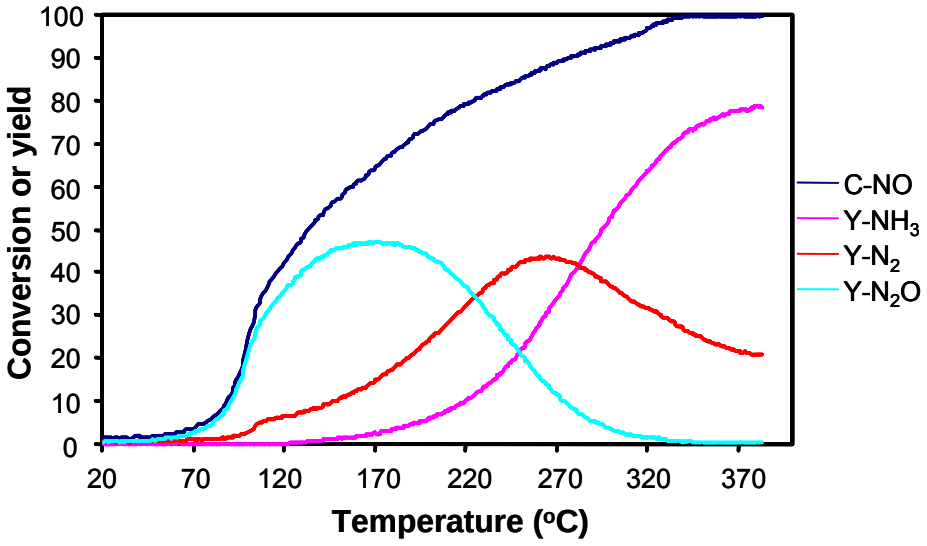

Figure 3.37. TPR of the CuPt/γ-alumina with a Pt loading of 1% (Cu/Pt 1/1). The reactant mixture contains 0.75% NO, 3% H_2 and Ar balance.

Figure 3.38 shows the TPR of the Cu@Pt catalyst for the de-NO_x reaction with a 4/1 H_2/NO ratio. Although the NH_3 is still the main reaction product, the N_2 selectivity is significantly higher than the pure Pt catalyst. The maximum N_2 selectivity is 43% at 155°C. In contrast, for the pure Pt catalyst (4.5 nm) the maximum is 25%. With a 1/1 H_2/NO ratio, the N_2 selectivity reaches 93% (Figure 3.39), which is higher than the Pt catalyst at the same conditions. Although the difference is not as large as the difference under the 4/1 H_2/NO conditions, it is expected because the 1/1 H_2/NO ratio favors the N_2 formation. The interaction between the core metal Cu and shell metal Pt changes the electronic properties of Pt, resulting in a N_2 selectivity enhancement.

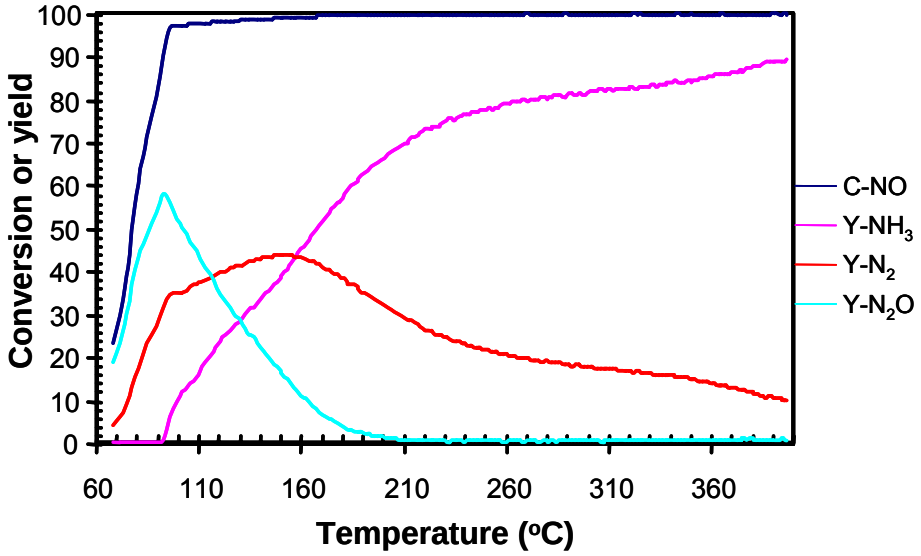

Figure 3.38. TPR of the Cu@Pt/γ-alumina with a Pt loading of 1% (Cu/Pt 1/1). The reactant mixture contains 0.75% NO, 3% H_2 and Ar balance.

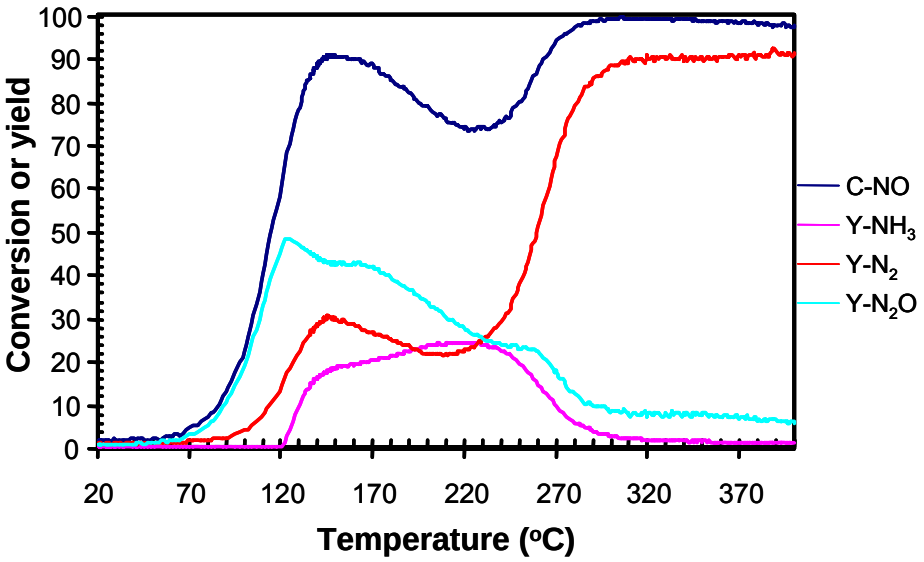

Figure 3.39. TPR of the Cu@Pt/γ-alumina with a Pt loading of 1% (Cu/Pt 1/1). The reactant mixture contains 0.75% NO, 0.75% H_2 and Ar balance.

Recently, the near surface alloy (NSA) theory suggested that the surface alloy structure may have activity and selectivity enhancements.[76, 77] NSA structure contain the second metal layers below the surface metal monolayer. This type of structure is easy to make on bulk scale (i.e. one monolayer of surface metal on the second metal single crystal). However, bulk materials have low percentage of surface atoms, and are not efficient in heterogeneous catalysis. Core-shell nanostructures are designed to address this problem. Core-shell structures can keep the metal-metal interactions and avoid the dilution effect by the second less active metal on the surface. Cu@Pt is a good example. The N_2 selectivity of the Cu@Pt catalyst under a 4/1 H_2/NO ratio is significantly higher than the pure Pt catalyst, and the high activity of the Pt component is retained. To further prove this principle, Pd@Pt and Pt@Pd core-shell structures were synthesized and tested for de-NO_x reactions under the 4/1 H_2/NO conditions. The choice of these reaction conditions is that the difference of N_2 selectivity is accentuated under high H_2/NO ratios. Figure 3.40

shows the TPR of the Pd@Pt catalyst. The highest N_2 selectivity is 62%, which is significantly higher than that of the pure Pt catalyst. The lightoff temperature is 72°C, which is comparable to that of the pure Pt catalyst. In the Pt@Pd system (Figure 3.41), both the selectivity and activity were enhanced relative to the pure Pd catalyst. The highest N_2 selectivity is 50%, and at 100°C the NO conversion approaches 100%. In contrast, the pure Pd catalyst shows a maximum N_2 selectivity of 15%, and at 320°C the NO conversion approaches 100%.

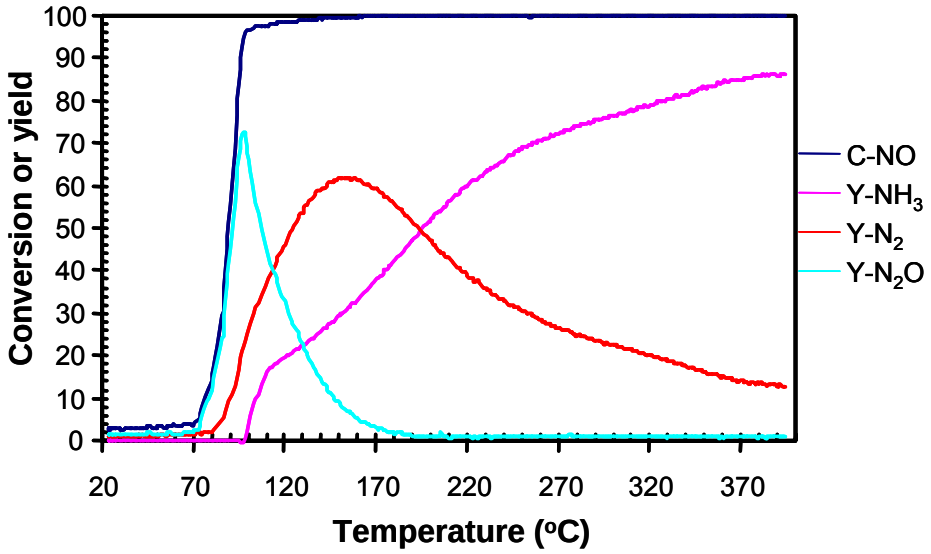

Figure 3.40. TPR of the Pd@Pt/γ-alumina with a Pt loading of 1% (Pd/Pt 1/1). The reactant mixture contains 0.75% NO, 3% H_2 and Ar balance.

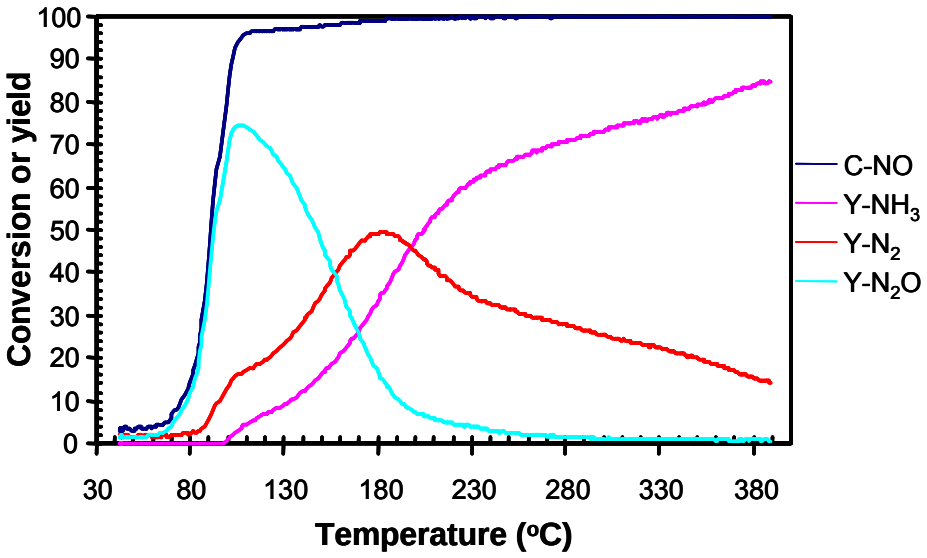

Figure 3.41. TPR of the Pt@Pd/γ-aluminaad with a Pt lo ing of 1% (Pd/Pt 1/1). The reactant mixture contains 0.75% NO, 3% H_2 and Ar balance.

3.3.9. Stability Test of Cu@Pt Catalyst under NO/H_2 Conditions

As shown in the annealing experiments of Cu@Pt NPs, Cu@Pt NPs are abnormally stable to alloy formation at high temperatures. The XRD pattern of Cu@Pt annealed at 370°C for five hours under vacuum shows a nearly pure Pt surface. In contrast, the Pt@Cu NPs readily transform into the alloy structures as expected from the thermodynamic phase diagram. To further prove the abnormal stability of Cu@Pt NPs, de-NO_x reactions under NO/H_2 conditions were used to monitor the structural change of Cu@Pt, Pt@Cu and PtCu NPs. To highlight the different thermal stabilities of these bimetallic catalysts, de-NOx reactions were carried out under a 4/1 H_2/NO ratio at 360°C (Figure 3.42 left panel). After 5.8 hours, the reaction was switched to a 1/1 H_2/NO ratio and run for additional 0.7 hours to clearly see the change of activity and selectivity (Figure 3.42 right panel). For the Cu@Pt nanoparticle catalyst, the NO conversion and N_2 selectivity in either reaction conditions are stable and the NO conversion is significantly

higher than those of the other bimetallic systems. XRD patterns of the Cu@Pt catalyst after reaction does not show any sign of PtCu alloy formation, indicating that the Cu@Pt particles are stable under these conditions (Figure 3.43g). This observation is consistent with the annealing experiment. In contrast, the PtCu alloy catalyst is deactivated quickly and then stabilizes with a NO conversion of 27%. Post XRD analysis shows an increase of crystallinity (Figure 3.43e), which may explain the activity drop. The Pt@Cu catalyst does not show significant activity as expected, and after three hours the N_2 selectivity becomes equivalent to that of PtCu. XRD pattern of the post reaction Pt@Cu catalyst shows complete alloying (Figure 3.43c), which is consistent with its annealing behavior. The final NO conversion of the alloyed Pt@Cu particle (17 %) is lower than that of the PtCu alloy (27 %), which is consistent with the significantly larger mean particle size of the Pt@Cu catalysts. Importantly, the Cu@Pt nanocatalyst is markedly better in activity as well as stability than the other two bimetallic catalysts.

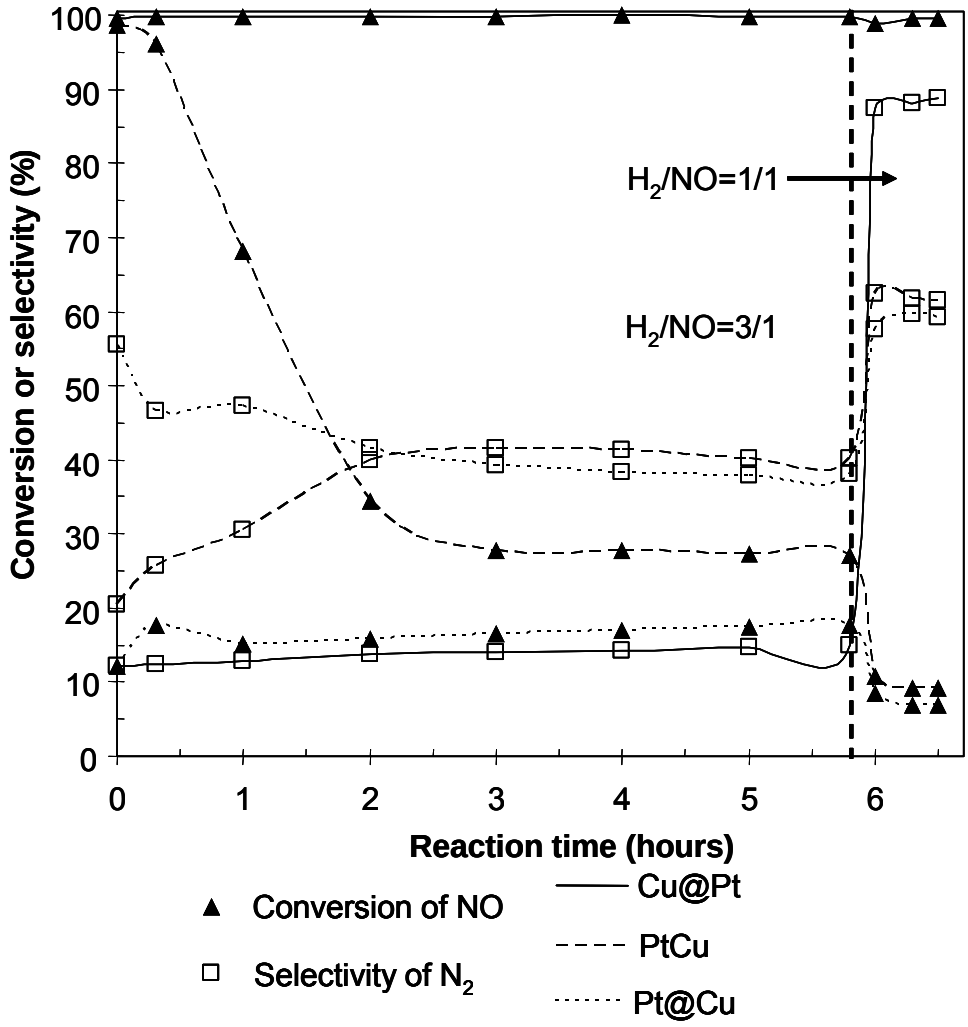

Figure 3.42. Stability tests for PtCu, Pt@Cu, and Cu@Pt nanocatalysts in the reduction of NO with H_2. The profiles for a 4:1 H_2/NO mixture (reaction time up to 5.8 h) are shown on the left. The subsequent reaction profiles for a 1:1 H_2/NO mixture are shown on the right.

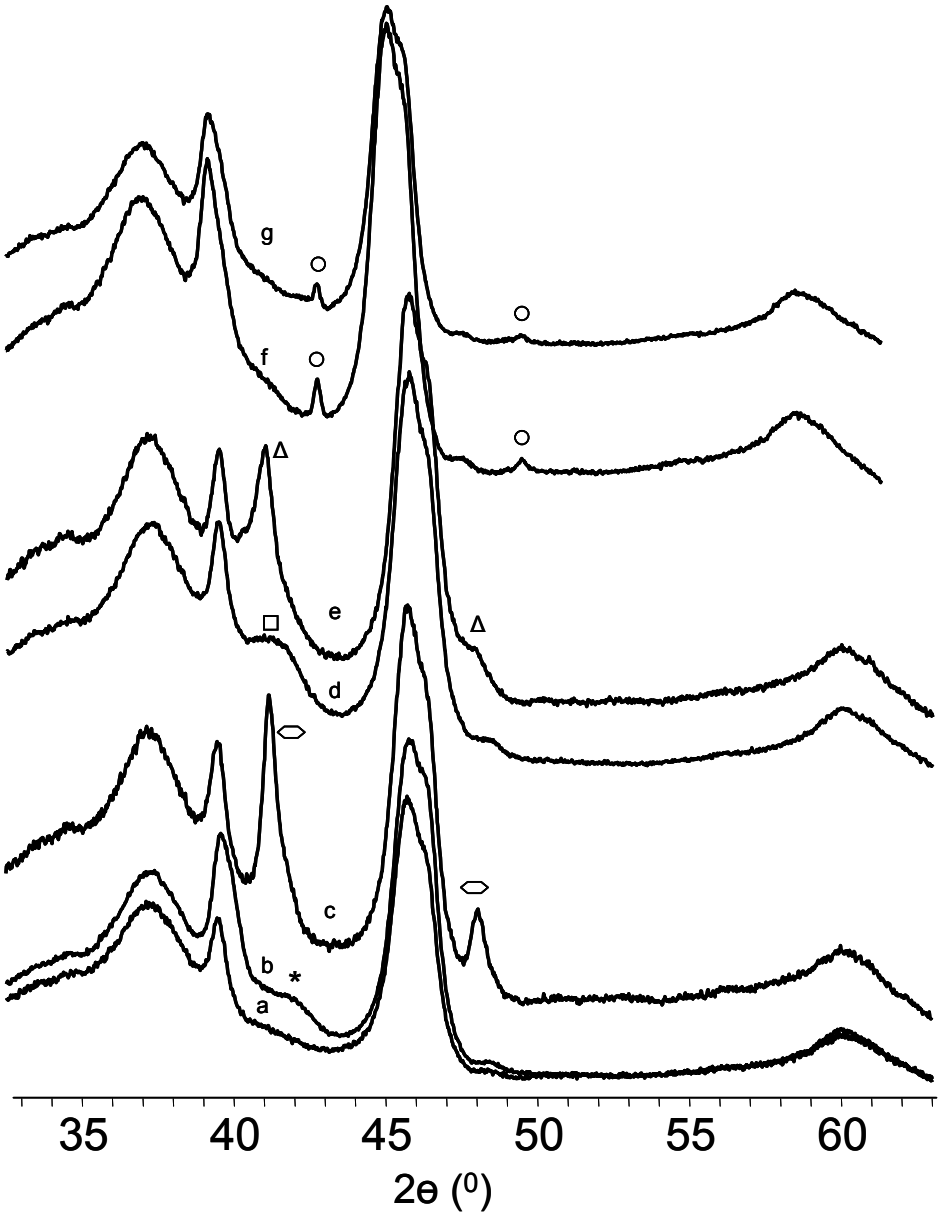

Figure 3.43. XRD patterns of Cu@Pt, Pt@Cu and CuPt catalyst after stability test. a) Gamma-alumina, b) Pt@Cu/gamma-alumina, star indicates the $Cu_{0.8}Pt_{0.2}$ shell, c) Pt@Cu/gamma-alumina after reaction, hexagon indicate PtCu alloy (JCPDS 29-0547), d) PtCu/gamma-alumina, square indicates as prepared PtCu (JCPDS 42-1326), e) PtCu/gamma-alumina after reaction, triangle indicates PtCu alloy(JCPDS 48-1549), f) Cu@Pt/gamma-alumina, circle indicates Cu (JCPDS 04-0836), g) Cu@Pt/gamma-alumina after reaction, circle indicates Cu (JCPDS 04-0836). NOTE: Pt peaks are obscured by Gamma-alumina.

3.4. Dissicusion

According to the phase diagram of PdCu, the α PdCu phase is generated at high temperatures (above 550^{o}C). Solution-based chemistry provides a simple way to synthesize materials that otherwise requires high temperatures in bulk method. α solid solution is generated in 2-ethoxyethanol. Upon annealing α phase transforms into the more stable β phase. This phenomenon is unique. The solvent may provide some stabilizing effect for the formation of metastable materials.

As shown in the annealing behavior of as prepared Pt-Cu core-shell NPs, the Pt@Cu readily transforms into alloy structures. However the Cu@Pt NPs are kinetically stable upon heating. We attribute this anomalous stability to Kirkendall mass-transport phenomena in which the net mass transport is balanced by the vacancy transport in the opposite direction. In the Cu-Pt diffusion couple the diffusion efficiency from Pt to Cu is significantly larger than from Cu to Pt. For example at 960^{o}C the diffusion efficiency from Pt to Cu is 6×10^{-7} $cm^2\ h^{-1}$. However at an even high temperature 1041^{o}C the diffusion efficiency from Cu to Pt is 8×10^{-8} $cm^2\ h^{-1}$. In the Pt@Cu core-shell NPs, the net mass transport at Pt-Cu interface strongly favors the Pt diffusion into Cu. Due to the large population of vacancies in Cu shells of the Pt@Cu NPs, the Pt diffusion to Cu can be easily balanced by the vacancy transport from Cu to Pt and results in facile PtCu alloy formation. In contrast, Cu@Pt NPs are kinetically stabilized upon annealing because the Pt diffusion to Cu is hindered due to a limited population of vacancies in Cu cores. Moreover, in the catalytic reaction H_2 provides an additional stabilizing effect for Cu@Pt. The alloy formation is unfavorable due to the high binding enthalpy between Pt atoms and H atoms.

In the conventional method for preparation of heterogeneous catalysts, adjusting metal dispersion (particle size) is difficult. Metallic nanoparticle colloids provide a simple way to tune particle size and assign performance to known structures. As shown in the syntheses of Pt NPs, the particle size is adjusted by the stabilizing agents. PVP, oleylamine and dendrimer produce Pt NPs with different particle sizes. Smaller particles afford higher activity. This is consistent with the reports in the literature. Alloy PdCu and PtCu catalysts show a high selectivity due to metal-metal interactions. However, the surface active atoms are diluted by the less active metal atoms that cause activity to drop. Core-shell structures provide an elegant way to maintain the metal-metal interactions and the active metal atoms on the surfaces. As shown in the Cu@Pt and Pd@Pt catalysts, the N_2 selectivity is enhanced for the NO/H_2 reactions, and the activity is similar as that of pure Pt catalysts. For Pt@Pd catalyst, the N_2 selectivity and activity are enhanced compared to those of the pure Pd catalyst. This may be explained by the near surface alloy theory. The core-shell interactions weaken the H binding on Pd atoms and also facilitate H_2 dissociation, which further enhances the overall H activation. In addition, the Pd-Pt interaction changes the electronic properties of Pd atoms, and results in the selectivity enhancements.

Chapter 4

Conclusion

Development of heterogeneous catalysts is a time-consuming process, especially for industrial catalysts. For example, scientists and engineers have put more than fifty years of effort into improving the ammoxidation catalysts for acrylonitrile production. Since 1960, BP chemicals has developed seven generations of Mo-Bi ammoxidation catalysts, and an effort to improve the catalyst continues on.

Unlike other areas of chemistry, development of heterogeneous catalysts is achieved mainly through experience, especially for industrial catalysts that in some cases contain more than ten components. Scientists are eager to design heterogeneous catalysts by theories and principles. To date, a limited number of successful examples have been achieved in idealized catalyst on small molecules.

In this study, different architecturally controlled bimetallic nanomaterials were synthesized and applied in CO tolerant hydrogen activation and de-NO_x reactions by hydrogen. As shown in Chapter 2 and Chapter 3, many important contributions have been given to chemical community. These contributions can be separated into two areas-designs of heterogeneous catalysts and synthetic method development for material synthesis. The detailed discussion is shown in the following sections.

4.1. Designs of Heterogeneous Catalysts

Recently, near surface alloy (NSA) theory developed by Mavrikakis and co-workers suggests that NSAs have a higher hydrogen activation compared to pure metals. The authors deal with the idealized system and calculate hydrogen binding energies by

quantum chemical methods. Although the NSA theory can explain the behavior of some idealized systems, such as weaker CO binding on thin layers of platinum on Ru(0001) crystals[78] and faster CO hydrogenation on vanadium dosed Pd(111) surface,[165] the real heterogeneous catalytic process is much more complicated. Any further theoretical simulation on real catalytic process required more experimental data.

In this study, core-shell nanostructures were designed for de-NO_x reaction by hydrogen. The results clearly demonstrate designs of heterogeneous catalysts are possible. Mavrikakis and co-workers predict that Cu/Pt NSA has a weaker hydrogen binding compared to a pure Pt surface, which further indicates more active H species and influences reaction selectivity.[77] The Cu/Pt NSA is the idealized system, and contains one monolayer of Pt on a Cu slab. In impregnation-based preparation methods of heterogeneous catalysts, it is not possible to make supported Cu/Pt NSA catalyst. Here, Cu@Pt core-shell NPs were synthesized, and studied for de-NO_x reaction by hydrogen. The catalytic results of the Cu@Pt catalyst show that the activity of pure Pt catalyst is maintained and a higher selectivity of N_2 is observed, which are consistent with the predictions of the NSA theory. In addition, the Pd@Pt catalyst was found to maintain the high activity of pure Pt catalyst and was more selective for N_2 product. In the Pt@Pd catalyst, the selectivity of N_2 is enhanced as well as the activity compared to the pure Pd catalyst. These studies provide important feedback of real heterogeneous catalysts to physical chemists and facilitate the further advance of theoretical simulation on non-ideal systems.

The influence of metal-metal interactions on catalytic performance is the central topic for bimetallic catalysts, which are extensively used in industrial processes. Scientists and

engineers have exploited various techniques, such as XPS and Extended X-ray Absorption Fine Structure (EXAFS), to characterize bimetallic catalysts prepared by current impregnation methods, and attribute the performance enhancement to alloying processes.[166] However, it is difficult to obtain the detailed information of the degree of alloying. Here, Au-Pt nanostructures with different degrees of alloying unequivocally demonstrate that the degree of metal-metal interactions strongly influences the catalytic behavior. The alloy AuPt NPs are CO tolerant hydrogen catalysts. The hydrogen oxidation and CO oxidation are initiated together, and CO conversion can not be completely done. This behavior results from Au-Pt interactions, which weaken the binding between the CO molecule and the Pt atom. The Au-Pt interactions also activate the Au component for oxygen activation, which is proven by the presence of oxidized Au component detected by XPS. In contrast, the AuPt heteoaggregate bimetallic NPs do not exhibit any significant enhancement compared to the pure Pt catalyst due to the absence of strong Au-Pt interactions. However, in the presence of an Fe promoter, the heteroaggregates show an enhanced CO tolerant hydrogen activation and high selectivity to CO_2 due to the unique heteroaggregate structure.

This study clearly shows how the degree of alloying and architecture of NPs influence the catalytic performance, and provides important principles for the design of heterogeneous catalysts.

4.2. Synthetic Method Development for Material Synthesis

4.2.1. Synthetic Methods for Metastable NPs by The Butyllithium Reduction Method

The development of low temperature synthetic methods for materials, which otherwise require high temperature annealing and solid-state methods, has significant importance in materials science. High temperature annealing in solid-state methods provides many useful materials. However, the materials obtained by this method do not have nanoscale size, and usually can not be dispersed in solution. These disadvantages limit their applications in catalysis. Schaak and co-workers have exploited NPs as a robust toolkit for syntheses of various intermetallic compounds upon annealing in solution or in the solid state at relative low temperatures compared to the bulk methods.[167, 168] The essence of their method is that intermixing of NPs eliminates the solid-solid diffusion as the rate-limiting step in solid state method. Due to the separation of nucleation and alloying, the particles prepared by intermixing of NPs either are aggregates or have a wide particle size distribution. Furthermore, no examples of the formation of intermetallic compounds of immisicible metals, such as Au and Pt, were reported by this method.

In this study, a simple and straightforward method was discovered to synthesize the AuPt alloy NPs by a low temperature solution-based method. In the bulk phase, Au and Pt are immisicible, and AuPt alloy can be only obtained by heat treatment above 1100^{o}C. This study exploited butyllithium to reduce the Au and Pt precursors. This rapid co-reduction method provides a route to mix the Au and Pt atoms, and trap the metastable AuPt alloy phase. The resulting AuPt NPs have a narrow particle size distrubutions, and are dispersible in nonpolar organic solvents. This important finding opens a new

synthetic method for other material synthesis, which either require high temperature annealing or are not possible to prepare by regular methods using reducing agents such as $NaBH_4$ and polyols.

4.2.2. Synthetic Method for fully Architecturally Controlled AuPt Bimetallic NPs

Controlling shapes of nanomaterials remains a challenge in material science. To date, various shape controlled nanomaterials have been reported. For bimetallic nanomaterials, the possible architectures include heterodimers,[13, 85] core-shell structures,[89] alloy structures[12, 52] and nanowires.[96] However, no bimetallic systems contain all the possible architectures previously reported.

In this study, AuPt alloy NPs, AuPt heteroaggregates and AuPt nanowires were synthesized by rapid co-reduction or sequential reduction method. These AuPt bimetallic nanostrutures synthesized in this study, plus the reported Au@Pt NPs,[89, 90] consist of the first example of bimetallic nanomaterials containing all the reported architectures. Moreover, the degree of atomic mixing increases from the heteroaggregates, core-shell structures to alloy NPs, which provides an excellent medium to investigate how the degree of metal-metal interactions influences the catalytic behavior.

4.2.3. Synthetic Method for Kinetically Stabilized Core-shell Structures

Core-shell NPs have been applied in various fields such as optics and catalysis.[11, 51] However, according to phase diagrams some core-shell NPs are metalstable. At an elevated temperature, these metastable core-shell structures will transform into more thermodynamically stable alloy phase. The alloy formation of Pt@Cu NPs upon

annealing is an example, where the CuPt alloy structure is more stable than phase-seperated core-shell structure according to the phase diagram. This phenomenon limits the application of core-shell NPs in catalysis, where usually elevated temperatures are required to overcome activation energy of the reactions.

However, in this study Cu@Pt was found to be a kinetically stabilized core-shell structure that is stabilized by the Kirkendall mass transport effect. Positioning the low melting point metal, Cu, in the core hinders the mass transportation from Pt to Cu due to a limited population of vacancy in Cu cores. Furthermore, in catalytic reaction H_2 provides another stabilizing effect on core-shell structures. The alloy formation is unfavorable due to the high binding enthalpy between H and Pt atoms. This finding greatly advances the understanding of stability of core-shell structures, and facilitates their applications in heterogeneous transformation and other designs of core-shell nanostructures.

Bibliography

(1) Cushing, B. L.; Kolesnichenko, V. L.; O'Connor, C. J. *Chemical Reviews (Washington, DC, United States)* **2004,** *104*, (9), 3893-3946.

(2) Sun, Y.; Mayers, B.; Xia, Y. *Advanced Materials (Weinheim, Germany)* **2003,** *15*, 641-646.

(3) Xia, Y.; Yang, P.; Sun, Y.; Wu, Y.; Mayers, B.; Gates, B.; Yin, Y.; Kim, F.; Yan, H. *Advanced Materials (Weinheim, Germany)* **2003,** *15*, 353-389.

(4) Pool, R. *Science* **1990,** *248*, 1186-1188.

(5) Aiken, J. D., III; Finke, R. G. *Journal of Molecular Catalysis A: Chemical* **1999,** *145*, 1-44.

(6) Tauster, S. J.; Fung, S. C. *Journal of Catalysis* **1978,** *55*, 29-35.

(7) Vannice, M. A.; Twu, C. C.; Moon, S. H. *Journal of Catalysis* **1983,** *79*, 70-80.

(8) Ji, L.; Lin, J.; Zeng, H. C. *Journal of Physical Chemistry B* **2000,** *104*, 1783-1790.

(9) Huidobro, A.; Sepulveda-Escribano, A.; Rodriguez-Reinoso, F. *Journal of Catalysis* **2002,** *212*, 94-103.

(10) Penner, S.; Wang, D.; Su, D. S.; Rupprechter, G.; Podloucky, R.; Schlogl, R.; Hayek, K. *Surface Science* **2003,** *532-535*, 276-280.

(11) Son, S. U.; Jang, Y.; Park, J.; Na, H. B.; Park, H. M.; Yun, H. J.; Lee, J.; Hyeon, T. *Journal of the American Chemical Society* **2004,** *126*, 5026-5027.

(12) Teng, X.; Yang, H. *Journal of the American Chemical Society* **2003,** *125*, 14559-14563.

(13) Gu, H.; Yang, Z.; Gao, J.; Chang, C. K.; Xu, B. *Journal of the American Chemical Society* **2005,** *127*, 34-35.

(14) Yin, Y.; Rioux, R. M.; Erdonmez, C. K.; Hughes, S.; Somorjai, G. A.; Alivisatos, A. P. *Science (Washington, DC, United States)* **2004,** *304*, 711-714.

(15) Niesz, K.; Grass, M.; Somorjai, G. A. *Nano Letters* **2005,** *5*, 2238-2240.

(16) Stoeva, S. I.; Zaikovski, V.; Prasad, B. L. V.; Stoimenov, P. K.; Sorensen, C. M.; Klabunde, K. J. *Langmuir* **2005,** *21*, 10280-10283.

(17) Watzky, M. A.; Finke, R. G. *Chemistry of Materials* **1997,** *9*, 3083-3095.

(18) Toshima, N.; Yonezawa, T. *New Journal of Chemistry* **1998,** *22*, 1179-1201.

(19) Hussain, I.; Graham, S.; Wang, Z.; Tan, B.; Sherrington, D. C.; Rannard, S. P.; Cooper, A. I.; Brust, M. *Journal of the American Chemical Society* **2005,** *127*, 16398-16399.

(20) Glavee, G. N.; Klabunde, K. J.; Sorensen, C. M.; Hadjipanayis, G. C. *Inorganic Chemistry* **1993,** *32*, 474-7.

(21) Glavee, G. N.; Klabunde, K. J.; Sorensen, C. M.; Hadjipanayis, G. C.; Tang, Z. X.; Yiping, L. *Nanostructured Materials* **1993,** *3*, 391-8.

(22) Faraday, M. *Philos. Trans. R. Soc.* **1857,** *147*, 145.

(23) Tan, Y.; Dai, X.; Li, Y.; Zhu, D. *Journal of Materials Chemistry* **2003,** *13*, 1069-1075.

(24) Schulz-Dobrick, M.; Sarathy, K. V.; Jansen, M. *Journal of the American Chemical Society* **2005,** *127*, 12816-12817.

(25) Wilson, O. M.; Scott, R. W. J.; Garcia-Martinez, J. C.; Crooks, R. M. *Journal of the American Chemical Society* **2005,** *127*, 1015-1024.

(26) Liu, Y.; Male, K. B.; Bouvrette, P.; Luong, J. H. T. *Chemistry of Materials* **2003,** *15*, 4172-4180.

(27) Fink, J.; Kiely, C. J.; Bethell, D.; Schiffrin, D. J. *Chemistry of Materials* **1998,** *10*, 922-926.

(28) Jana, N. R.; Peng, X. *Journal of the American Chemical Society* **2003,** *125*, 14280-14281.

(29) Ackerson, C. J.; Jadzinsky, P. D.; Kornberg, R. D. *Journal of the American Chemical Society* **2005,** *127*, 6550-6551.

(30) Hiramatsu, H.; Osterloh, F. E. *Chemistry of Materials* **2004,** *16*, 2509-2511.

(31) Zhao, M.; Sun, L.; Crooks, R. M. *Journal of the American Chemical Society* **1998,** *120*, 4877-4878.

(32) Zhao, M.; Crooks, R. M. *Angewandte Chemie, International Edition* **1999,** *38*, 364-366.

(33) Liu, G.; Yan, X.; Lu, Z.; Curda, S. A.; Lal, J. *Chemistry of Materials* **2005,** *17*, 4985-4991.

(34) Knecht, M. R.; Garcia-Martinez, J. C.; Crooks, R. M. *Chemistry of Materials* **2006,** *18*, 5039-5044.

(35) Son, S. U.; Park, I. K.; Park, J.; Hyeon, T. *Chemical Communications (Cambridge, United Kingdom)* **2004**, 778-779.

(36) Willard, M. A.; Kurihara, L. K.; Carpenter, E. E.; Calvin, S.; Harris, V. G. *International Materials Reviews* **2004,** *49*, 125-170.

(37) Peng, S.; Wang, C.; Xie, J.; Sun, S. *Journal of the American Chemical Society* **2006,** *128*, 10676-10677.

(38) Kim, F.; Connor, S.; Song, H.; Kuykendall, T.; Yang, P. *Angewandte Chemie, International Edition* **2004,** *43*, 3673-3677.

(39) Sun, Y.; Xia, Y. *Science (Washington, DC, United States)* **2002,** *298*, 2176-2179.

(40) Chen, J.; Herricks, T.; Xia, Y. *Angewandte Chemie, International Edition* **2005,** *44*, 2589-2592.

(41) Xiong, Y.; McLellan, J. M.; Chen, J.; Yin, Y.; Li, Z.-Y.; Xia, Y. *Journal of the American Chemical Society* **2005,** *127*, 17118-17127.

(42) Xiong, Y.; Chen, J.; Wiley, B.; Xia, Y.; Aloni, S.; Yin, Y. *Journal of the American Chemical Society* **2005,** *127*, 7332-7333.

(43) Viau, G.; Brayner, R.; Poul, L.; Chakroune, N.; Lacaze, E.; Fievet-Vincent, F.; Fievet, F. *Chemistry of Materials* **2003,** *15*, 486-494.

(44) Cha, S. I.; Mo, C. B.; Kim, K. T.; Hong, S. H. *Journal of Materials Research* **2005,** *20*, 2148-2153.

(45) Jin, S.; Yuan, L.; Zhou, Y.; Qiu, G.; Wan, C. *Materials Research Bulletin* **2006,** *41*, 2130-2136.

(46) Sun, Y.; Xia, Y. *Advanced Materials (Weinheim, Germany)* **2002,** *14*, 833-837.

(47) Roychowdhury, C.; Matsumoto, F.; Mutolo, P. F.; Abruna, H. D.; DiSalvo, F. J. *Chemistry of Materials* **2005,** *17*, 5871-5876.

(48) Hou, Y.; Kondoh, H.; Kogure, T.; Ohta, T. *Chemistry of Materials* **2004,** *16*, 5149-5152.

(49) Blin, B.; Fievet, F.; Beaupere, D.; Figlarz, M. *New Journal of Chemistry* **1989,** *13*, 67-72.

(50) Xiong, Y.; Wiley, B.; Chen, J.; Li, Z.-Y.; Yin, Y.; Xia, Y. *Angewandte Chemie, International Edition* **2005,** *44*, 7913-7917.

(51) Banin, U.; Bruchez, M.; Alivisatos, A. P.; Ha, T.; Weiss, S.; Chemla, D. S. *Journal of Chemical Physics* **1999,** *110*, 1195-1201.

(52) Sun, S.; Murray, C. B.; Weller, D.; Folks, L.; Moser, A. *Science (Washington, D. C.)* **2000,** *287*, 1989-1992.

(53) Lisiecki, I. *Journal of Physical Chemistry B* **2005,** *109*, 12231-12244.

(54) Lee, C.-C.; Chen, D.-H. *Nanotechnology* **2006,** *17*, 3094-3099.

(55) Teng, X.; Black, D.; Watkins, N. J.; Gao, Y.; Yang, H. *Nano Letters* **2003,** *3*, 261-264.

(56) Zhang, L.; Dou, Y.-H.; Gu, H.-C. *Journal of Colloid and Interface Science* **2006,** *297*, 660-664.

(57) Puntes, V. F.; Krishnan, K. M.; Alivisatos, A. P. *Science (Washington, DC, United States)* **2001,** *291*, 2115-2117.

(58) Massalski, T. B.; Murray, J. L.; Bennett, L. H.; Baker, H. *Binary Alloy Phase Diagram*. American Society for Metals: Metals Park, 1986; 'Vol.' 1, p 1096.

(59) Sun, Y.; Mayers, B. T.; Xia, Y. *Nano Letters* **2002,** *2*, 481-485.

(60) Tomus, D., Tsuchiya, K.; Inuzuka, M.; Sasaki, M.; Imai, D.; Ohmori, T.; Umemoto, M. *Scripta Mater.* **2003,** *48*, 489.

(61) Stejny, J.; Dlugosz, J.; Keller, A. *Journal of Materials Science* **1979,** *14*, 1291-300.

(62) Stejny, J.; Trinder, R. W.; Dlugosz, J. *Journal of Materials Science* **1981,** *16*, 3161-70.

(63) Tarascon, J. M.; DiSalvo, F. J.; Chen, C. H.; Carroll, P. J.; Walsh, M.; Rupp, L. *Journal of Solid State Chemistry* **1985,** *58*, 290-300.

(64) Suslick, K. S. *Science (Washington, DC, United States)* **1990,** *247*, 1439-45.

(65) Mayers, B.; Xia, Y. *Journal of Materials Chemistry* **2002,** *12*, 1875-1881.

(66) Mayers, B.; Gates, B.; Yin, Y.; Xia, Y. *Advanced Materials (Weinheim, Germany)* **2001,** *13*, 1380-1384.

(67) Jones, E. T. T.; Chyan, O. M.; Wrighton, M. S. *Journal of the American Chemical Society* **1987,** *109*, 5526-8.

(68) Hulteen, J. C.; Martin, C. R. *Journal of Materials Chemistry* **1997,** *7*, 1075-1087.

(69) Li, M.; Schnablegger, H.; Mann, S. *Nature (London)* **1999,** *402*, 393-395.

(70) Zhang, Y.; Franklin, N. W.; Chen, R. J.; Dai, H. *Chemical Physics Letters* **2000,** *331*, 35-41.

(71) Korgel, B. A.; Fitzmaurice, D. *Advanced Materials (Weinheim, Germany)* **1998,** *10*, 661-665.

(72) Peng, X.; Manna, U.; Yang, W.; Wickham, J.; Scher, E.; Kadavanich, A.; Allvisatos, A. P. *Nature (London)* **2000,** *404*, 59-61.

(73) Tang, C.; Fan, S.; de la Chapelle, M. L.; Dang, H.; Li, P. *Advanced Materials (Weinheim, Germany)* **2000,** *12*, 1346-1348.

(74) Wu, Y.; Messer, B.; Yang, P. *Advanced Materials (Weinheim, Germany)* **2001,** *13*, 1487-1489.

(75) Wen, X.; Yang, S. *Nano Letters* **2002,** *2*, 451-454.

(76) Greeley, J.; Mavrikakis, M. *Journal of Physical Chemistry B* **2005,** *109*, 3460-3471.

(77) Greeley, J.; Mavrikakis, M. *Nature Materials* **2004,** *3*, 810-815.

(78) Schlapka, A.; Lischka, M.; Gross, A.; Kasberger, U.; Jakob, P. *Physical Review Letters* **2003,** *91*, 016101/1-016101/4.

(79) Hwu Henry, H.; Eng, J., Jr.; Chen Jingguang, G. *Journal of the American Chemical Society* **2002,** *124*, 702-9.

(80) Hungria, A. B.; Iglesias-Juez, A.; Martinez-Arias, A.; Fernandez-Garcia, M.; Anderson, J. A.; Conesa, J. C.; Soria, J. *Journal of Catalysis* **2002,** *206*, 281-294.

(81) Chen, M.; Kumar, D.; Yi, C.-W.; Goodman, D. W. *Science (Washington, DC, United States)* **2005,** *310*, 291-293.

(82) Peng, X.; Wickham, J.; Alivisatos, A. P. *Journal of the American Chemical Society* **1998,** *120*, 5343-5344.

(83) Manna, L.; Scher, E. C.; Alivisatos, A. P. *Journal of the American Chemical Society* **2000,** *122*, 12700-12706.

(84) Yuan, J.; Li, W.-N.; Gomez, S.; Suib, S. L. *Journal of the American Chemical Society* **2005,** *127*, 14184-14185.

(85) Gu, H.; Zheng, R.; Zhang, X.; Xu, B. *Journal of the American Chemical Society* **2004,** *126*, 5664-5665.

(86) Moller, H.; Pistorius, P. C. *Journal of Electroanalytical Chemistry* **2004,** *570*, 243-255.

(87) Lang, H.; Maldonado, S.; Stevenson, K. J.; Chandler, B. D. *Journal of the American Chemical Society* **2004,** *126*, 12949-12956.

(88) Wu, M.-L.; Chen, D.-H.; Huang, T.-C. *Chemistry of Materials* **2001,** *13*, 599-606.

(89) Mandal, S.; Mandale, A. B.; Sastry, M. *Journal of Materials Chemistry* **2004,** *14*, 2868-2871.

(90) Cao, L.; Tong, L.; Diao, P.; Zhu, T.; Liu, Z. *Chemistry of Materials* **2004,** *16*, 3239-3245.

(91) Massalski, T. B.; Murray, J. L.; Bennett, L. H.; Baker, H. *Binary Alloy Phase Diagram*. American Society for Metals: Metals Park, 1986; 'Vol.' 1, p 298-299.

(92) Mariscal, M. M.; Dassie, S. A.; Leiva, E. P. M. *Journal of Chemical Physics* **2005,** *123*, 184505/1-184505/6.

(93) Njoki, P. N.; Luo, J.; Wang, L.; Maye, M. M.; Quaizar, H.; Zhong, C.-J. *Langmuir* **2005,** *21*, 1623-1628.

(94) Damle, C.; Biswas, K.; Sastry, M. *Langmuir* **2001,** *17*, 7156-7159.

(95) Chen, Y.; Kim, M.; Lian, G.; Johnson, M. B.; Peng, X. *Journal of the American Chemical Society* **2005,** *127*, 13331-13337.

(96) Liang, H.-P.; Guo, Y.-G.; Zhang, H.-M.; Hu, J.-S.; Wan, L.-J.; Bai, C.-L. *Chemical Communications (Cambridge, United Kingdom)* **2004**, 1496-1497.

(97) Yu, T.; Joo, J.; Park, Y. I.; Hyeon, T. *Journal of the American Chemical Society* **2006,** *128*, 1786-1787.

(98) Zhou, S.; McIlwrath, K.; Jackson, G.; Eichhorn, B. *Journal of the American Chemical Society* **2006,** *128*, 1780-1781.

(99) Zeng, J.; Yang, J.; Lee, J. Y.; Zhou, W. *Journal of Physical Chemistry B* **2006,** *110*, 24606-24611.

(100) Yang, C.-S.; Kauzlarich, S. M.; Wang, Y. C. *Chemistry of Materials* **1999,** *11*, 3666-3670.

(101) Chang, Y.-H.; Chiu, C.-W.; Chen, Y.-C.; Wu, C.-C.; Tsai, C.-P.; Wang, J.-L.; Chiu, H.-T. *Journal of Materials Chemistry* **2002,** *12*, 2189-2191.

(102) Prater, K. B. *Journal of Power Sources* **1996,** *61*, 105-109.

(103) Appleby, A. J. *Philosophical Transactions of the Royal Society of London, Series A: Mathematical, Physical and Engineering Sciences* **1996,** *354*, 1681-1693.

(104) Gottesfeld, S.; Pafford, J. *Journal of the Electrochemical Society* **1988,** *135*, 2651-2.

(105) Stonehart, P.; Kohlmayr, G. *Electrochimica Acta* **1972,** *17*, 369-82.

(106) Avgouropoulos, G.; Ioannides, T. *Applied Catalysis, B: Environmental* **2005,** *56*, 77-86.

(107) Bissett, E. J.; Oh, S. H.; Sinkevitch, R. M. *Chemical Engineering Science* **2005,** *60*, 4709-4721.

(108) Ayastuy, J. L.; Gil-Rodriguez, A.; Gonzalez-Marcos, M. P.; Gutierrez-Ortiz, M. A. *International Journal of Hydrogen Energy* **2006,** *31*, 2231-2242.

(109) Shou, M.; Tanaka, K.-i. *Catalysis Letters* **2006,** *111*, 115-118.

(110) Ko, E.-Y.; Park, E. D.; Seo, K. W.; Lee, H. C.; Lee, D.; Kim, S. *Catalysis Letters* **2006,** *110*, 275-279.

(111) Uysal, G.; Akin, A. N.; Oensan, Z. I.; Yildirim, R. *Catalysis Letters* **2006,** *111*, 173-176.

(112) Tanaka, K.-i.; Moro-oka, Y.; Ishigure, K.; Yajima, T.; Okabe, Y.; Kato, Y.; Hamano, H.; Sekiya, S.-i.; Tanaka, H.; Matsumoto, Y.; Koinuma, H.; He, H.; Zhang, C.; Feng, Q. *Catalysis Letters* **2004,** *92*, 115-121.

(113) Tanaka, K.-I.; Shou, M.; He, H.; Shi, X. *Catalysis Letters* **2006,** *110*, 185-190.

(114) Chang, L.-H.; Sasirekha, N.; Chen, Y.-W.; Wang, W.-J. *Industrial & Engineering Chemistry Research* **2006,** *45*, 4927-4935.

(115) Arena, F.; Famulari, P.; Trunfio, G.; Bonura, G.; Frusteri, F.; Spadaro, L. *Applied Catalysis, B: Environmental* **2006,** *66*, 81-91.

(116) Deng, W.; De Jesus, J.; Saltsburg, H.; Flytzani-Stephanopoulos, M. *Applied Catalysis, A: General* **2005,** *291*, 126-135.

(117) Jain, A.; Zhao, X.; Kjergaard, S.; Stagg-Williams, S. M. *Catalysis Letters* **2005,** *104*, 191-197.

(118) Panagiotopoulou, P.; Christodoulakis, A.; Kondarides, D. I.; Boghosian, S. *Journal of Catalysis* **2006,** *240*, 114-125.

(119) Panagiotopoulou, P.; Kondarides, D. I. *Journal of Catalysis* **2004,** *225*, 327-336.

(120) Sendroy, J., Jr.; Collison, H. A.; Mark, H. J. *Anal. Chem.* **1955,** *27*, 1641-5.

(121) Yan, W.; Mahurin, S. M.; Pan, Z.; Overbury, S. H.; Dai, S. *Abstracts of Papers, 231st ACS National Meeting, Atlanta, GA, United States, March 26-30, 2006* **2006**, CATL-020.

(122) Chen, M. S.; Goodman, D. W. *Science (Washington, DC, United States)* **2004,** *306*, 252-255.

(123) Chen, M.; Cai, Y.; Yan, Z.; Goodman, D. W. *Journal of the American Chemical Society* **2006,** *128*, 6341-6346.

(124) Lopez, N.; Janssens, T. V. W.; Clausen, B. S.; Xu, Y.; Mavrikakis, M.; Bligaard, T.; Norskov, J. K. *Journal of Catalysis* **2004,** *223*, 232-235.

(125) Lin, H.-Y.; Chen, Y.-W. *Industrial & Engineering Chemistry Research* **2005,** *44*, 4569-4576.

(126) Schumacher, B.; Denkwitz, Y.; Plzak, V.; Kinne, M.; Behm, R. J. *Journal of Catalysis* **2004,** *224*, 449-462.

(127) Comotti, M.; Li, W.-C.; Spliethoff, B.; Schueth, F. *Journal of the American Chemical Society* **2006,** *128*, 917-924.

(128) Shelef, M. *Chemical Reviews (Washington, D. C.)* **1995,** *95*, 209-25.

(129) Burch, R.; Breen, J. P.; Meunier, F. C. *Applied Catalysis, B: Environmental* **2002,** *39*, 283-303.

(130) Hu, Z.; Allen, F. M.; Wan, C. Z.; Heck, R. M.; Steger, J. J.; Lakis, R. E.; Lyman, C. E. *Journal of Catalysis* **1998,** *174*, 13-21.

(131) Granger, P.; Praliaud, H.; Billy, J.; Leclercq, L.; Leclercq, G. *Surface and Interface Analysis* **2002,** *34*, 92-96.

(132) Ramis, G.; Yi, L.; Busca, G. *Catalysis Today* **1996,** *28*, 373-380.

(133) Sadykov, V.; Kuznetsova, T.; Doronin, V.; Bunina, R.; Alikina, G.; Batuev, L.; Matyshak, V.; Rozovskii, A.; Tretyakov, V.; Burdeynaya, T.; Lunin, V.; Ross, J. *Catalysis Today* **2006,** *114*, 13-22.

(134) Liu, Z.; Oh, K. S.; Woo, S. I. *Catalysis Surveys from Asia* **2006,** *10*, 8-15.

(135) Komatsu, T.; Tomokuni, K.; Yamada, I. *Catalysis Today* **2006,** *116*, 244-249.

(136) Ingelsten, H. H.; Skoglundh, M. *Catalysis Letters* **2006,** *106*, 15-19.

(137) Arve, K.; Popov, E. A.; Klingstedt, F.; Eraenen, K.; Lindfors, L. E.; Eloranta, J.; Murzin, D. Y. *Catalysis Today* **2005,** *100*, 229-236.

(138) Klingstedt, F.; Eraenen, K.; Lindfors, L. E.; Andersson, S.; Cider, L.; Landberg, C.; Jobson, E.; Eriksson, L.; Ilkenhans, T.; Webster, D. *Topics in Catalysis* **2004,** *30/31*, 27-30.

(139) Huuhtanen, M.; Maeaettae, T.; Rahkamaa-Tolonen, K.; Maunula, T.; Keiski, R. L. *Topics in Catalysis* **2004,** *30/31*, 359-363.

(140) Garcia-Cortes, J. M.; Perez-Ramirez, J.; Rouzaud, J. N.; Vaccaro, A. R.; Illan-Gomez, M. J.; Salinas-Martinez De Lecea, C. *Journal of Catalysis* **2003,** *218*, 111-122.

(141) Eranen, K.; Lindfors, L.-E.; Klingstedt, F.; Murzin, D. Y. *Journal of Catalysis* **2003,** *219*, 25-40.

(142) Eraenen, K.; Klingstedt, F.; Arve, K.; Lindfors, L.-E.; Murzin, D. Y. *Journal of Catalysis* **2004,** *227*, 328-343.

(143) Burch, R.; Watling, T. C. *Journal of Catalysis* **1997,** *169*, 45-54.

(144) Saaid, I. M.; Mohamed, A. R.; Bhatia, S. *Journal of Molecular Catalysis A: Chemical* **2002,** *189*, 241-250.

(145) Montes de Correa, C.; Cordoba, F.; Bustamante, F. *Microporous and Mesoporous Materials* **2000,** *40*, 149-157.

(146) Burch, R.; Coleman, M. D. *Journal of Catalysis* **2002,** *208*, 435-447.

(147) Burch, R.; Shestov, A. A.; Sullivan, J. A. *Journal of Catalysis* **1999,** *186*, 353-361.

(148) Shestov, A. A.; Burch, R.; Sullivan, J. A. *Journal of Catalysis* **1999,** *186*, 362-372.

(149) Burch, R.; Shestov, A. A.; Sullivan, J. A. *Journal of Catalysis* **1999,** *188*, 69-82.

(150) Costa, C. N.; Savva, P. G.; Andronikou, C.; Lambrou, P. S.; Polychronopoulou, K.; Belessi, V. C.; Stathopoulos, V. N.; Pomonis, P. J.; Efstathiou, A. M. *Journal of Catalysis* **2002,** *209*, 456-471.

(151) Costa, C. N.; Stathopoulos, V. N.; Belessi, V. C.; Efstathiou, A. M. *Journal of Catalysis* **2001,** *197*, 350-364.

(152) Otto, K.; Yao, H. C. *Journal of Catalysis* **1980,** *66*, 229-36.

(153) Machida, M.; Ikeda, S. *Journal of Catalysis* **2004,** *227*, 53-59.

(154) Macleod, N.; Cropley, R.; Keel, J. M.; Lambert, R. M. *Journal of Catalysis* **2004,** *221*, 20-31.

(155) Marina, O. A.; Yentekakis, I. V.; Vayenas, C. G.; Palermo, A.; Lambert, R. M. *Journal of Catalysis* **1997,** *166*, 218-228.

(156) Bradley, J. S.; Hill, E. W.; Klein, C.; Chaudret, B.; Duteil, A. *Chemistry of Materials* **1993,** *5*, 254-6.

(157) Toshima, N.; Wang, Y. *Langmuir* **1994,** *10*, 4574-80.

(158) Wang, Y.; Toshima, N. *Journal of Physical Chemistry B* **1997,** *101*, 5301-5306.

(159) Esumi, K.; Tano, T.; Torigoe, K.; Meguro, K. *Chemistry of Materials* **1990,** *2*, 564-7.

(160) Massalski, T. B.; Murray, J. L.; Bennett, L. H.; Baker, H. *Binary Alloy Phase Diagram*. American Society for Metals: Metals Park, 1986; 'Vol.' 1, p 948.

(161) Hansen, M. P.; Anderko, R. N. K. *Constitution of Binary Alloys*. McGRAW-HILL: New York, 1958; p 612-615.

(162) Zhou, S.; Varughese, B.; Eichhorn, B.; Jackson, G.; McIlwrath, K. *Angew Chem Int Ed Engl FIELD Full Journal Title:Angewandte Chemie (International ed. in English)* **2005,** *44*, 4539-43.

(163) Hamada, H.; Kintaichi, Y.; Sasaki, M.; Ito, T.; Tabata, M. *Applied Catalysis* **1991,** *75*, L1-L8.

(164) Obuchi, A.; Ohi, A.; Nakamura, M.; Ogata, A.; Mizuno, K.; Ohuchi, H. *Applied Catalysis, B: Environmental* **1993,** *2*, 71-80.

(165) Klotzer, B.; Unterberger, W.; Hayek, K. *Surface Science* **2003,** *532-535*, 142-147.

(166) Guczi, L.; Bazin, D.; Kovacs, I.; Borko, L.; Schay, Z.; Lynch, J.; Parent, P.; Lafon, C.; Stefler, G.; Koppany, Z.; Sajo, I. *Topics in Catalysis* **2002,** *20*, 129-139.

(167) Leonard, B. M.; Schaak, R. E. *Journal of the American Chemical Society* **2006,** *128*, 11475-11482.

(168) Schaak, R. E.; Sra, A. K.; Leonard, B. M.; Cable, R. E.; Bauer, J. C.; Han, Y.-F.; Means, J.; Teizer, W.; Vasquez, Y.; Funck, E. S. *Journal of the American Chemical Society* **2005,** *127*, 3506-3.